Viscous Waves in ^{4}He Films

by

Diane Susan Spencer

Department of Physics,
Royal Holloway and Bedford New College,
University of London.

A thesis submitted for the degree of
Doctor of Philosophy at the University of London.

Abstract

A quartz crystal resonator has been used to excite shear waves at a frequency of 20.5 MHz in ^{4}He films above and below the superfluid transition and just above the liquid-gas critical point. The wave has a viscous penetration depth $\delta \simeq 20$ nm and the transverse acoustic impedance $Z = R - iX$ of the film was found from changes in the quality factor and resonant frequency of the crystal. The thickness of a He I film was swept at constant temperature by creating a small temperature difference between the ^{4}He film on the crystal and bulk liquid helium below it. Calculations of the impedance of a homogeneous film as a function of d/δ using transmission line theory show the film's thickness d could be swept from 1.5 to $\gtrsim$60 nm. The impedance of six superfluid films of constant thickness in the range 14-23 nm has been measured for $0.4 < T < T_\lambda$. From the impedance in the ballistic limit, $\omega\tau \gg 1$, the average probability of the quantum evaporation of a ^{4}He atom by a roton incident upon the liquid-vapour interface is estimated to be ~ 0.35. A resonance, the temperature of which was dependent on film thickness, was observed in the superfluid film and has tentatively been identified with the resonance in the $\lambda/4$ Kelvin mode of vortices pinned to the crystal surface. The transverse acoustic impedance Z of helium has also been measured 49 mK above the liquid-gas critical point for pressures up to 2000 torr. In the highly compressible critical region, the impedance shows the effects of the large density gradients that develop close to the crystal surface under van der Waals' forces. At low pressures, the transition to non-hydrodynamic behaviour ($\omega\tau > 1$) is observed, and it is estimated that a fraction 0.2 of ^{4}He atoms incident upon the crystal are diffusely scattered from it.

CONTENTS

FIGURE CAPTIONS

2.1 The velocity profile of the viscous wave, penetration depth $\delta = (2\eta/\rho\omega)^{\frac{1}{2}}$. $x = 0$ is the solid/liquid interface.

3.1 Schematic block diagram of the feedback circuit used to lock on to the resonance of the quartz crystal.

3.2 Electrical representation of the transmission circuit.

3.3 The signal S as a function of frequency, showing the resonance of the crystal at 20.5 MHz at 4.2 K in vacuum.

3.4 Diode detector calibration.

3.5 Diagram of the sonic cell.

3.6 Resistance thermometer calibration: R4 .

3.7 Resistance thermometer calibration: R8 .

3.8 $Q/\Delta T$ versus exchange gas pressure for the cell at 5 K .

3.9 Calibration for the carbon-glass resistance thermometer.

3.10 Gas handling and pressure measurement system.

3.11 Schematic diagram of the system used for data acquisition.

4.1 The change of film thickness d with temperature difference $\Delta T = T_x - T_o$ between the crystal and the bulk liquid helium below it, for a film of equilibrium ($\Delta T = 0$) thickness 20 nm at 3 K .

4.2 The real and imaginary parts, R and X, of the transverse acoustic impedance of a film, thickness d, in vacuum. The bulk liquid has an impedance $(1 - i)r$ and δ is the penetration depth of the viscous wave.

4.3 The profile of a ^{4}He film, thickness d, adsorbed on the crystal, showing the localised atomic layer and the region of enhanced density liquid caused by the van der Waals' forces.

4.4 The change in resonant frequency $\Delta f = f_o - f$ of the crystal versus the signal S, representing its quality factor $(Q \alpha S^{\frac{1}{2}})$, as the thickness of a He I film is swept at 3.11 K .

4.5 X versus R for the data of Figure 4.4, showing the locus of X versus R for a film of bulk impedance 172 $kgm^{-2}\ s^{-1}$ with a vapour impedance of zero (dashed line) and of 16 $kgm^{-2}\ s^{-1}$ (solid line). At 3.11 K , $\delta = 19$ nm .

4.6 The temperature dependence of the real and imaginary parts R and X of the impedance of bulk liquid ^{4}He at 20 MHz .

4.7 X versus R for ^{4}He films at 2.33 and 2.78 K . The solid line is the same as that drawn in Figure 4.5 and represents the data at 3.11 K .

4.8 Table giving the impedance $z = r - ix$ of bulk liquid helium, the penetration depth δ of the viscous wave in the liquid and the viscosity η_v and impedance r_v of the helium vapour at various temperatures.

5.1 Temperature dependence of the real and imaginary parts R and X of the acoustic impedance of a film of thickness 14.5 nm . Also shown is the impedance calculated for a homogeneous film (solid lines) and that corrected for the effects of the enhancement of the density of the helium close to the crystal (dashed line).

5.2 Temperature dependence of R and X of a film of thickness 15.5 nm .

5.3 Temperature dependence of R and X of a film of thickness 17.5 nm .

5.4 Temperature dependence of R and X of a film of thickness 19.5 nm .

5.5 Temperature dependence of R and X of a film of thickness 21.0 nm .

5.6 Temperature dependence of R and X of a film of thickness 22.5 nm .

5.7 The impedance X versus R for films of thickness 14.5 and 21 nm , showing the normal liquid spiral at T_λ .

5.8 The real part R of the impedance of films at thickness 14.5 and 15.5 nm at low temperature. Also shown is the ballistic impedance calculated for rotons (solid lines) and phonons (dashed line).

5.9 The imaginary part X of the impedance of the 14.5 and 15.5 nm films, showing the roton ballistic impedance for a 15 nm film (solid line) and including the effects of two-dimensional rotons (dashed line).

5.10 The height h of the crystal above the surface of bulk liquid helium versus the film thickness.

5.11 $A(d) = (mgh/K_b)(d/d_o)^3$ as a function of film thickness d for the data of Figure 5.10 and for various substrates.

5.12 The temperature dependence of the resonance in the superfluid film and of the resonance at $d = \lambda/4$ of Kelvin waves on pinned vortices at 20.5 MHz .

5.13 The temperature dependence of R and X for a film thickness 15.5 nm with a vortex resonance at 1.65 K .

5.14 The temperature dependence of R and X for a film of thickness 21 nm with a vortex resonance at 0.06 K .

5.15 The signal S as a function of frequency at 34 MHz for various power levels.

5.16 Table giving the crystal surface potential $A(d)$ for film thickness d at a height h above the bulk liquid surface, the temperature of the resonance observed and the quality factor calculated for the vortex resonance.

6.1 The real and imaginary parts, R and X , of the acoustic impedance as a function of pressure at 5.239 K .

6.2 $X - R$ for the data of Figure 6.1, showing the excess mass density adsorbed on the crystal for one (upper solid line) and two (lower solid line) adsorbed atomic layers, and for one layer including the effects of viscosity (dashed line).

6.3 Density profile of the helium film on the crystal for various bulk pressures at 5.239 K .

6.4 Temperature dependence of the low density viscosity of ^{4}He gas.

6.5 The density dependence of $\Delta\eta(\rho) = \eta(\rho,T) - \eta(0,T)$ for ^{4}He.

6.6 The effective viscosity of ^{4}He as a function of density at 5.239 K .

6.7 The effective viscosity of ^{4}He at low densities, showing the viscosity calculated for a diffusely scattered fraction α of 0.1, 0.2 and 1.0.

Chapter 1

Introduction

The propagation of stress waves at ultrasonic frequencies is widely used to investigate the physical properties of condensed matter. In both solids and liquids longitudinal and transverse waves propagate, though in liquids the transverse mode is a heavily damped viscous wave whose existance is frequently overlooked. Viscous waves may be excited by, for example, a vibrating wire, a torsional crystal oscillator or a planar crystal vibrating in shear. The high attenuation of the viscous wave makes direct measurement of its velocity and attenuation difficult and it is usually the effects of the liquid on the surface generating the wave, rather than the properties of the wave itself, that are measured.

This thesis reports the excitation of viscous waves in ^{4}He films adsorbed on the electrodes of an AT-cut quartz crystal resonator vibrating in shear. The physical properties of a film of thickness comparable with the penetration depth of the viscous wave, 15 nm at the λ-point at 20 MHz, may then be deduced from changes in the quality factor and resonant frequency of the crystal.

The AT-cut quartz crystal, discussed in Chapter 3.2, vibrates stably in a thickness-shear mode of resonance and is used extensively as a microbalance (Lu, 1984). For both solid films and liquid films of thickness much less than the penetration depth of the viscous wave, the resonant frequency f of the crystal decreases in proportion to the adsorbed mass per unit area σ (Chapter 2.2)

$$\Delta f = - \frac{4f^2\sigma}{nR_q} \qquad (1.1)$$

where n is the harmonic number of the crystal's resonance and R_q is the acoustic impedance of the quartz. As the thickness of a liquid film increases and the effects of viscous damping become appreciable, the quality factor of the crystal's resonance is lowered and the change in the resonant frequency is less than that for a solid film of the same thickness and density. A crystal fully immersed in a liquid of specific transverse acoustic impedance $Z = R - iX$ experiences a change in the frequency f and quality factor Q of the resonance given by

$$\Delta f = - \frac{2fX}{n\pi R_q} \tag{1.2}$$

$$\Delta(Q^{-1}) = \frac{4R}{n\pi R_q} \tag{1.3}$$

for $R_q >> R , X$.

The transverse acoustic impedance at a frequency $f = \omega/2\pi$ of a homogeneous, hydrodynamic fluid of density ρ and viscosity η is, as shown in Chapter 2.3

$$Z = R - iX$$

$$= (1 - i) \sqrt{\frac{\omega\rho\eta}{2}} \tag{1.4}$$

and the viscous penetration depth of the wave is $\delta = \sqrt{2\eta/\rho\omega}$. For He II (see for example Wilks (1967)), the superfluid component, density ρ_s , does not couple to the crystal's motion and the total density and viscosity, ρ and η , are replaced by those of the normal fluid component, $\rho_n = \rho - \rho_s$ and η_n (Putterman, 1974). In general however, the liquid is not homogeneous, the short range ($< \delta$)

van der Waals' forces between a liquid and a solid enhancing the density of helium close to the crystal. The crystal then acts both as a microbalance, the enhanced density helium, equivalent to an adsorbed mass per unit area σ, decreasing its resonant frequency (equation (1.1)) and as a high frequency viscometer with the viscous loading of the helium decreasing both f and Q (equations (1.2) and (1.3)).

If the crystal is immersed in helium of pressure less than the saturated vapour pressure, the van der Waals' forces compress the gas, its density increases and it condenses to form a liquid film on the crystal (Chapter 2.5). The film's thickness will depend upon the pressure of the vapour over the film and hence, if bulk liquid is present, upon the height of the crystal above the liquid level. At $T > T_\lambda$ however, the film thickness is very sensitive to small changes in its temperature and by deliberately creating a temperature difference between the bulk liquid and the film, it is possible, as shown in Chapter 4, to sweep the film thickness from a few nanometers to very much greater than the viscous penetration depth. The impedance measured by the crystal as the film thickness is swept at constant temperature and hence constant δ, may be calculated as a function of the changing ratio d/δ using the transmission line theory of Chapter 2.4.

Below the λ-point it is not possible to create the temperature difference that is used to sweep the film thickness at $T > T_\lambda$, and the superfluid film on the crystal is stable, with a thickness determined by the crystal's height above the liquid level. The data for the impedance measured at various film thicknesses is presented in Chapter 5 and shows the effects of the viscous penetration depth δ

increasing from 15 nm at the λ-point to $\sim$70 nm at 1.2 K for a frequency of 20 MHz. The impedance may be calculated from transmission line theory similar to that used for the normal helium film, since again the relevant parameter is the changing of the ratio d/δ. For $T \lesssim 1.2$ K, the film enters the non-hydrodynamic regime with $\omega\tau \gtrsim 1$ where τ is the relaxation time of the excitations. In the ballistic limit, $\omega\tau >> 1$, the phonons have a negligible effect and the major contribution to the measured impedance is from the rotons. These travel unimpeded across the film after reflection at the crystal, and a fraction α, which may be deduced from the data, transfers momentum from the crystal to the vapour. The superfluid film data also exhibits a large, unexpected thickness and temperature dependent resonance which has tentatively been identified with vortices pinned to the crystal and resonating in the $\lambda/4$ Kelvin mode, with a node at the crystal surface and an antinode at the liquid-vapour interface (Chapter 2.6).

At temperatures greater than that of the liquid-gas critical point T_c, the liquid film cannot form on the crystal. For temperatures only just above T_c however, the high compressibility of the helium in the critical region under the crystal's surface potential causes its density to change rapidly from a gas-like to a liquid-like value. In Chapter 6, measurements of the helium's impedance for the isotherm $T - T_c = 49$ mK are presented; both the data and calculations using transmission line theory show a maximum in the mass adsorbed on the crystal for pressures close to the critical pressure. At low densities, the mean free path of the helium atoms becomes comparable with the viscous penetration depth and it is possible to estimate the fraction of atoms that are diffusely scattered from the crystal surface.

Shear waves have previously been used to probe ^{3}He, ^{4}He and ^{3}He - ^{4}He mixtures in both bulk liquid and adsorbed film states. All techniques measure either or both the frequency of the viscous wave and the energy lost from the resonator to the liquid. In 1960, Welber used a cylindrical, torsionally oscillating crystal to excite viscous waves in bulk ^{4}He at a frequency of 32 kHz and, from the change in the electrical series resistance of the oscillator caused by the damping of the liquid, deduced the product $\rho_n \eta_n$. A torsional oscillator has also been used by Betts et al (1965) and Bertinat et al (1972) to find the effective viscosity at 40 kHz of ^{3}He and solutions of ^{3}He in ^{4}He by measuring the decay of the crystal oscillations. Roach and Ketterson (1976) have used direct transmission of transverse sound between two AC-cut transducers at frequencies of 12-108 MHz to measure the impedance of ^{3}He.

A planar crystal resonator has also been used to propagate shear waves in both bulk liquid helium and adsorbed films. Chester, Yang and Stephens (1972) and Chester and Yang (1973) used a quartz crystal resonator vibrating in shear at a frequency of 24 MHz as a microbalance; since the superfluid component of a helium film adsorbed on the crystal does not couple to its oscillations, they were able to observe the onset of superfluidity in the thin film. These measurements are reported in more detail in Yang's thesis (1973) and have recently been extended to the superfluid onset regime in films of ^{3}He - ^{4}He mixtures (Webster et al, 1979 and 1980). Similar data in the onset region of ^{4}He films has also been obtained by Herb and Dash (1975) at frequencies of 8 and 24 MHz.

Migone et al (1985) have used shear oscillating crystals to investigate the formation at vapour pressures close to the saturated vapour pressure of ^{4}He films on gold and silver substrates for

temperatures between 1.4 K and just below the liquid-gas critical point. Yang and Mason (1980) have also used crystal oscillators to look at the properties of thick adsorbed superfluid helium films, but under zero gravity conditions.

An AT-cut quartz crystal, resonating at frequencies of 20.5, 34.1 and 47.8 MHz has been used in an extensive study of the effective viscosity of bulk ^{4}He, both above the λ-point (Lea and Fozooni, 1986) and below it, under svp (Lea, Fozooni and Retz, 1984) and at pressures up to the solidification pressure (Lea and Fozooni, 1984).

Chapter 2

Background Theory for the Interpretation of the Experimental Results

2.1 Introduction

A crystal resonator immersed in helium and vibrating in shear acts both as a microbalance and as a high frequency viscometer; changes in the quality factor and frequency of the crystal's resonance due to mass and viscous loading being used to find the transverse acoustic impedance of the helium (sections 2.2 and 2.3). The viscous wave propagates in the helium in accordance with the one-dimensional Navier-Stokes equation and is a sensitive probe of the fluid's properties on a length scale comparable with the viscous penetration depth. The van der Waals' forces between a fluid and a substrate enhance the density of the layers of helium close to the crystal and, if the crystal is surrounded by helium vapour, a liquid film may condense upon it (section 2.5). The effects of these and other inhomogeneities on the impedance measured by the crystal can be calculated using transmission-line theory (section 2.4).

2.2 The Effect of Helium on the Resonator

A quartz AT-cut crystal resonator vibrating in shear has a resonant frequency f_s which is determined by the thickness of the crystal t

$$f_s = \frac{nv}{2t} \qquad (2.2.1)$$

where v is the velocity of the shear waves in the crystal and $n = 1, 3, 5, \ldots$ is the harmonic number of the resonance.

For thin adsorbed films the crystal acts as a microbalance; to a first approximation the crystal's Q is unchanged and its resonant frequency decreases in proportion to the adsorbed mass per unit area,

σ (Stockbridge, 1966 and Lu, 1984)

$$\Delta f = - \frac{4f_s^2 \sigma}{nR_q} \tag{2.2.2}$$

where $R_q = \rho_q v$ is the transverse acoustic impedance of the quartz, density ρ_q.

The intrinsic quality factor, Q_o of the resonator is due to loss of energy in the crystal mounting and the intrinsic losses of the quartz itself. If the crystal is immersed in helium of specific transverse acoustic impedance $Z = R - iX$, there are additional losses associated with the excitation of the viscous wave in the fluid. A transverse wave propagating in the quartz and incident normally on one of the two plane interfaces with the helium suffers an energy loss and a phase change on reflection, the complex reflection coefficient A being given by

$$A = \frac{R_q - Z}{R_q + Z} \tag{2.2.3}$$

Since $R_q >> R$ and X, the fractional energy loss from the crystal per reflection is

$$\frac{\Delta E}{E} = \frac{4R}{R_q} \tag{2.2.4}$$

and the phase change of the wave per reflection is

$$\Delta\phi = \frac{2X}{R_q} \tag{2.2.5}$$

The wave undergoes many reflections at the quartz/helium interfaces and the energy lost from the crystal to its surroundings is measured as

a decrease in its quality factor Q, defined as

$$Q = \omega \frac{E}{dE/dt} \tag{2.2.6}$$

where $f = \omega/2\pi$ is the frequency of the wave. Hence, since the wave is reflected $v/t = 2f_s/n$ times per second,

$$\Delta\left(\frac{1}{Q}\right) = \frac{4R}{n\pi R_q} \tag{2.2.7}$$

The phase shift per second is $(2X/R_q)(2f_s/n)$ and the decrease in resonant frequency of the crystal due to the helium is therefore

$$\Delta f = \frac{2f_s X}{n\pi R_q} \tag{2.2.8}$$

Thus R and X, the real and imaginary parts of the transverse acoustic impedance of the helium, can be found from changes in the quality factor Q and resonant frequency f_s of the crystal;

$$R(T) = \frac{n\pi R_q}{4}\left(Q^{-1}(T) - Q_o^{-1}\right) \tag{2.2.9}$$

$$X(T) = \frac{n\pi R_q}{2f_o}\left(f_o - f_s(T)\right) \tag{2.2.10}$$

where f_o and Q_o are the baseline values of the crystal's resonant frequency and quality factor corresponding to $X = 0$ and $R = 0$, and are usually taken as either the low temperature ($T < 0.6$ K) or vacuum values of f_s and Q.

2.3 The Transverse Acoustic Impedance

2.3.1 The Hydrodynamic Region ($\omega\tau < 1$)

The quartz crystal resonator vibrating in the $x = 0$ plane as shown in Figure 2.1, excites a transverse wave in the fluid in which it is immersed. The velocity distribution $u(x)$ of the wave in a homogeneous fluid satisfies the 1-D Navier-Stokes equation (Landau and Lifshitz, 1959)

$$\rho \frac{\partial u(x)}{\partial t} = \eta \frac{\partial^2 u(x)}{\partial x^2} \tag{2.3.1}$$

where η is the viscosity of the fluid and ρ is its density. The amplitude of the shear wave at any point x in the fluid is

$$\xi(x) = \xi_o \exp(- i\omega t - \gamma x) \tag{2.3.2}$$

where $\omega = 2\pi f$. The propagation constant of the wave, γ , is found from equation (2.3.1) with $u(x) \equiv \dot{\xi}(x)$, to be

$$\gamma = (1 - i)/\delta \tag{2.3.3}$$

where

$$\delta = \sqrt{\frac{2\eta}{\rho\omega}} \tag{2.3.4}$$

is the penetration depth of the viscous wave and characterises the distance over which the fluid participates in the crystal's motion. In helium, $\delta \sim 20$ nm and as shown in Figure 2.1, the wave is very heavily damped.

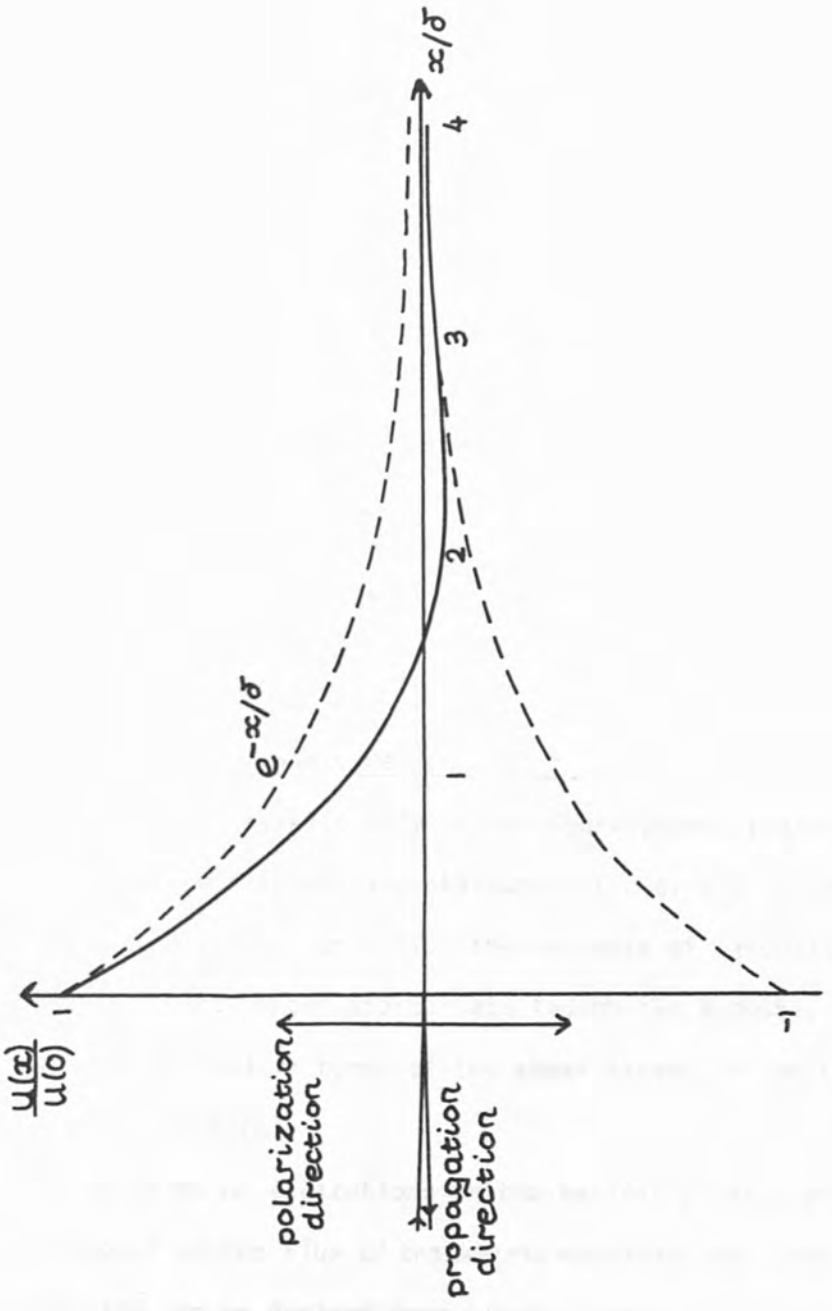

Figure 2.1

The velocity profile of the viscous wave, penetration depth $\delta = (2\eta/\rho\omega)^{\frac{1}{2}}$. $x = 0$ is the solid/liquid interface.

The transverse acoustic impedance of the helium measured by the crystal is defined as

$$Z = \frac{\pi_{yz}}{u(0)} \qquad (a)$$

$$= -\eta \frac{\partial u(0)/\partial x}{u(0)} \qquad (b) \qquad (2.3.5)$$

where π_{yz} is the shear stress on the crystal surface. Hence from equation (2.3.2)

$$\begin{aligned} Z &= \eta\gamma \\ &= (1 - i)\eta/\delta \\ &= (1 - i)\,(\omega\rho\eta/2)^{\frac{1}{2}} \end{aligned} \qquad (2.3.6)$$

2.3.2 The Non-Hydrodynamic Region ($\omega\tau > 1$)

The analysis above is valid only in the hydrodynamic region where $\omega\tau < 1$, τ being a relaxation time characteristic of the system. In the non-hydrodynamic region, $\omega\tau > 1$, the concepts of viscosity and penetration depth are no longer appropriate though the acoustic impedance remains well defined in terms of the shear stress π on the crystal, equation (2.3.5)(a).

For a gas of atoms or excitations in the ballistic limit with $\omega\tau \gg 1$, π is equal to the flux of transverse momentum away from the crystal surface and can be derived from kinetic theory. If the angle between the normal to the crystal and the direction of the gas particle's approach is θ, the number of particles hitting unit area of the crystal/second is given by

$$n_s = \frac{n\bar{c}}{2} \int_0^{\pi/2} \sin\theta\cos\theta d\theta \qquad (2.3.7)$$

where n is the number of particles per unit volume and $\bar{c}$ is their mean velocity.

An incoming particle scattered diffusely by the crystal experiences a change in its transverse momentum of mu, where m is the effective mass of the particle and $u = u_o e^{-i\omega t}$ is the velocity of the crystal surface. The shear stress on the crystal is then

$$\pi = n_s m u_o e^{-i\omega t} \qquad (2.3.8)$$

and the impedance $Z = \pi/u_o e^{-i\omega t}$ is

$$Z_\infty = R_\infty = \tfrac{1}{4} nm \bar{c}$$

$$= \tfrac{1}{4} \rho \bar{c} \qquad (2.3.9)$$

The impedance Z of a bulk gas in the ballistic limit $\omega\tau >> 1$ is therefore purely real and independent of frequency. If a fraction s of the gas particles are specularly reflected from the crystal and pick-up no momentum from it, the ballistic impedance becomes

$$R_\infty = \tfrac{1}{4} \alpha \rho \bar{c} \qquad (2.3.10)$$

where $\alpha = 1 - s$ is the diffusely scattered fraction contributing to the shear stress on the crystal.

At frequencies of 20 MHz, the experimental conditions are such that the helium is relatively often in the non-hydrodynamic region, the two examples of relevance here are the gaseous ^{4}He atoms at low pressures

above the liquid-gas critical point and the phonon and roton excitations in superfluid helium at low temperatures, $T < 1.2$ K.

2.4 Transmission Line Theory

The expression for the acoustic impedance Z, equation (2.3.6), assumes that the helium is homogeneous, having the same properties at the crystal surface, $x = 0$ as in the bulk, $x = \infty$. If the properties of the helium depend on position, and density and viscosity are functions of x, $\rho = \rho(x)$ and $\eta = \eta(x)$, transmission line theory is used to calculate the impedance actually measured by the crystal. A characteristic or local impedance is defined (Lea and Fozooni, 1985),

$$\begin{aligned} z(x) &= \gamma(x)\,\eta(x) \\ &= (1 - i)\,(\omega\rho(x)\,\eta(x)/2)^{\frac{1}{2}} \end{aligned} \tag{2.4.1}$$

which is the impedance a bulk homogeneous fluid would have if its properties were the same as those that exist locally at x. The actual impedance at x, $Z(x)$, is an accumulative value, due to all the fluid to the right of x and is therefore the impedance that would be measured at that point.

From equation (2.3.5)

$$Z(x) = -\eta(x)\,\frac{\partial u(x)/\partial x}{u(x)} \tag{2.4.2}$$

where the velocity $u(x)$ is found from the generalised form of equation (2.3.2) for the displacement of the wave,

$$u(x) = A\,\exp(-\gamma(x)x) + B\,\exp(\gamma(x)x) \tag{2.4.3}$$

where A is the amplitude of the forward travelling wave and B that of any reflected wave. The above three equations, (2.4.1 - 2.4.3) yield the relation between the actual and local impedances at x ;

$$\frac{Z(x)}{z(x)} = \frac{A\ \exp(-\gamma(x)x) - B\ \exp(\gamma(x)x)}{A\ \exp(-\gamma(x)x) + B\ \exp(\gamma(x)x)} \qquad (2.4.4)$$

If a length of transmission line ℓ is considered to represent the fluid between x and $x - \ell$, then $Z(x)$ of equation (2.4.4) is the terminating impedance of the line and $Z(x - \ell)$ is its input impedance and is given by

$$\frac{Z(x - \ell)}{z(x)} = \frac{A\ \exp(-\gamma(x)(x - \ell)) - B\ \exp(\gamma(x)(x - \ell))}{A\ \exp(-\gamma(x)(x - \ell)) + B\ \exp(\gamma(x)(x - \ell))} \qquad (2.4.5)$$

where the length of line ℓ is small and $z(x) \simeq z(x - \ell)$.

Combining equations (2.4.4) and (2.4.5) to relate the input and terminating impedances of the line gives

$$\frac{Z(x - \ell)}{z(x)} = \frac{Z(x)/z(x) + \tanh(\gamma\ell)}{1 + Z(x)/z(x)\tanh(\gamma\ell)} \qquad (2.4.6)$$

where γ is the local propagation constant,

$$\gamma(x) = (1 - i)\sqrt{\frac{\omega\rho(x)}{2\eta(x)}}$$

Equation (2.4.6) reduces to the form

$$Z(x - \ell) = z(x)\ \tanh(\psi + \gamma\ell) \qquad (2.4.7)$$

where

$$\tanh(\psi) = \frac{Z(x)}{z(x)}$$

In the limit of $\ell \to 0$, the differential form of equation (2.4.7) is

$$\frac{dZ(x)}{dx} = \gamma z(x) \left[1-\tanh^2(\psi)\right]$$

$$= \gamma z(x) \left[1 - \frac{Z^2(x)}{z^2(x)}\right] \qquad (2.4.8)$$

In general, this equation has to be solved by numerical methods (Lea and Fozooni, 1985), but for the specific case of a homogeneous film adsorbed on the crystal surface it can be solved analytically, as discussed in Chapter 4.

2.5 Adsorption of Helium Films on the Crystal Resonator

The helium film adsorbed on a substrate has its surface in contact with vapour that is compressed in the potential field $V(x)$ of the substrate, its pressure increasing with decreasing x until, at $x = d$, the vapour condenses. The chemical potential of a helium atom of the gas in the vicinity of the crystal resonator is

$$V_c = K_b T_o \ln [P_x/P_o(T_o)] \qquad (2.5.1)$$

where K_b is the Boltzmann constant, P_o the saturated vapour pressure at temperature T_o and P_x the pressure of the vapour at the crystal. If the pressure at the lowest point in the cell is represented by P_b then equation (2.5.1) becomes

$$V_c = m g h + K_b T_o \ell n [P_b/P_o(T_o)] \qquad (2.5.2)$$

where mgh is the gravitational potential of the helium atom at height h above the cell bottom. At the liquid film surface, the crystal potential $V(d) = -V_c$, and hence, if bulk liquid helium is present in the cell at temperature T_o and the crystal, also at T_o, is a height h above its surface, $P_b = P_o$ and

$$V(d) = -m g h \qquad (2.5.3)$$

The simplest expression for the potential $V(x)$ of the substrate is that deriving from the van der Waals' form of the attractive potential between two molecules, $V(r) \alpha r^{-6}$. Integrating this over the complete substrate yields $V(x) \alpha 1/x^3$ and $V(d)$, the value of the potential at the film surface is therefore

$$V(d) = \frac{-AK_b}{d^3} \qquad (2.5.4)$$

where A is a constant for the substrate.

The van der Waals' forces $F \alpha 1/r^7$, where r is the separation of two atoms, are electromagnetic in origin and arise from fluctuations in the electrostatic dipoles of the atoms. As r increases however, retardation of the electromagnetic radiation becomes important and Casimir and Polder (1948) have shown that for separations large compared with the wavelength λ_o corresponding to transitions between the ground and excited states of the atom, $F \alpha 1/r^8$. This leads to a x^{-4} dependence of the potential of an atom in the field of a planar substrate for large x.

Thus the potential of a substrate is expected to vary as x^{-n} where n increases from $n = 3$ for $x << \lambda_o$ to $n = 4$ for $x >> \lambda_o$. Lifshitz (1956) approached the problem from a macroscopic viewpoint and took the interaction between two solid bodies spaced a short distance d apart to occur via the fluctuating electromagnetic field that is present inside a medium and extends beyond it. The interaction is then completely specified for all separations large compared with interatomic distances by the complex dielectric susceptibilities of the medium and has the limiting forms of $V\alpha x^{-3}$ and $V\alpha x^{-4}$ for small and large separations. Dzyalashinskii, Lifshitz and Pitaevskii (DLP) (1961) extended the Lifshitz theory to liquid films adsorbed on a substrate and in contact with a vapour, and showed how the surface potential may be estimated from the absorption spectra of the liquid, vapour and substrate.

The DLP theory of film thickness has been verified by Sabisky and Anderson (1973) for a helium film adsorbed on a single crystal of SrF_2. Longitudinal acoustic waves (30 GHz) were excited in the helium film and the standing waves set up between the substrate and the free film surface were observed as the pressure of the vapour above the film was reduced and the film thinned. The film thicknesses deduced from the $n\lambda/4$ (n is odd) resonances of the waves in both saturated and unsaturated films over a range of thicknesses, 1-25nm, are in excellent agreement with those calculated from the DLP theory.

In general therefore, for a helium film adsorbed on a substrate, the potential $V(d)$ is proportional to d^{-n}, where n increases from $n = 3$ to $n = 4$ as the film thickness increases, Sabisky and Anderson reporting that the limiting form, $n = 4$ was not reached for their substrate at film thicknesses of 25nm.

The deviation of the potential $V(d)$ from the van der Waals' form $1/d^3$ can be expressed by permitting the substrate constant A to become a function of film thickness. Thus for all d,

$$V(d) = \frac{-A(d)K_b}{d^3}$$

For thin films, Chester, Yang and Stephens (1972) give a value for A of $\sim$40K for gold plated crystals similar to those used in these studies.

2.6 Vortices and Vortex Waves

2.6.1 Vortices in He II

The vortices that exist in superfluid helium are similar to those of classical hydrodynamics (e.g. Batchelor, 1967), but differ in that they have quantized circulation.

The two-fluid model of He II (see for example, Wilks 1967) considers the liquid to be a mixture of two intermingling, non-interacting fluids such that its density is $\rho = \rho_n + \rho_s$. The normal fluid component, density ρ_n carries all the entropy of the liquid and has associated with it a viscosity η_n, while the superfluid component, density ρ_s has zero viscosity and its velocity $\underline{V_s}$ satisfies the relation

$$\underline{\zeta} = \text{curl } \underline{V_s} = 0 \qquad (2.6.1)$$

throughout the liquid. The circulation κ in the helium is defined by the integral

$$\kappa = \oint \underline{V_s} \cdot \underline{d\ell} \qquad (2.6.2)$$

taken over any closed circuit in the liquid. By Stoke's theorem, this becomes

$$\kappa = \oint \text{curl } \underline{V_s} \cdot \underline{ds}$$

for a reducible circuit and therefore, by equation (2.6.1), there should be zero circulation in the helium and the superfluid component in a simply connected rotating bucket should remain at rest with $\underline{V_s} = 0$. Experiments show however (e.g. Osborne, 1950), that the whole mass of He II may be set into uniform rotation and therefore that $\underline{V_s}$ is not zero. This apparent contradiction is resolved by considering the helium to be threaded with vortices with non-zero vorticity $\underline{\zeta}$ along their cores. Thus equation (2.6.1) is satisfied for most of the liquid and yet the helium rotates rigidly with the container as required. For sufficiently high rotation speeds Ω , the liquid will be threaded by a uniform array of vortices aligned along the rotation axis, each with a circulation κ and hence a line density (Feynman, 1955)

$$n_o = \frac{2\Omega}{\kappa} \qquad (2.6.3)$$

The circulation κ is quantized in units of $h/m = 10^{-7} m^2 s^{-1}$ for ^{4}He, hence for an angular velocity $\Omega = 1$ rad.s^{-1} , the vortex line density is $n_o = 2000$ cm^{-2} , equivalent to a spacing between the lines of approximately 0.2 mm .

If a vortex is aligned along the z-axis the velocity of the helium about the axis is

$$V = \frac{\kappa}{2\pi r} \qquad \text{for} \quad r > a \tag{2.6.4}$$

where $a \simeq 1.3\ \mathring{A}$ characterises the size of the vortex core and increases with temperature, diverging as $T \to T_\lambda$. The core of the vortex would classically be that region where the rotating liquid is held back from the vortex axis by centrifugal forces. There is however, no evidence that the core of a vortex in ^4He is a region of zero or depleted density, though for the sake of simplicity, a hollow core model is frequently used to describe it. A more physical picture is that the core radius is related to the superfluid healing length with $\rho_s = 0$ at the vortex axis $r = 0$; from this assumption, Barenghi, Donnelly and Vinen (1953) have estimated the core radius as a function of temperature, and this is the value of a used in the calculations of Chapter 5.

A rectilinear vortex has an energy ε per unit length which, for a hollow core vortex aligned along the z-axis is, in cylindrical polar co-ordinates

$$\varepsilon = \pi \rho_s \int_a^R r\, v^2\, dr \tag{2.6.5}$$

where R is a macroscopic cut-off representing either the size of the container or the spacing between the vortices. In general, for a velocity distribution given by equation (2.6.4), this becomes

$$\varepsilon = \frac{\rho_s \kappa^2}{4\pi} \left[\ell n \left(\frac{R}{a} \right) + \delta \right] \tag{2.6.6}$$

where δ characterises the core model; $\delta = 0$ for a hollow core and $\delta = \frac{1}{4}$ for a core in solid body rotation.

A curved vortex in a stationary fluid has a self induced velocity that is perpendicular to its plane of curvature. The velocity v_i induced at the vortex core by a length of line L is given by (Batchelor, 1967)

$$v_i = \frac{\kappa c}{4\pi} \ell n\left(\frac{L}{a}\right) \tag{2.6.7}$$

where c is the radius of curvature. Thus the vortex line moves and changes its shape with a velocity that at any point is caused by the curvature of the line at that point. A rectilinear vortex with $c = 0$ has no self-induced velocity and remains stationary, whereas a vortex ring, with constant curvature (radius r_o) has a translational velocity (Fetter, 1978)

$$v_i = \frac{\kappa}{4\pi r_o} \left| \ell n \left(\frac{8r_o}{a}\right) - \tfrac{1}{2} + \delta \right| \tag{2.6.8}$$

where δ again characterises the core model.

A vortex moving through a liquid experiences a force perpendicular to its direction of motion known as the Magnus force. In hydrodynamics, this arises because the circulation of the vortex causes an increased velocity of fluid on one side of the vortex, resulting in an excess pressure from the other. If the line is moving with a velocity $\underline{v_\ell}$ in the laboratory frame and has a self-induced velocity $\underline{v_i}$, then in a superfluid flow of velocity $\underline{v_s}$ the streaming of the fluid past the

vortex is given by $(\underline{v}_i + \underline{v}_s)$ and the Magnus force per unit length of line is (Barenghi et al, 1983)

$$\underline{f}_m = \rho_s \underline{\kappa} \times (\underline{v}_\ell - \underline{v}_i - \underline{v}_s) \tag{2.6.9}$$

where $\underline{\kappa} = \kappa\hat{\underline{\omega}}$ and $\hat{\underline{\omega}}$ is a unit vector along the axis of the vortex.

Equation (2.6.9) assumes that the helium in which the vortex exists is pure superfluid. In He II however, interactions between the vortices and the excitations of the normal fluid result in a drag or friction force $\underline{f}_d$ per unit length of line, with components parallel and perpendicular to the direction of the relative motion of the line and the normal fluid,

$$\underline{f}_d = \gamma_o (\underline{v}_n - \underline{v}_\ell) + \gamma_o' \underline{\omega} \times (\underline{v}_n - \underline{v}_\ell) \tag{2.6.10}$$

where $\underline{v}_n$ is the velocity of the normal fluid flow. The mutual friction coefficients γ_o and γ_o' are experimentally determined for $T < 1$ K from the motion of vortex rings attached to ions and can be found indirectly at higher temperatures from the attenuation of second sound by rectilinear vortices in rotating containers.

The motion of the vortex is therefore determined by the balance of forces on the line,

$$\underline{f}_m + \underline{f}_d = 0 \tag{2.6.11}$$

2.6.2 Waves on an Isolated Vortex

Lord Kelvin (Thomson, 1880) showed that it should be possible for

circularly polarized transverse waves to propagate along an isolated vortex line. In this case, the velocity of the line at each point is proportional to its radius of curvature and is in a direction perpendicular to the plane of curvature. If however, the vortex line is one of an array of vortices, its curvature will depend upon the velocity induced at its core by its neighbours; the resulting lattice waves are called Tkachenko waves (Andereck and Glaberson, 1982). Vortex waves in rotating helium were first observed by Hall (1958) on lines pinned between discs oscillating at frequencies of around 1 Hz.

It is possible to gain an insight into the motion of the vortex associated with the Kelvin wave by considering an analogy between the vortex line and a fine elastic filament (Fetter, 1978). Initially, consider the vortex line to be moving with velocity $\underline{v}_i$ in a stationary fluid $\underline{v}_s = 0$, experiencing no drag force, $\underline{f}_d = 0$. Then, from equations (2.6.9) to (2.6.11)

$$\rho_s \underline{\kappa} \times (\underline{v}_\ell - \underline{v}_i) = 0 \qquad (2.6.12)$$

The first term of this equation, $\rho_s \underline{\kappa} \times \underline{v}_\ell$ is effectively the Magnus force on the line resulting from its motion through the fluid. The vortex has associated with it an energy/unit length (equation (2.6.6)) and hence a tension T_o which acts to restore the deformation of the line caused by the Magnus force. T_o is therefore associated with the term $-\rho_s \underline{\kappa} \times \underline{v}_i$ where, as before, $\underline{v}_i$ is the self-induced velocity of the vortex. If the displacement of the vortex is $\underline{u}(z,t)$, the vortex being aligned along the z-axis with its displacement perpendicular to it, then the velocity of the line is $\underline{v}_\ell = \partial \underline{u}/\partial t$ and equation (2.6.12) becomes

$$T_o \frac{\partial^2 \underline{u}}{\partial z^2} + \rho_s \underline{\kappa} \times \frac{\partial \underline{u}}{\partial t} = 0 \qquad (2.6.13)$$

Taking the deformation $\underline{u} = (\xi, \eta, 0)$ and solving (2.6.13) gives the two equations:

$$\begin{aligned} T_o \frac{\partial^2 \xi}{\partial z^2} + \rho_s \kappa \dot{\eta} = 0 \qquad \text{(a)} \\ T_o \frac{\partial^2 \eta}{\partial z^2} + \rho_s \kappa \dot{\xi} = 0 \qquad \text{(b)} \end{aligned} \qquad (2.6.14)$$

Assuming a wave-like dependence $\exp[i(\omega t - kz)]$ for both ξ and η, these equations can be solved for the angular frequency $\omega = 2\pi f$ of the vortex wave, giving

$$\omega_{\pm} = \pm \frac{T_o k^2}{\rho_s \kappa} \qquad (2.6.15)$$

and

$$\eta_{\pm} = \mp i\xi$$

These modes are circularly polarized with a helical deformation that propagates along the vortex axis, each element of core performing a small circular orbit in the plane perpendicular to the undeformed axis. The positive wave ω_+, with $\eta = -i\xi$, has a rotation in the same sense as the superfluid circulation while the negative wave ω_-, $\eta = i\xi$, rotates in the opposite direction.

If the mass of the vortex is taken into account by setting equation (2.6.12) equal to the inertial force $\rho_s \pi a^2(\partial^2\xi/\partial t^2 , \partial^2\eta/\partial t^2)$ then, assuming the waves to be circularly polarized,

$$k_-^2 = \frac{\rho_s \kappa \omega}{T_o}\left(1 + \frac{\omega}{\omega_o}\right)$$

$$k_+^2 = -\frac{\rho_s \kappa \omega}{T_o}\left(1 - \frac{\omega}{\omega_o}\right) \qquad (2.6.16)$$

where $\omega_o = \kappa/\pi a^2$. Therefore, for $\omega < \omega_o$ where $\omega_o/2\pi = 3 \times 10^{11}$Hz, k_+ is imaginary and the wave is a non-propagating mode. For low frequencies, $\omega << \omega_o$,

$$k_+ = i\, k_- \qquad (2.6.17)$$

Superposition of two circularly polarized waves of frequency ω_- travelling in opposite directions along the vortex line yields a sinusoidal deformation of the vortex that is confined to a plane and rotates about the undeformed vortex axis in a direction opposite to that of the superfluid circulation.

Equation (2.6.15) expresses the frequency of the vortex wave in terms of the tension or energy per unit length of the line, equation (2.6.6). A more detailed analysis (Fetter and Harvey, 1971) gives the effective long wavelength tension, and the frequency of the negative wave for $ka << 1$ is then

$$\omega_- = -\frac{\kappa k^2}{4\pi}\left[\ell n\left(\frac{1}{ka}\right) + 0.1159\right] \qquad (2.6.18)$$

which is the result derived by Lord Kelvin (Thomson, 1880). Ashton and Glaberson (1979) have reported the excitation of Kelvin waves on a vortex line by the radiofrequency oscillation (10 MHz) of ions trapped on the vortex.

Equation (2.6.18) is derived assuming there is no interaction between the vortex and the excitations of the normal fluid; if the drag force $\underline{f_d}$ per unit length of line (equation (2.6.10)) is taken into account the wave motion satisfies equation (2.6.11) and the frequency ω_- of the wave is complex, with

$$\begin{aligned} \mathrm{Re}(\omega) &= \omega_- \frac{\gamma(\rho_s\kappa - \gamma_o')}{\gamma_o\rho_s\kappa} \qquad \text{(a)} \\ \ell m(\omega) &= \omega_- \frac{\gamma}{\rho_s\kappa} \qquad \text{(b)} \end{aligned} \tag{2.6.19}$$

where

$$\gamma = \frac{\gamma_o\rho_s^2\kappa^2}{\gamma_o^2 + (\rho_s\kappa - \gamma_o')^2} \tag{2.6.20}$$

Equation (2.6.19)(a) represents a shift in the frequency of the wave and equation (2.6.19)(b) represents its damping.

Chapter 3

Experimental Techniques

3.1 Introduction

The quality factor and resonant frequency of a quartz crystal vibrating in shear were measured for superfluid and normal ^{4}He films and for ^{4}He fluid at a temperature just above that of the liquid gas critical point. The AT-cut crystal (section 3.2) was mounted in a cell supported by and thermally anchored to, the mixing chamber of an Oxford Instrument's ^{3}He-^{4}He dilution refrigerator whose operation is discussed in section 3.5. The experimental cell itself (section 3.4) was designed so it could be used for both bulk and film measurements, in the latter case a tube attached to the cell held liquid ^{4}He and the height of the crystal above the liquid surface determined the equilibrium thickness of the film on the crystal.

The resonant frequency f_s and quality factor Q_s of the crystal were found using a transmission circuit (section 3.3), Q being deduced from the magnitude of the transmitted signal at resonance, S_m. A feedback system was used to lock-on to the crystal's resonance and continuously monitor its frequency and the transmitted signal S_m, which were recorded, together with the resistance of the thermometer by an HP9816 microcomputer (section 3.6).

3.2 The Crystal Resonator

3.2.1 AT-Cut Quartz Crystals

The AT-cut crystal resonator is a member of the singly rotated Y-cut family of crystals; these are crystal plates whose normal is at

an angle ϕ to the Y-axis in the Y-Z plane of the crystallographic axes. The crystals may be piezoelectrically excited into a thickness-shear mode of resonance, with particle motion along the X-axis in the plane of the crystal and antinodes of vibration at opposite faces. The angle of rotation defining the AT-cut, $\phi = 35° 10'$, is chosen such that the resonator has a temperature coefficient of frequency, df/dt of zero at room temperature (Mason, 1940). The high short-term stability of AT-cut quartz crystals has lead to them being an important component in oscillator systems and research into their properties and behaviour has recently been extended to cryogenic temperatures because of the increase in Q-factor and greater long-term frequency stability that can be expected.

The resonator used for these studies was a thickness shear mode AT-cut quartz crystal which had been selected and donated by the GEC Hirst Centre, Wembley, Middlesex and had previously been used extensively in measurements of the transverse acoustic impedance of bulk ^{4}He both above and below the λ-point (e.g. Lea et al, 1984, 1985, 1986). The AT-cut crystal is designed to resonate stably in the thickness-shear mode with minimal coupling to other vibrations. Coupling to flexural, extensional and anharmonic modes can occur however, the latter being when phase reversals of the vibration occur along the crystal surface rather than along its thickness. The crystal used in these experiments had a diameter to thickness ratio of 36, sufficiently high to prevent coupling to unwanted modes and no evidence of parasitic resonances had been observed previously.

The resonator consisted of a polished quartz disc of diameter 9 mm and thickness 0.25 mm with vacuum deposited gold electrodes of size 2.5 mm x 2.5 mm and thickness 150 nm, as shown in Figure 3.5.

The crystal was used in its commercial mounting with two Be-Cu springs making contact with the electrodes via conducting epoxy resin.

Equation (2.2.1) gives the resonant frequency of an AT-cut crystal as

$$f_s = \frac{nv}{2t}$$

where t is the thickness of the crystal and v is the velocity of transverse sound in the quartz. The fundamental frequency ($n = 1$) of the crystal used was 6.83 MHz, though for the thickness of electrode plating on the crystal, this mode was not energy trapped and the Q-factor of the resonance was low. The 3rd, 5th and 7th harmonics ($n = 3$, 5 and 7), at 20.5, 34.1 and 47.8 MHz, are energy trapped modes however, and the Q's obtained are high, $> 10^5$ in vacuum at 4.2 K .

Quartz has a hexagonal structure and its mechanical properties are characterised by 6 independent stress constants, c_{ij} with $ij = 11$, 13, 14, 33 and 66. For a singly rotated crystal of cut angle ϕ the velocity of shear waves in quartz of density ρ_q is given by

$$\rho_q v^2 = (c_{66} + P_e)\cos^2\phi + c_{44}\sin^2\phi - 2c_{14}\sin\phi\cos\phi \qquad (3.2.1)$$

where c_{66} , c_{44} and c_{14} are the elastic moduli of the quartz and $P_e = 0.763 \times 10^9$ Nm^{-2} is an empirical factor (Stockbridge, 1966) to account for the effects of piezoelectric stiffening.

The elastic moduli change little with temperature below 77 K, hence, taking the values given by Stockbridge for liquid nitrogen temperatures

$$c_{66} = +38.715 \times 10^{9}\ Nm^{-2}$$

$$c_{44} = +59.645 \times 10^{9}\ Nm^{-2}$$

$$c_{14} = -17.724 \times 10^{9}\ Nm^{-2}$$

and $\rho_q = 2.664\ gcm^{-3}$, the velocity of shear waves in an AT-cut quartz crystal $\phi = 35°\ 10'$ is $3326m\ s^{-1}$. The transverse acoustic impedance of the quartz, $R_q = \rho_q v$ is therefore $8.862 \times 10^{6} kgm^{-2}\ s^{-1}$.

The measured frequency and quality factor, $f(T,P)$ and $Q(T,P)$, include contributions from the change of the quartz crystal's intrinsic properties with temperature and pressure, as well as those from the helium. For practical purposes, however, as shown in section 3.2.2, over the temperature and pressure ranges we are concerned with here, the only non-negligible effect is that of pressure on frequency.

3.2.2 The Effect of Pressure and Temperature on f and Q

The non-helium contribution to the change of resonant frequency with pressure is a result of changes in the intrinsic properties of the quartz of the crystal. Stockbridge (1966) has outlined a method for estimating the fractional frequency change with pressure, $1/f(df/dP)$, using the derivatives of the elastic moduli c_{ij} with respect to pressure. He gives

$$\frac{1}{f}\frac{df}{dp} = \frac{v\vartheta}{v^2} \qquad (3.2.2)$$

where

$$\vartheta = \left[\frac{dv}{dp}\right]_{p=0}$$

and

$$2\rho_q v\vartheta = (\mathcal{E}_{66} + \mathring{P}_e)\cos^2\phi + \mathcal{E}_{44}\sin^2\phi + 2\mathcal{E}_{14}\sin\phi\cos\phi \qquad (3.2.3)$$

from equation (3.2.1). For quartz at 77 K and hence, to a good approximation, also at 4.2 K,

$$\mathcal{E}_{66}/2\rho_q = -0.4269 \times 10^{-3}\ m^3kg^{-1}$$
$$\mathcal{E}_{44}/2\rho_q = +0.2003 \times 10^{-3}\ m^3kg^{-1}$$
$$\mathcal{E}_{14}/2\rho_q = -0.7967 \times 10^{-3}\ m^3kg^{-1}$$
$$\mathring{P}_e/2\rho_q = -0.0002 \times 10^{-3}\ m\ kg^{-1}$$

For the AT-cut crystal, $\phi = 35°\ 10'$ and $1/f(df/dp) = 18.8 \times 10^{-10}\ torr^{-1}$ which for the third harmonic, 20 MHz, is 0.0388 Hz/torr. Measurements taken at $T = 0.25$ K where the superfluid helium exerts no viscous loading on the crystal give $df/dp = (0.0399 \pm 0.0003)$ Hz/torr (Lea and Fozooni, 1984); the discrepancy may be due to the slight temperature dependence of the crystal parameters below 77 K. Similar measurements also show that the quality factor Q is essentially independent of pressure over the range used here ($< 2000\tau$) .

The frequency stability of an AT-cut quartz crystal with temperature, $1/f(df/dT)$ has been given by Mossuz and Gagnepain (1976) as $< 4 \times 10^{-9}\ K^{-1}$ at 4.2 K , though Komiyama's estimate (1981) is higher, $1.2 \times 10^{-8}\ K^{-1}$ at 4.2 K , decreasing to $1.5 \times 10^{-9}\ K^{-1}$ at 2 K . The Q-factor of the crystal at liquid helium temperatures is also expected to have a small temperature coefficient as there is a relaxation peak in quartz and a consequent decrease in Q at around 15 K, but experimentally the Q is found to change only slightly below 2 K .

For $T < 2$ K , the effects of temperature should be negligible, certainly less than the error bars upon the measurements of f and Q themselves, and for temperatures higher than this, f and Q are taken relative to reference values f_o and Q_o obtained at the same temperature.

3.2.3 Amplitude and Velocity of the Crystal Surface Vibration

It is important that the amplitude of the crystal vibration is small and that its velocity is less than the critical velocity of the helium film. Estimates of the maximum amplitude ξ and velocity $\dot{\xi}$ of the n'th harmonic's vibration can be obtained; following Stockbridge (1966)

$$\xi = d_{26} \frac{I\omega L}{2n} \tag{3.2.4}$$

and

$$\dot{\xi} = \frac{2\xi v}{t} \tag{3.2.5}$$

where $d_{26} = 3.44 \times 10^{-12}$ C/N is the piezoelectric coefficient of the quartz, L is the crystal's inductance and t is its thickness. The current I in the crystal, resistance $r \simeq 60\Omega$ at resonance, is estimated from the transmission circuit of Figure 3.2 to be

$$I = \frac{\sqrt{200 P_{rf}}}{100 + r}$$

where P_{rf} is the r.f. power in the circuit in watts and is found

from the setting, in dBm, on the Marconi signal generator, where 0dBm ≡ 1 mW and represents the power dissipated in a 50Ω load connected across the output terminals of the oscillator.

At 20.5 MHz (n = 3), L = 0.18 H and for P_{rf} = -56 dBm, the peak current in the crystal is ∿6.3 μA, hence $\xi_{max} \simeq 0.8\mathring{A}$ and $\dot{\xi} \simeq 0.2$ cm s^{-1}. This latter is very much less than the critical velocity of the HeII film; for d = 20 nm, v_c = 30 cm s^{-1} (Atkins, 1959).

The power dissipation in the crystal P_c was kept as low as possible to minimise heating effects; for P_{rf} = -56 dBm, P_c ∿ 1.5 nW. Power dependence was checked for, and apart from a notable exception discussed in Chapter 5, none was observed. Chester, Yang and Stephens (1972) used power dissipations of ∿1 μW in their quartz crystals and reported no power dependence of their film measurements, though Yang (1973) notes that there was considerable power dependence of measurements in bulk HeII at similar levels.

Through the power dissipated in it, the crystal is maintained at a temperature higher than that of the ambient helium by the Kapitza effect. The temperature difference between the crystal and the helium is given by $\Delta T = (R_K/A)P_c$ where for T > 0.2 K, $R_K T^3 \sim 0.001$ $K^4m^2W^{-1}$ (Lounasmaa, 1974) and $A \sim 10^{-5}$ m is the total surface area of the electrodes. Thus for P_c = 1.5 nW, $\Delta T \simeq 0.2$ μK at 1 K and the crystal and the helium are in good thermal equilibrium.

3.3 The Measurement of f and Q

3.3.1 The Transmission Circuit

The transmission circuit used to measure f and Q is shown in block diagram form in Figure 3.1. The crystal was placed in series with a Marconi 2018 signal generator and driven at powers of between

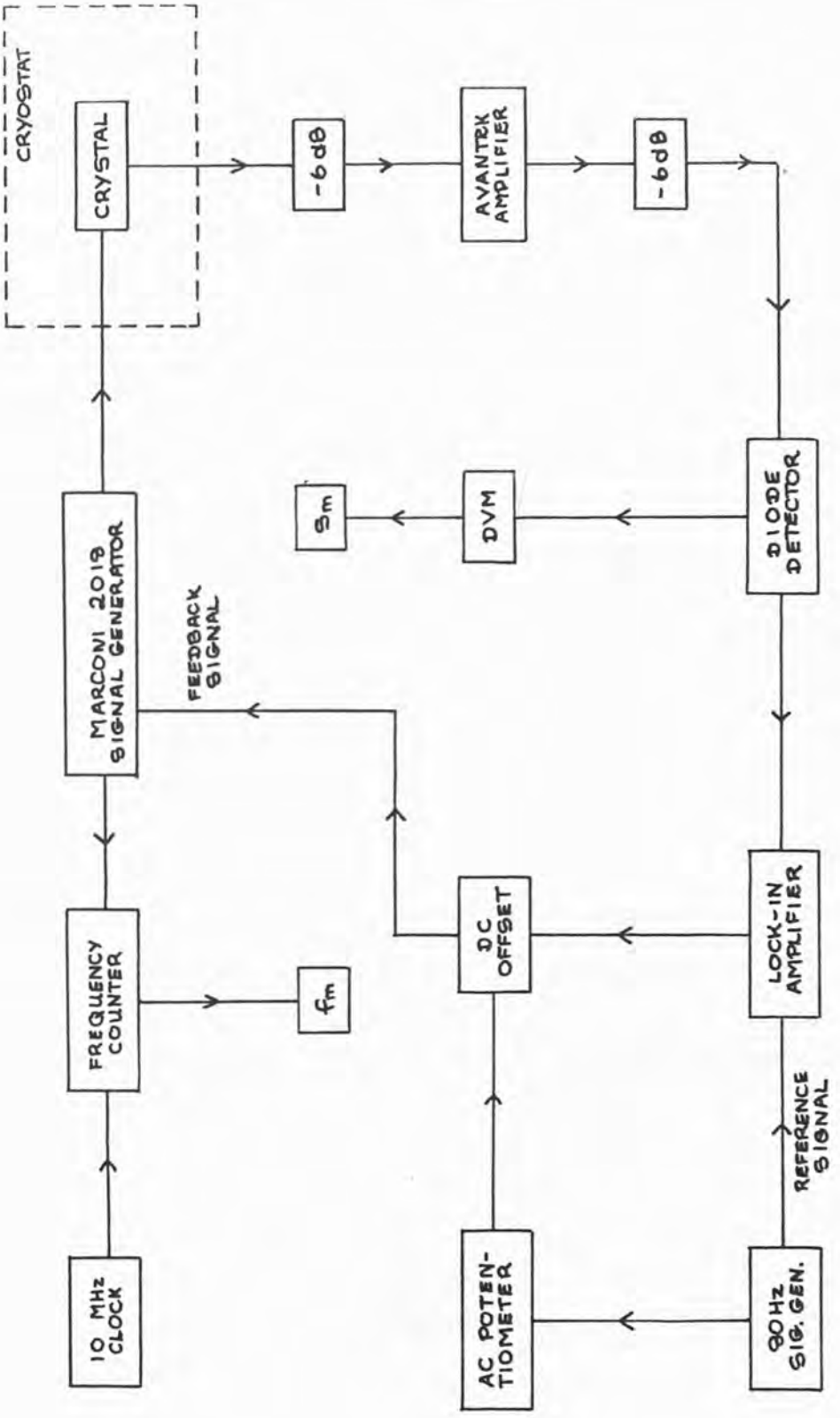

Figure 3.1

Schematic block diagram of the feedback circuit used to lock onto the resonance of the quartz crystal.

-47 and -57 dBm. The transmitted signal was amplified by a high gain Avantek amplifier and detected by a diode detector. Figure 3.2 shows the electrical representation of this transmission circuit with the crystal represented by the equivalent circuit of an AT-cut crystal near resonance; a series LCR branch in parallel with a capacitance C_o (Berlincourt, 1964 and Firth, 1965). The series impedances L and C represent the vibrating body and are frequency independent for a given resonance, but may change with the harmonic number of the resonance. The resistance r_q represents the losses of the crystal due to internal friction and determines the intrinsic Q_o of the crystal. The shunt capacitance C_o is an actual lump capacitance due to the crystal electrodes and stray capacitance of the supporting structures. Typical values at 20 MHz of the equivalent circuit components are:

$$L = 0.18 \text{ H}$$

$$C = 0.34 \times 10^{-3} \text{ pF}$$

$$r_q = 50\,\Omega$$

$$C_o = 0.730 \pm 0.006 \text{ pF}$$

The crystal has two characteristic frequencies, the series and parallel resonances f_{so} and f_{po}, given by

$$f_{so} = \frac{1}{2\pi\sqrt{LC}} \tag{3.3.1}$$

$$f_{po} = \frac{1}{2\pi}\sqrt{\frac{1 + C/C_o}{LC}} \tag{3.3.2}$$

Hence $\Delta f_{po} = f_{so} - f_{po} \simeq f_{so}\, C/2C_o = 4830$ Hz at 20 MHz .

If helium is in contact with the crystal, its effects are represented by the addition of an electrical impedance $z_{He} = r_{He} - ix_{He}$ in series

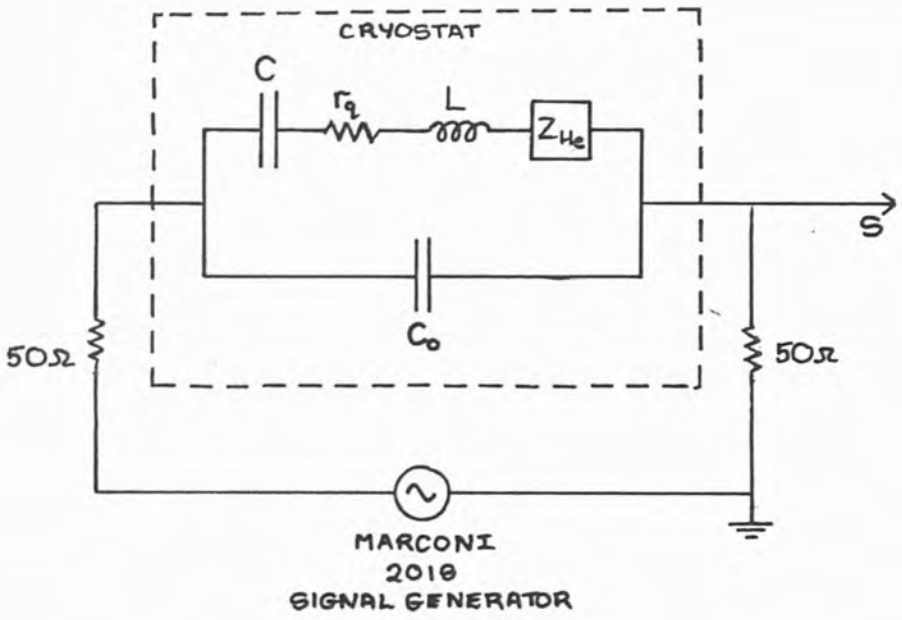

Figure 3.2

Electrical representation of the transmission circuit.

with the LCr_q impedances in Figure 3.2. The electrical impedance z_{He} is proportional to Z, the acoustic impedance of the helium and is therefore temperature dependent.

The electrical impedance z_e of the equivalent circuit of the crystal in contact with helium at frequency f, with $\omega = 2\pi f$, is given by

$$\frac{1}{z_e} = i\omega C_o + \frac{1}{r_s + i(\omega L - 1/\omega C)} \tag{3.3.3}$$

where $r_s = r_q + r_{He}$ and L and C now include the effects of the helium embodied in the term x_{He}. Introducing the figure of merit of the circuit, $M = 1/\omega C_o r_s$, the electrical impedance becomes

$$\frac{z_e}{r_s} = \frac{1 + iM\left[\frac{\Delta f}{\Delta f_p} - \left(\frac{\Delta f}{\Delta f_p}\right)^2 - \frac{1}{M^2}\right]}{\frac{1}{M^2} + \left(1 - \frac{\Delta f}{\Delta f_p}\right)^2} \tag{3.3.4}$$

where $\Delta f = f - f_s$ and $\Delta f_p = f_p - f_s$.

If M is large, the effects of the shunt capacitance C_o can be neglected and the complete circuit behaves as a simple series resonant circuit with resonant frequency $f_s = (2\pi\sqrt{LC})^{-1}$ and quality factor Q given as

$$\frac{1}{Q} = \frac{1}{Q_o} + \frac{1}{Q_c} + \frac{1}{Q_{He}} \tag{3.3.5}$$

where the contributions to the measured Q arise from the crystal, the circuit and the helium respectively.

Q was deduced from the power developed across the 50Ω load to the right of the crystal in Figure 3.2. The d.c. signal S is the output of a Marconi-Saunders diode and is proportional to the power P in the circuit. Therefore, from Figure 3.2

$$\frac{S}{S_o} = \frac{P}{P_o} = \left|\frac{100}{100 + z_e}\right|^2 \qquad (3.3.6)$$

where P_o and S_o are the power and signal when $z_e = 0$, i.e., when the crystal is shorted out of the circuit. At series resonance, $z_e = r_s$ and the signal S_s is given by

$$\frac{S_s}{S_o} = \left|\frac{100}{100 + r_s}\right|^2 \qquad (3.3.7)$$

Since the Q of an a.c. circuit is inversely proportional to the resistance in the circuit, we have

$$\frac{1}{Q} = \frac{r_s + 100}{\omega_s L} = AS_s^{-\frac{1}{2}} \qquad (3.3.8)$$

where A is a constant that can be determined from the transmission resonance curve, Figure 3.3.

The diode detector is designed to have a square law response (i.e., the output voltage is directly proportional to the input power) up to 30 mV. In general, however, $S \alpha P^n$ where $n \simeq 1$ and Figure 3.4 shows the response of the diode as a function of circuit power (in dBm) for the 3rd, 5th and 7th harmonics of the crystal and $n = 0.995$, 0.997 and 1.000 respectively for $S < 7$ mV. During the measurements, therefore, S was kept below this value, and the error in assuming S directly proportional to P was negligible.

As explained in section 3.3.2, the feedback system locks on to

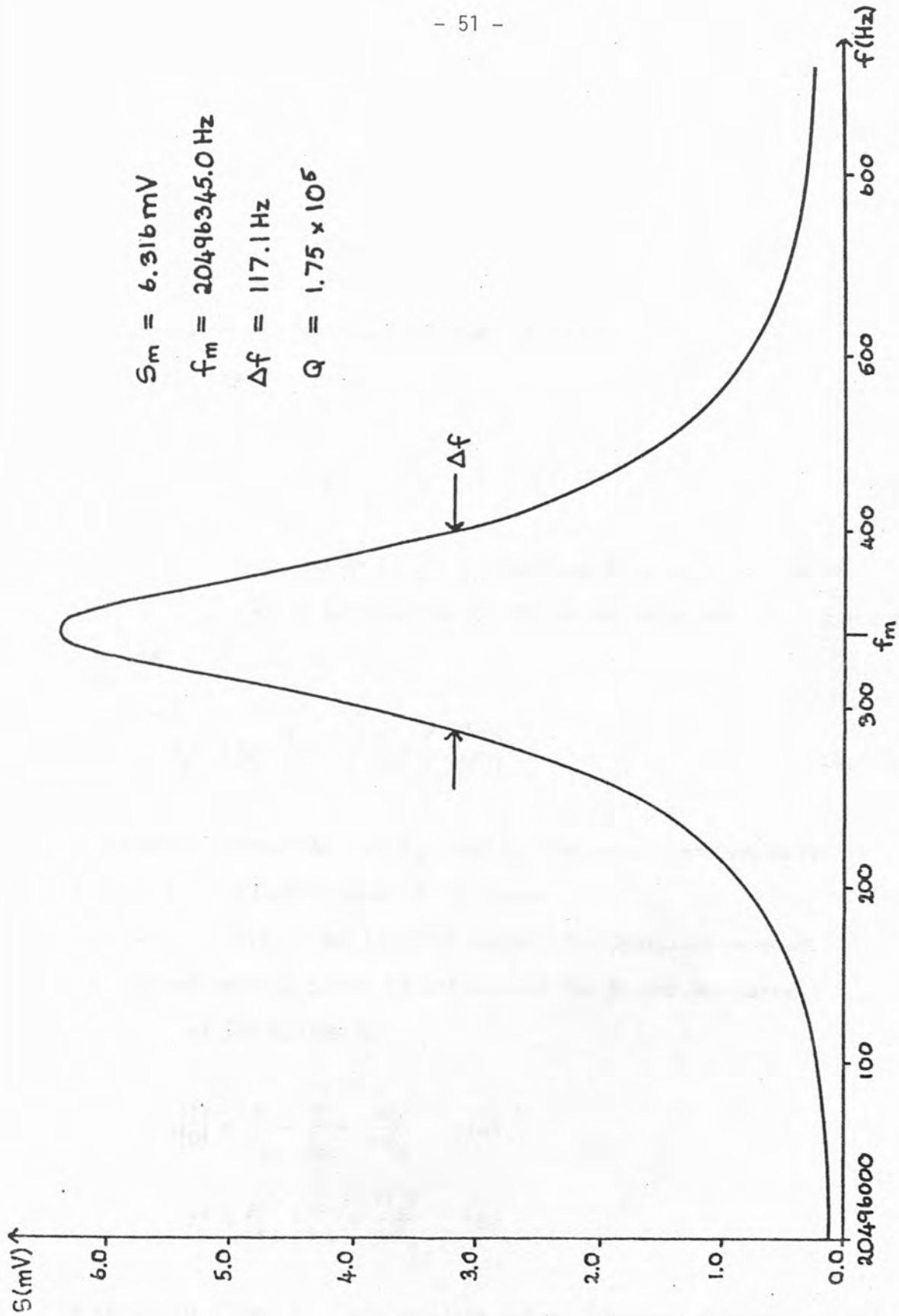

Figure 3.3

The signal S as a function of frequency, showing the resonance of the crystal at 20.5 MHz at 4.2 K in vacuum.

the frequency f_m of maximum signal S_m. The presence of the shunt capacitance C_o in the crystal equivalent circuit however, means that f_m and Q_m are not equal to f_s and Q_s, the series frequency and quality factor of resonance used in calculation of R and X (equations (2.2.9) and 2.2.10)). The frequency f_m is found from the condition $dS/df = 0$ where S is given by equation (3.3.6). Ignoring terms of $1/M^4$ and smaller

$$f_m - f_s = -\frac{\Delta f_p}{M^2}\,\frac{(r_s + 200)}{r_s} \tag{3.3.9}$$

The measured quality factor, Q_m, calculated from S_m, is similarly different from that to be expected for the series resonant LCr_s circuit, Q_s, and

$$Q_s^{-1} = Q_m^{-1}\left[1 + \frac{1}{M^2}\,\frac{(r_s + 200)}{(r_s + 100)}\right] \tag{3.3.10}$$

These circuit corrections to f_m and Q_m are small, particularly for Q_m, and are negligible when M is large.

Equations (2.2.9) and (2.2.10) express the change in resonant frequency and quality factor of the crystal due to the impedance $Z = R - iX$ of the helium as

$$\Delta\left(\frac{1}{Q}\right) = \frac{1}{Q_s} - \frac{1}{Q_o} = \frac{4R}{n\pi R_q} \qquad \text{(a)}$$

$$\Delta f = f_{so} - f_s = \frac{2f_s X}{n\pi R_q} \qquad \text{(b)} \tag{3.3.11}$$

The values Q_o and f_{so} are baseline values, obtained when the crystal is not loaded, i.e., when under vacuum or in the mechanical vacuum of superfluid helium at $T \lesssim 0.6$ K, though as noted in Chapter 5, these are not equivalent conditions.

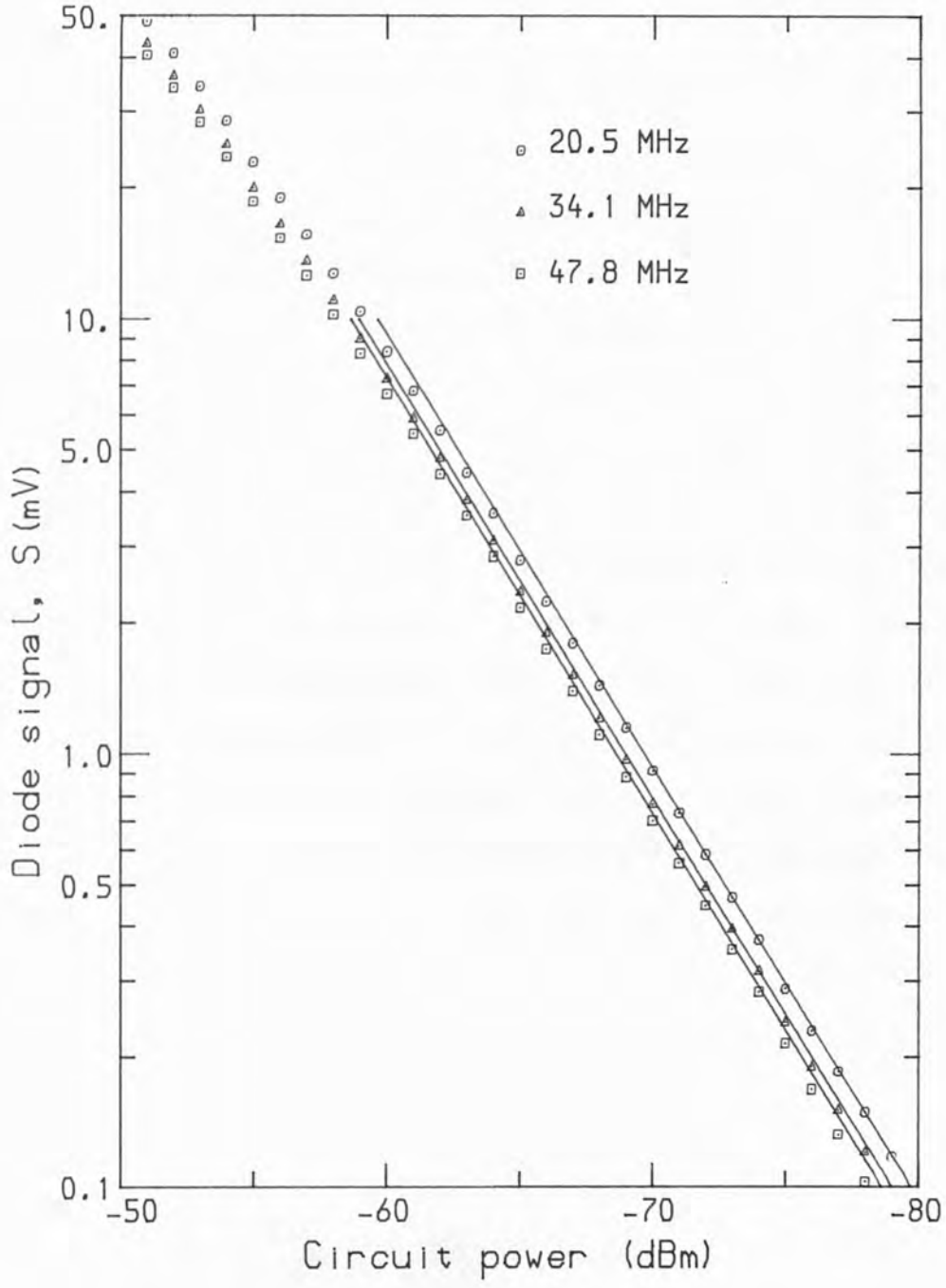

Figure 3.4

Diode detector calibration

3.3.2 The Feedback System

A block diagram of the feedback system used to continuously monitor the resonant frequency and Q-factor of the crystal is shown in Figure 3.1. The Marconi 2018 signal generator, modified to allow the r.f. signal to the crystal to be externally a.c. and d.c. frequency modulated with sensitivity 1 kHz/volt, was driven in continuous wave mode and frequency modulated at a frequency $f_f = 80$ Hz. The signal detected by the diode, S, is proportional to the power in the circuit and is therefore amplitude modulated with an amplitude dependent upon the magnitude of the frequency modulation. This could be made sufficiently small to have negligible effect on the value of S_m. The amplitude modulation of S was phase sensitively detected by a Brookdeal 9503 Lock-in Amplifier whose d.c. output swung positive to negative as the frequency increased, passing through zero at the frequency f_m of maximum signal where $ds/df = 0$. This output was used to d.c. frequency modulate the Marconi signal generator, locking it to the frequency f_m.

The phase ϕ of the crystal changes rapidly at resonance, passing through zero at a frequency f_r defined by $\ell m(z_e) = 0$ and given by

$$f_r - f_s = \frac{\Delta f_p}{M^2}$$

Hence, from equation (3.3.9)

$$f_m - f_r = \frac{2\Delta f_p}{M^2}\left(\frac{r + 100}{r}\right)$$

which is small, ~ 0.8Hz at 20 MHz. The phase of the Lock-in Amplifier is therefore set at that of the circuit when the crystal is at resonance, though in practice the operation of the feedback loop was relatively

insensitive to the phase angle, and over a range of approximately ±15° the lock-in frequency remained constant to the resolution of the measurement, ± 0.1 Hz .

The efficiency of the feedback loop in locking-on to the resonant frequency f_m may be defined in terms of the factor

$$g = \frac{f - f_m}{f_\ell - f_m}$$

where, for a given d.c. frequency modulation signal to the signal generator, f_ℓ is the frequency when the feedback loop is operating and f when it is broken. Thus the higher the value of g, the better the feedback loop operated, with the limit that for high g the system became unstable, oscillating uncontrollably. A suitable compromise was found to be $g \simeq 300$.

The frequency of modulation f_f was chosen such that the decay time of the crystal, $\tau = Q/2\pi f_s < 1/(2\pi f_f)$.

3.4 The Sonic Cell

The basic components of the sonic cell are shown in Figure 3.5. The cell consisted of three blocks of oxygen-free, high conductivity (OFHC) copper, the crystal holder and the thermometer and fill-line blocks, which were bolted onto the main body of the cell, also of OFHC copper. The cell was sealed with indium 'O' rings and suspended from the mixing chamber of a ^{3}He-^{4}He dilution refrigerator. This design made the initial assembly of the cell easier and had the advantage that when the fill line required changing it was not necessary to dismantle the whole cell. Figure 3.5 shows the arrangement used for the film measurements; the base of the tube, diameter 0.5 cm, was 8.5 cm below the crystal and thus limited the film thickness, determined by the

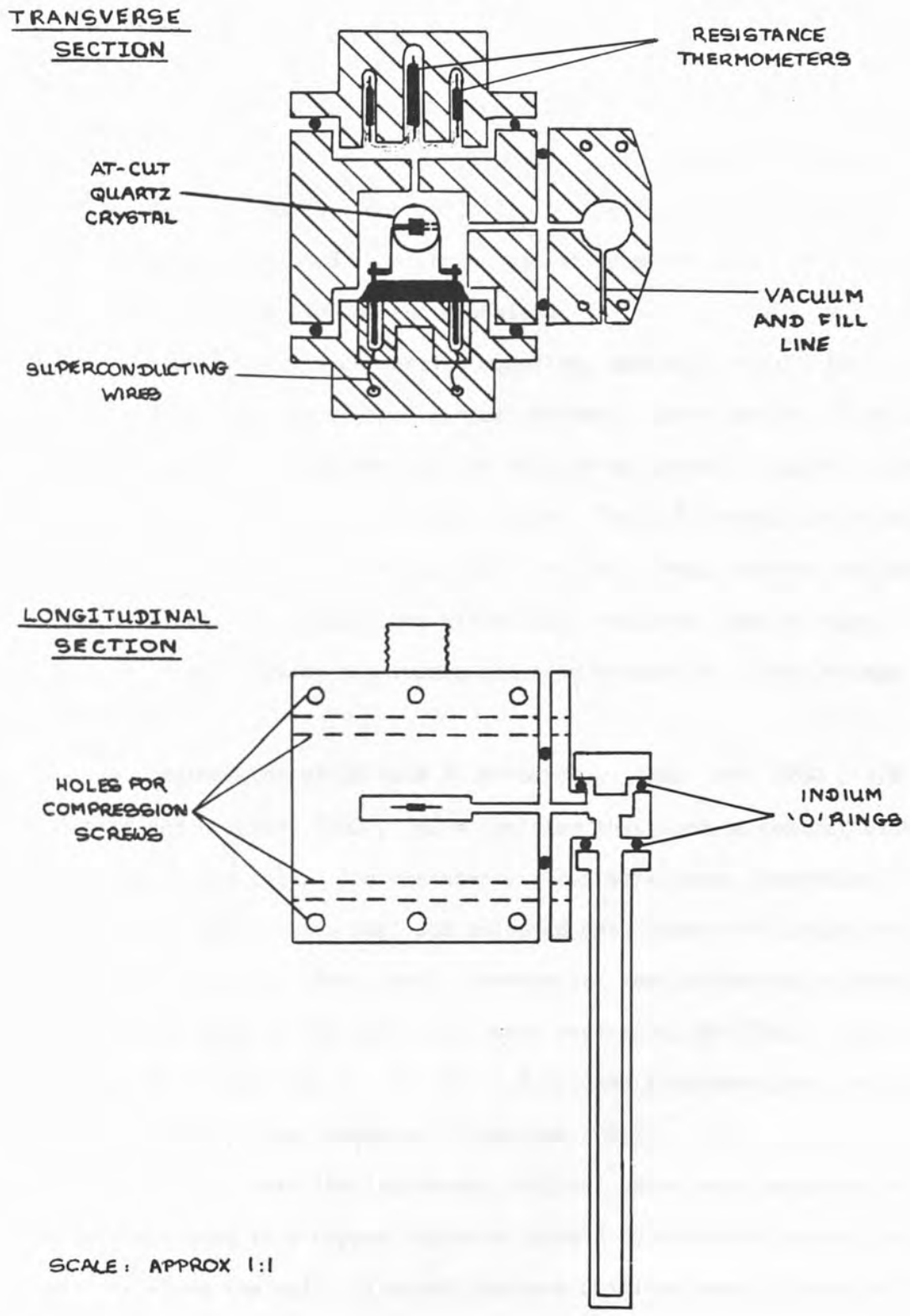

Figure 3.5

Diagram of the sonic cell.

height of the crystal above the surface of the bulk helium condensed in the tube, to greater than $\sim$13 nm. For measurements near the liquid-gas critical point a fill-line block with a small dead volume was used. The fill-line entered the cell horizontally, on the same plane as the crystal, and was enclosed in a vacuum jacket from the level of the mixing chamber to the top of the cryostat.

The crystal, in its commercial mounting, was held rigidly horizontal in the cell body by the crystal contact holder. Short lengths of Niomax CN superconducting wire connected the crystal to co-axial feed-throughs which were sealed with stycast epoxy resin. The r.f. signal was transmitted to and from the crystal by 50Ω co-axial lines running the length of the cryostat; the crystal was effectively isolated from any heat leak down these lines by the superconducting transition of the Niomax wires at 10 K .

The thermometer block held Allen-Bradley 100Ω and 220Ω , 1/8 W resistors and a Speer 100Ω , 1/2 W resistor that were in contact with the helium in the cell. The resistance wires were taken from the cell via a stycast epoxy resin seal and soldered onto stand-offs which were bolted onto the cell. Additional thermometers were thermally anchored to the copper body of the cell; two Speer resistors, R4 (100Ω , 1/2 W , $T < 1$ K), R8 (470Ω , 1/2 W , $1 < T < 4.2$ K) and a carbon-glass resistor ($4.2 < T < 5.2$ K), as discussed in section 3.5.

Measurements near the liquid-gas critical point were conducted with the cell enclosed in a copper radiation shield to minimise temperature gradients along the cell. The cell heaters (bifilar wound constantan wire, 100Ω and 1000Ω) were mounted on the radiation shield and the co-axial cables, all the resistance wires and the fill-line were thermally anchored to it. Long equilibrium times near the gas-liquid critical

point, especially along the vapour pressure curve, meant that a small sample space was an advantage; the total volume of the helium in the cell was estimated as being about 1 cm^3 . Silver sinter, with a high surface area to volume ratio ($\sim 10^6$ m^{-1}) was used for both the critical point and the film measurements to improve thermal contact between the helium and the copper of the cell, to which it was firmly attached.

3.5 Thermometry and the Operation of the Dilution Refrigerator

3.5.1 Temperature $0.3 < T < 3$ K

In brief, the principles of operation of a ^{3}He-^{4}He dilution refrigerator are as follows, a full description is given in many low temperature technique books, e.g., that by Betts (1976). The gaseous ^{3}He-^{4}He mixture is cooled to 1.2 K by contact with the ^{4}He pot and condenses into the dilution unit of the refrigerator. When condensation is complete, the mixture is cooled further by pumping on the still until at $\sim$0.8 K the mixture in the mixing chamber separates into a ^{3}He-rich phase floating on a ^{4}He-rich phase. Cooling now occurs because the ^{4}He-rich phase has superfluid properties and the ^{3}He atoms dissolved in it behave as a Fermi gas. ^{3}He atoms therefore 'evaporate' across the phase boundary into the ^{4}He from the concentrated ^{3}He phase thus cooling the mixture. They are then removed from the still by pumping and subsequently recondensed via a series of heat-exchangers into the mixing chamber.

Under optimum conditions, the lowest temperature attained by this particular fridge is of the order of 30 mK, however, for these experiments there was a large heat leak associated with the fill-line, as explained in section 3.5.3 and the lowest temperature reached was $\sim$300 mK.

Above T_λ , for the normal fluid helium films, the data was taken with only a small amount of ^{4}He in the dilution unit, to act as a thermal link between the ^{4}He pot at 1.2 K and the sonic cell.

For temperature measurement when $T < 4.2$ K , two carbon Speer resistors were used; R4(100Ω $\frac{1}{2}$W) and R8 (470Ω $\frac{1}{2}$W), below and above 1 K respectively, both thermally anchored to the cell. R4 had been calibrated against a CMN magnetic susceptibility thermometer and a Superconducting Reference Material (SRM)767 unit, and R8 was calibrated against a carbon-glass (628) resistor and checked against the saturated vapour pressure of ^{4}He. The calibration curves R(T) for R4 and R8 are shown in Figures 3.6 and 3.7; the curves are a least square fit of the calibration points to the formula

$$\frac{1}{T} = aR + b\sqrt{R} + c \qquad (3.5.1)$$

The resistance of R4 and R8 was measured by an AVS-45 Automatic Resistance Bridge made by RV-Elektronikka Oy of Finland, and fitted with a BCD data transfer option. The excitation voltage of the bridge was variable (range 10-3000 μV) and was chosen so that power dissipation in the sensor did not exceed 10^{-10} W . The bridge's resolution over the resistance range under consideration was 0.1Ω and errors in the measurement of temperature were estimated to be 1.5% for $T < 1$ K and 1% for $T > 1$ K .

A Cryobridge S72 (see section 3.5.2) was used to monitor the resistance of one of the resistances in the cell (AB 100Ω or Speer 100Ω , depending on the temperature) and gave a d.c. output voltage directly related to the difference between the required temperature of the cell - determined by the resistance set on the Cryobridge, and its actual temperature. This error signal was input to an Oxford Instruments Digital Temperature Controller (DTC2) which was capable of proportional, derivative and integral action and regulated the voltage applied to the cell heater. Under ideal conditions, the cell temperature was

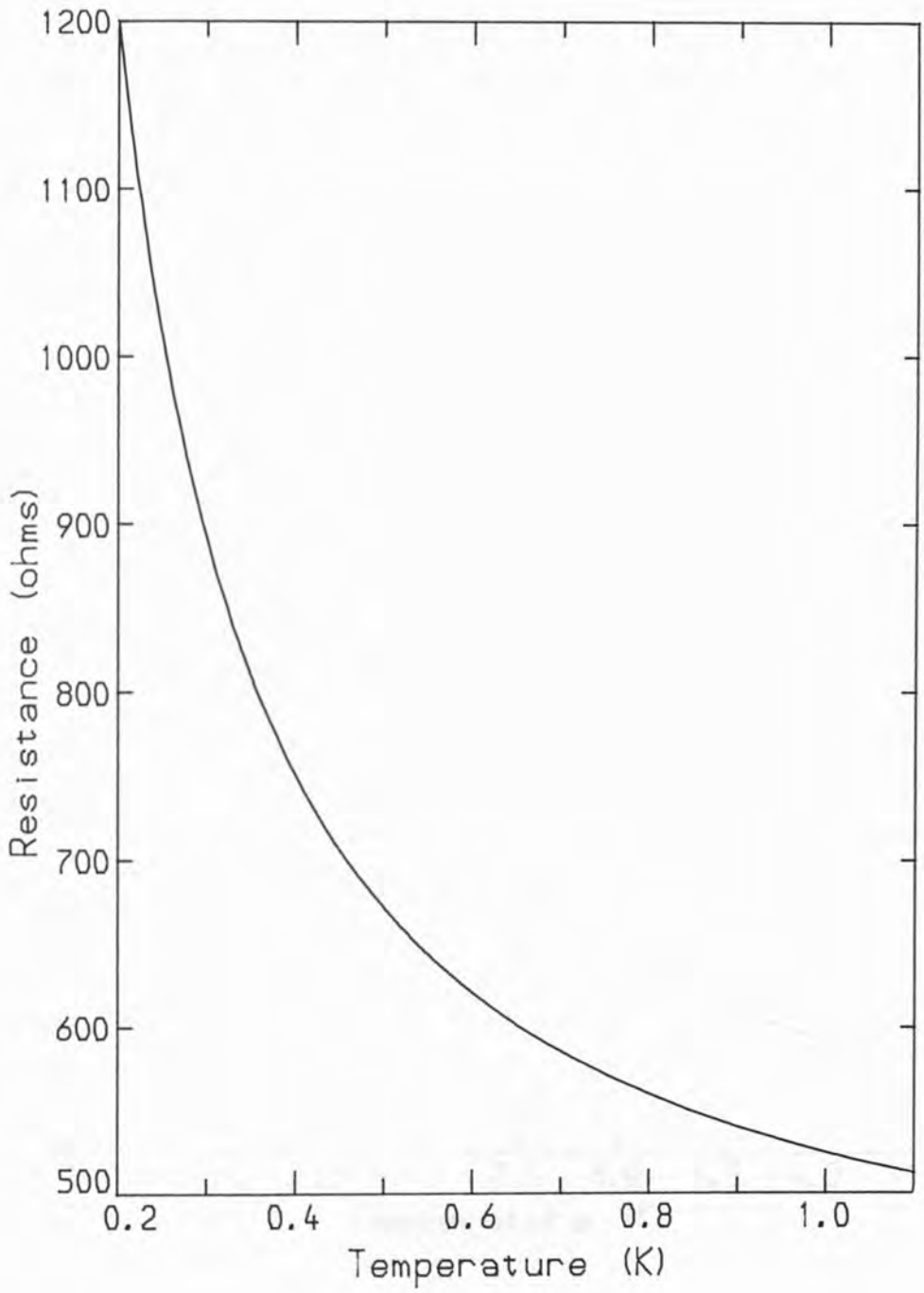

Figure 3.6

Resistance thermometer calibration: R4 .

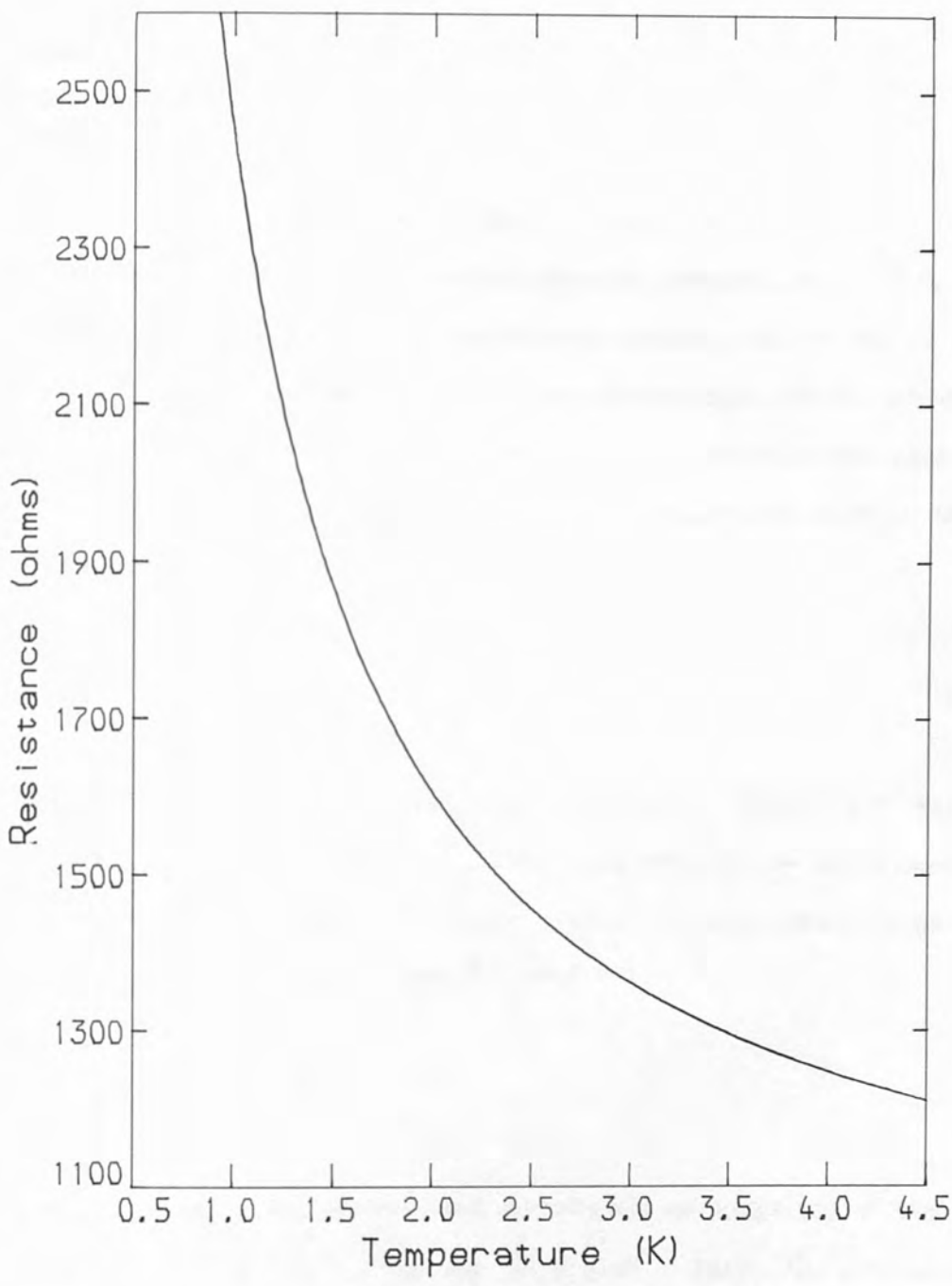

Figure 3.7

Resistance thermometer calibration: R8 .

controlled to within the resolution of the AVS-45 bridge i.e., < 5 mK at 2 K .

3.5.2 Temperature $T \sim 5.2$ K

Measurements near the liquid-gas critical point were also taken using the dilution refrigerator, the 1.2 K pot being filled with helium at 4.2 K and the cell, heated to the required temperature ~ 5.2 K, being thermally linked to the the helium bath by exchange gas in the IVC.

The conduction of heat by a gas between two parallel plates when the mean free path (m.f.p.) of the molecules is less than the separation of the plates ($\lambda << d$) is independent of pressure and given by the kinetic theory as

$$\dot{Q} = -K \, dT/dx \quad Wm^{-2} \tag{3.5.2}$$

where K is the thermal conductivity of the gas, $26 mWm^{-1} K^{-1}$ for ^4He at 4.2 K . Maintaining the cell at 5.2 K in this regime would necessitate a high heat input, $\dot{Q} > 60$ mW , which would create a large temperature gradient along the cell, with

$$\Delta T = \frac{\dot{Q}\ell}{KA} \tag{3.5.3}$$

where $\ell = 5$ cm , $A \simeq 20$ cm^2 and the thermal conductivity of the OFHC copper $K \sim 750 \; Wm^{-1} K^{-1}$, giving $\Delta T = 2$ mK . Hence low pressures where $\lambda >> d$ and the kinetic theory equation (3.5.2) is no longer appropriate must be used (Rose-Innes, 1973)

$$\dot{Q} = 300 \, aP \, \Delta T \; Wm^{-2} \tag{3.5.4}$$

where P is the exchange gas pressure in torr and a is the accommodation coefficient ($a < 1$, its exact value depending on the surface of the plates). At 4.2 K, $\lambda \alpha 1/P$ and the mean free path of ^{4}He molecules at $10^{-3}\tau$ is 1 mm. Figure 3.8 shows $\dot{Q}/\Delta T$ versus exchange gas pressure for the cell at .5 K, and the transition from the kinetic region where $\dot{Q}$ is independent of pressure, to the low pressure region is evident. An exchange gas pressure of $\sim 4 \times 10^{-4}$ torr was chosen, giving a thermal response time for the cell of $\sim$20 s; this was deemed an acceptable compromise between the fast response time of high exchange gas pressure and large heat input, and a slow response time with low heat input.

Temperatures above 4.2 K were measured using a carbon-glass resistor that was calibrated against the s.v.p. of ^{4}He on the T(58) temperature scale using the equation given by McCarty (1973). McCarty imposed the constraints $T_c = 5.1994$ K and $P_c = 1718\ \tau$ on his equation, whereas Kierstead (1971) gives $T_c = 5.1899$ and $P_c = 1706.1\ \tau$. On McCarty's T(58) scale, $1706\ \tau$ corresponds to $T = 5.190$ K. The critical temperature and pressure were therefore taken as Kierstead's values, the carbon-glass resistor was not calibrated for pressures higher than $1706\ \tau$ and the resulting temperature/resistance calibration fitted to the expression

$$\ell n\ (T) = \sum_n A_n\ (\ell nR)^{n-1}$$

is shown in Figure 3.9. For $T > T_c$, where the resistor is not calibrated, the temperature is estimated by extrapolating the above equation.

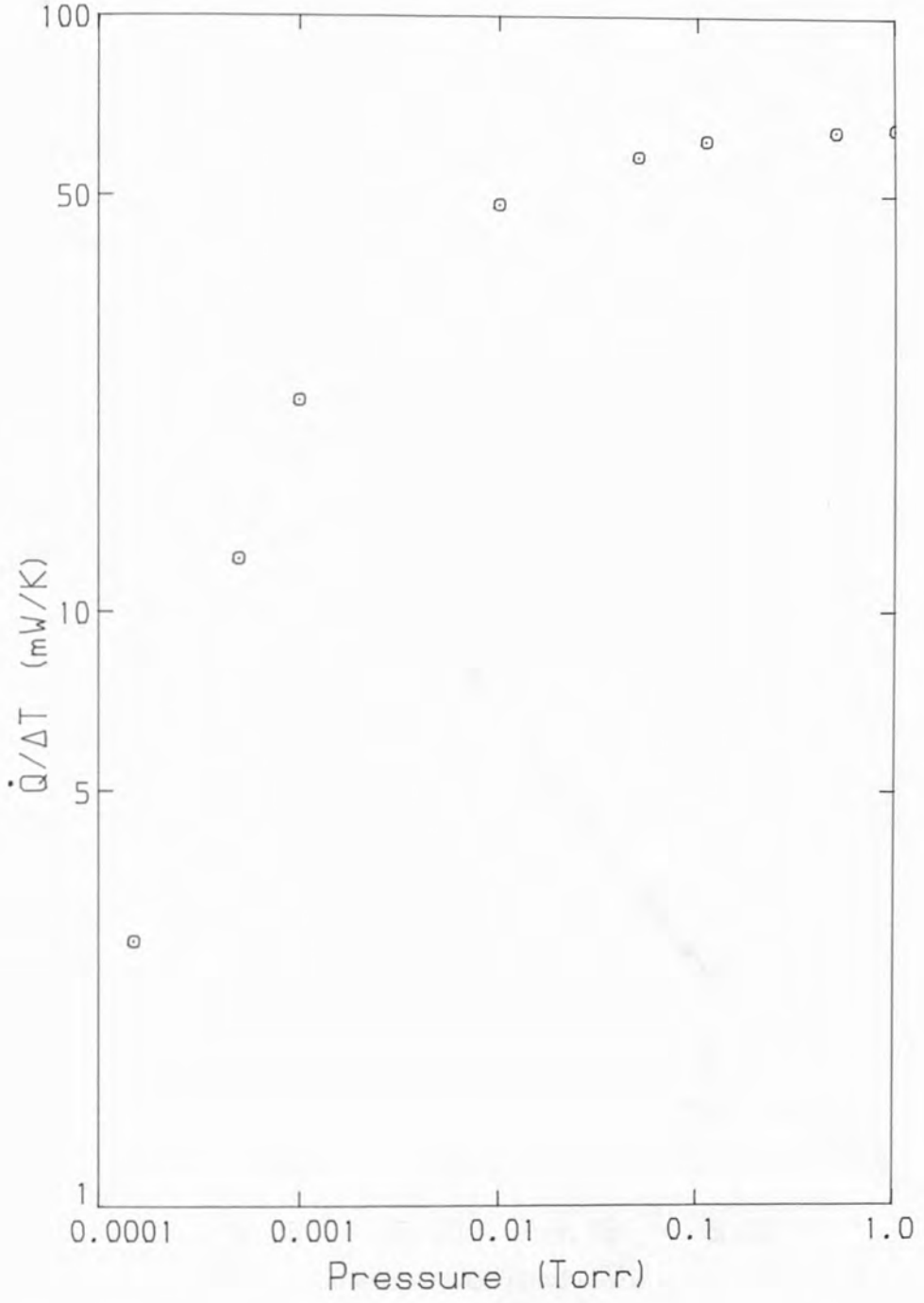

Figure 3.8

$\dot{Q}/\Delta T$ versus exchange gas pressure for the cell at 5 K .

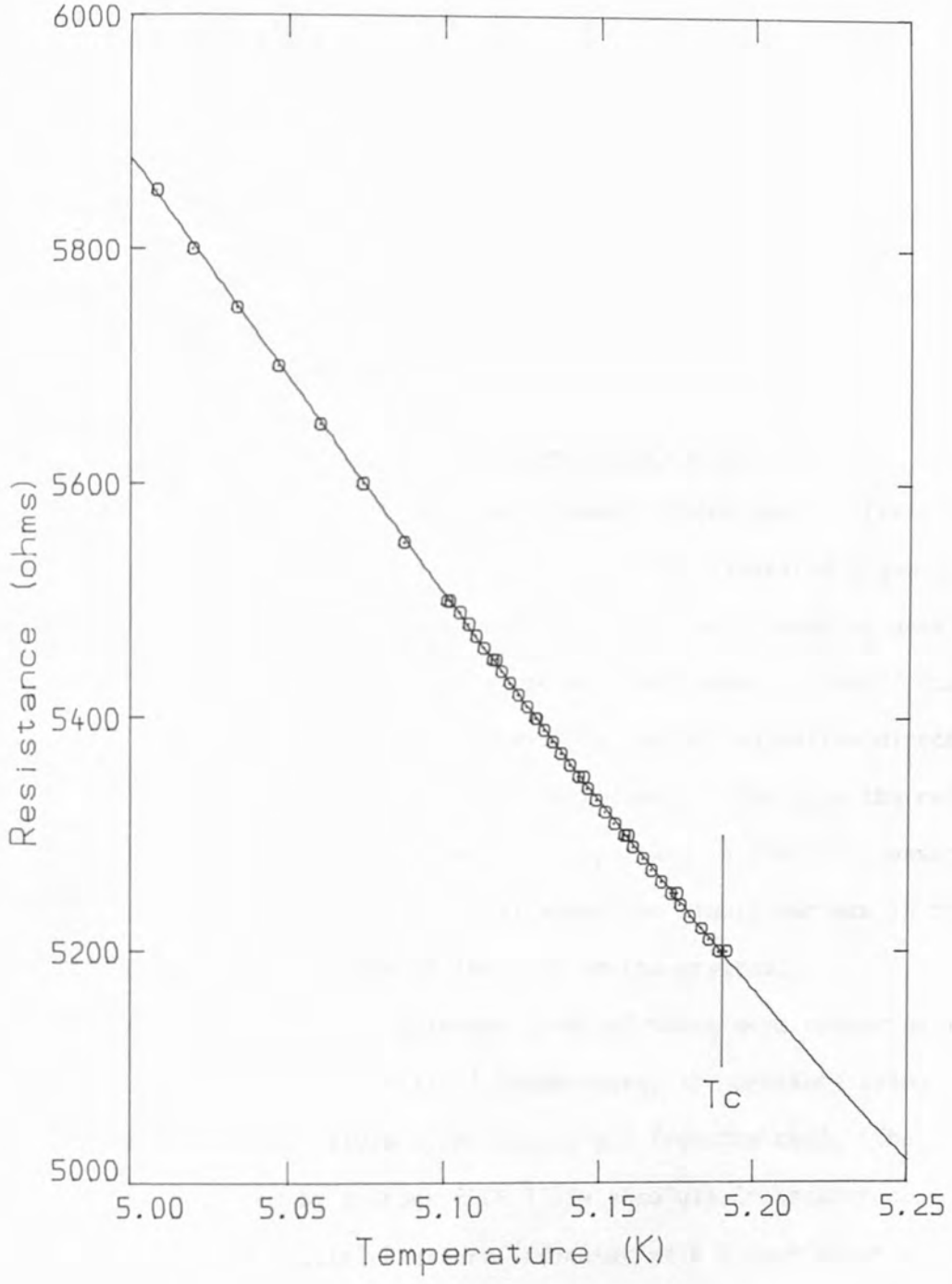

Figure 3.9

Calibration for the carbon-glass resistance thermometer.

The resistance of the carbon-glass thermometer was measured with a Cryobridge S72 (manufactured by the Czechoslovak Academy of Science). This is essentially an a.c. Wheatstone bridge with built-in comparative resistances and a resolution of 1Ω . Errors in temperature determination were estimated to be $< 0.05\%$ for $T < Tc$. Temperature was controlled as described above, using the DTC2 temperature controller.

3.5.3 The Gas Handling and Pressure Measurement System

The gas handling and pressure measurement system used in these experiments is shown schematically in Figure 3.10. Research grade ^4He gas was taken from the high pressure cylinder, twice cleaned by passing it through liquid N_2 cooled molecular seives and stored in the 2ℓ dump on the high pressure side of the system. By condensing helium directly from the 2ℓ dump into the sonic cell, the volume of liquid in the cell could be estimated. This was especially important in the film measurements, since the height of the crystal above the liquid surface in the tube determines the thickness of the film on the crystal.

Measurements near the liquid-gas critical point were conducted in the fluid region above the critical temperature, the pressure being swept at constant temperature by releasing gas from the cell. The pressure was measured by a Druck PDCR 110/W absolute transducer connected to a DPI 101 Digital Pressure Indicator with a resolution of $0.1\ \tau$. Data was recorded over the range $0\text{-}2000\ \tau$ ($P_c = 1706\ \tau$). The accuracy of the pressure measurement was limited by the linearity of the DPI to $\sim 0.8\ \tau$.

The dilution refrigerator originally had a capilliary fill line which was thermally anchored to the 1.2 K ^4He pot and to the fridge heat exchangers. For the measurements reported here, this was replaced

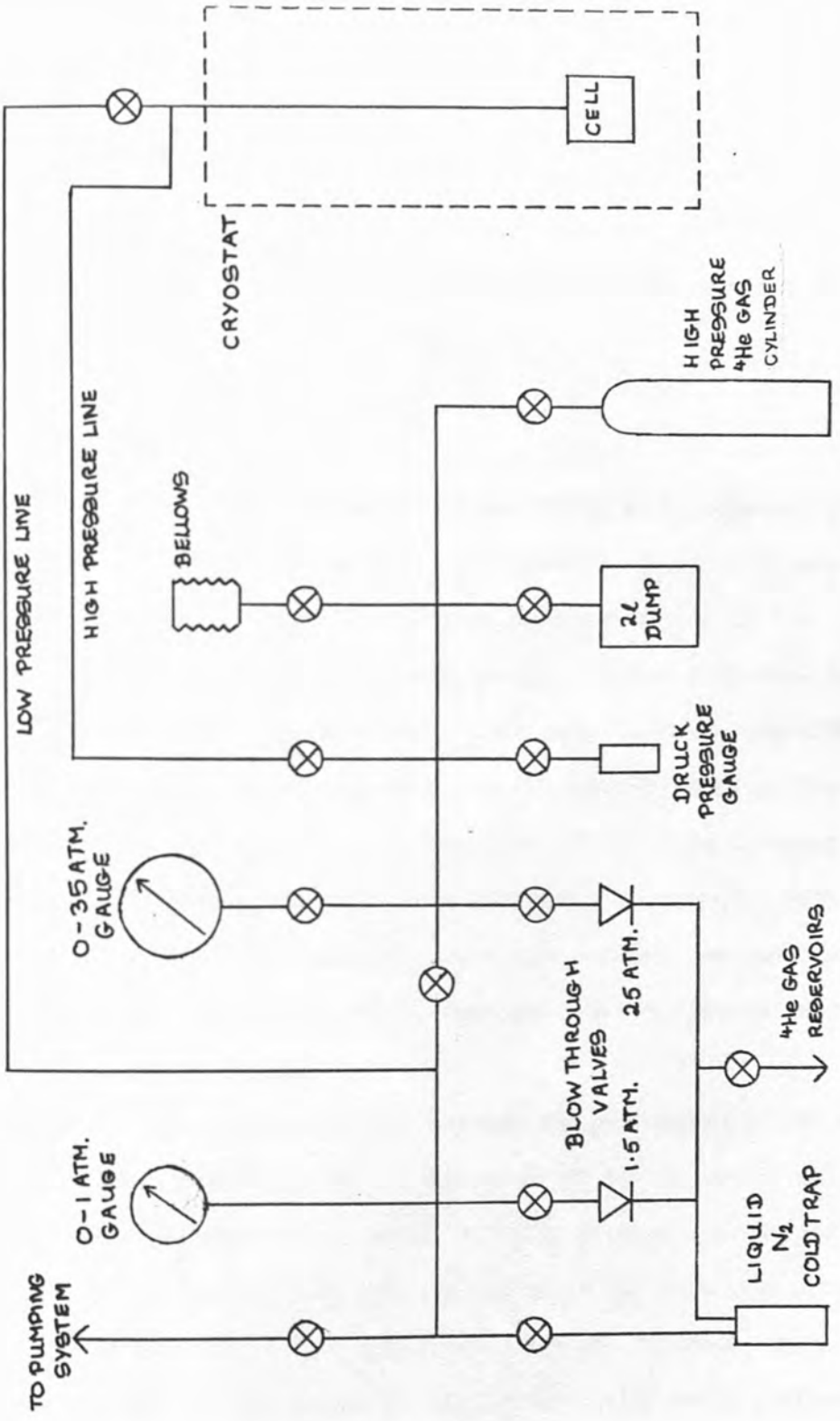

Figure 3.10

Gas handling and pressure measurement system.

by a vacuum jacketed fill line so the temperature gradient along the length of the line was always the same sign. This reduces hydrostatic head errors in the measurement of the pressure and prevents condensation of helium in the neighbourhood of the ^{4}He pot when its temperature is lower than that of the cell. Unfortunately, there was a large heat leak associated with this fill line limiting the minimum temperature attainable by the fridge to $\sim$300 mK .

3.6 Data Acquisition

Data was recorded by a Hewlett-Packard HP9816 microcomputer, a schematic diagram of the data acquisition system is given in Figure 3.11. A disc drive and dot-matrix printer were interfaced to the microcomputer using the Hewlett-Packard General Purpose Interface Bus (GPIB) which follows IEEE conventions. Also interfaced via the GPIB were the Marconi 2018 signal generator and the Keithley 195A multimeter used for measuring the signal S . These devices could be accessed directly by the HP9816 using their IEEE commands. Instruments with interfaces other than GPIB compatible were accessed via the two control and interface boxes, AKB-1 and AKB-2, designed and manufactured by the college electronics workshop.

The AKB-1 acted as an interface between the microcomputer and the Philips PM6615 frequency counter and the Druck DPI101 pressure indicator, interpreting the controller's commands to these devices and, on its request for data, scanning them and placing their BCD data into a buffer. The contents of the buffer, the individual readings separated by a colon (:), are then sent in IEEE format to the microcomputer where software separates the two values. In addition to this, the AKB-1 could also function as a pressure controller, pulses from it controlling, via a stepwise motor, the movement and direction of movement of bellows in

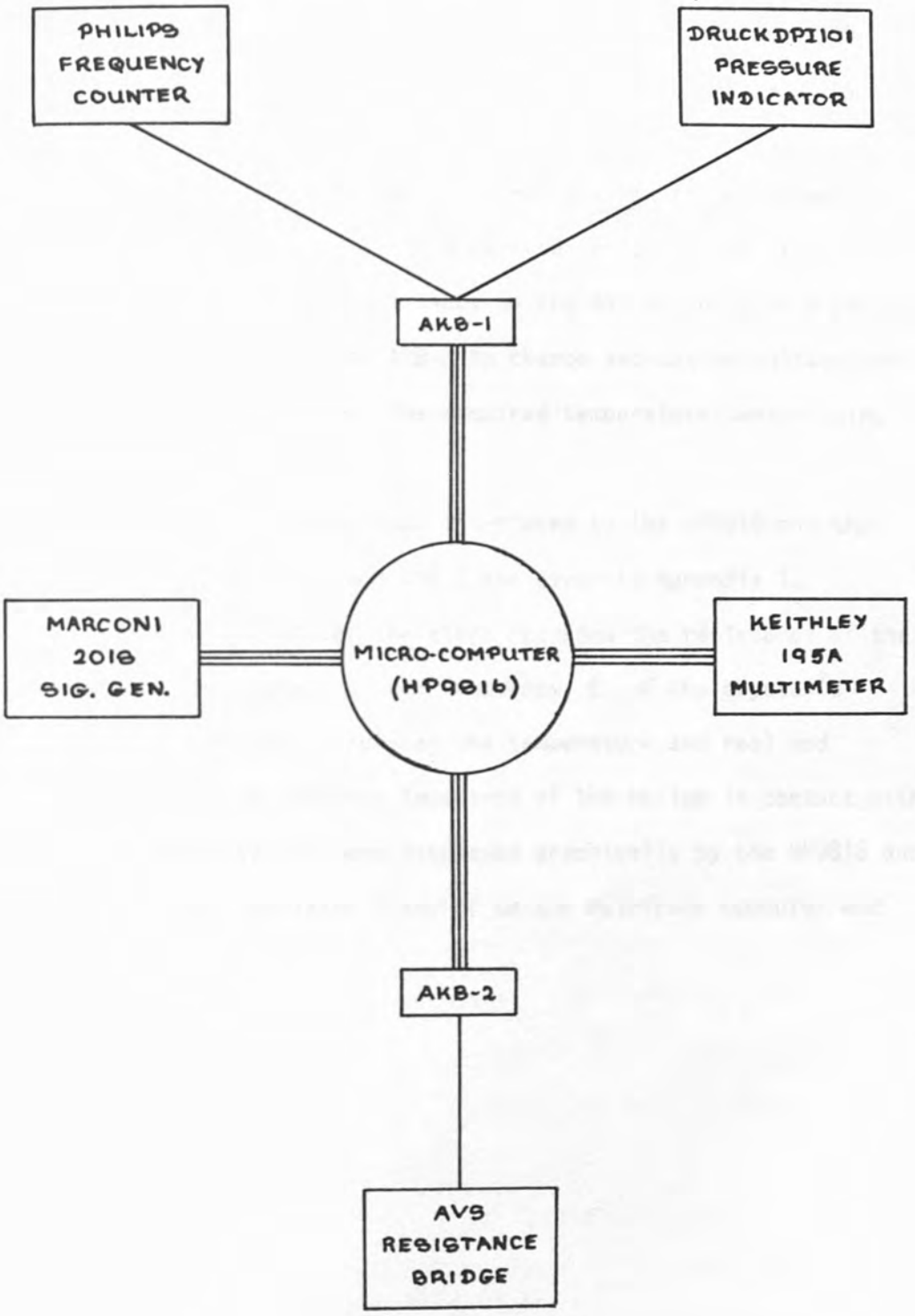

Figure 3.11

Schematic diagram of the system used for data acquisition.

the gas handling system. The frequency of the pulses and hence the bellow's speed of movement could be selected either manually or by the HP9816.

The AVS-45 resistance bridge was interfaced to the microcomputer by the AKB-2, this converted its BCD representation of the data into IEEE format. Additional control lines to the AVS-45 could be accessed from the microcomputer via the AKB-2 to change excitation voltage and resistance range and to select the required temperature sensor using the multiplexer option.

The addresses for the devices interfaced to the HP9816 and the command codes for the AKB-1 and AKB-2 are given in Appendix 1.

The HP9816 microcomputer therefore recorded the resistance of the thermometer and the signal S and frequency f of the crystal's resonance, and from them calculated the temperature and real and imaginary parts of the acoustic impedance of the helium in contact with the crystal. These values were displayed graphically by the HP9816 and were stored on disc for later transfer to the mainframe computer and further processing.

Chapter 4

Helium Films: $T > T_\lambda$

4.1 Introduction

A known amount of helium at room temperature was condensed into the cell, partially filling the tube with liquid such that the crystal was a predetermined height h above the liquid surface. The film that forms upon the crystal due to van der Waals' forces has an equilibrium thickness that can be estimated from the van der Waals' form of the potential;

$$\frac{AK_b}{d^3} = m\ g\ h$$

with $A \simeq 40$ K . The film however, need not be of the equilibrium thickness given by this equation. As explained in the following section, a temperature difference between the crystal and the liquid in the tube causes the film to evaporate or condense. By deliberately creating such a temperature difference, it is therefore possible to sweep the thickness of the film from a few atoms to effectively a bulk liquid.

The effect on the measured impedance of the changing position of the liquid-vapour interface as the film thickness is swept can be deduced by solving the transmission line equations of Chapter 2 for the specific case of a homogeneous film (section 4.3).

The density profile of the helium film adsorbed on the crystal is discussed in section 4.4 and measurements of the film's impedance at 20 MHz, 3.11 K (Spencer, Lea and Fozooni, 1985), 2.78 K and 2.33 K are presented in section 4.5.

4.2 Sweeping the Film Thickness

The thickness of the film adsorbed on the crystal resonator is determined by the height of the crystal above the level of the helium liquid in the tube attached to the cell. Equation (2.5.3) shows that for the crystal in an isothermal cell and at a given height h above the liquid level, the adsorbed film will have a well defined thickness d, that depends solely upon the form of the potential $V(d)$. If, however, a temperature difference ΔT is created between the crystal and the liquid in the tube, equation (2.5.2) for the chemical potential V_c becomes

$$V(d) = - V_c = -m\,g\,h - K_b\,T_o\,\ell n\left[\frac{P_o(T_x)}{P_o(T_o)}\right] \qquad (4.2.1)$$

where $P_o(T_o)$ is the saturated vapour pressure of the liquid at temperature T_o and $P_o(T_x)$ is the svp at the crystal's temperature, T_x. A positive temperature difference, $T_x > T_o$ increases the svp of the liquid of the film while, to a first approximation, the temperature of the liquid in the tube and hence the vapour pressure over the film remains constant. The film is therefore no longer in equilibrium, helium evaporates from it, and its thickness is reduced. The process is reversed for $T_x < T_o$, helium vapour condenses and the film rapidly thickens to become effectively a bulk liquid ($d \gg \delta$, the penetration depth of the wave in the film). Figure 4.1 shows the change in film thickness for a temperature difference ΔT between the crystal and the liquid in the tube at 3 K, for an equilibrium film thickness of 20 nm.

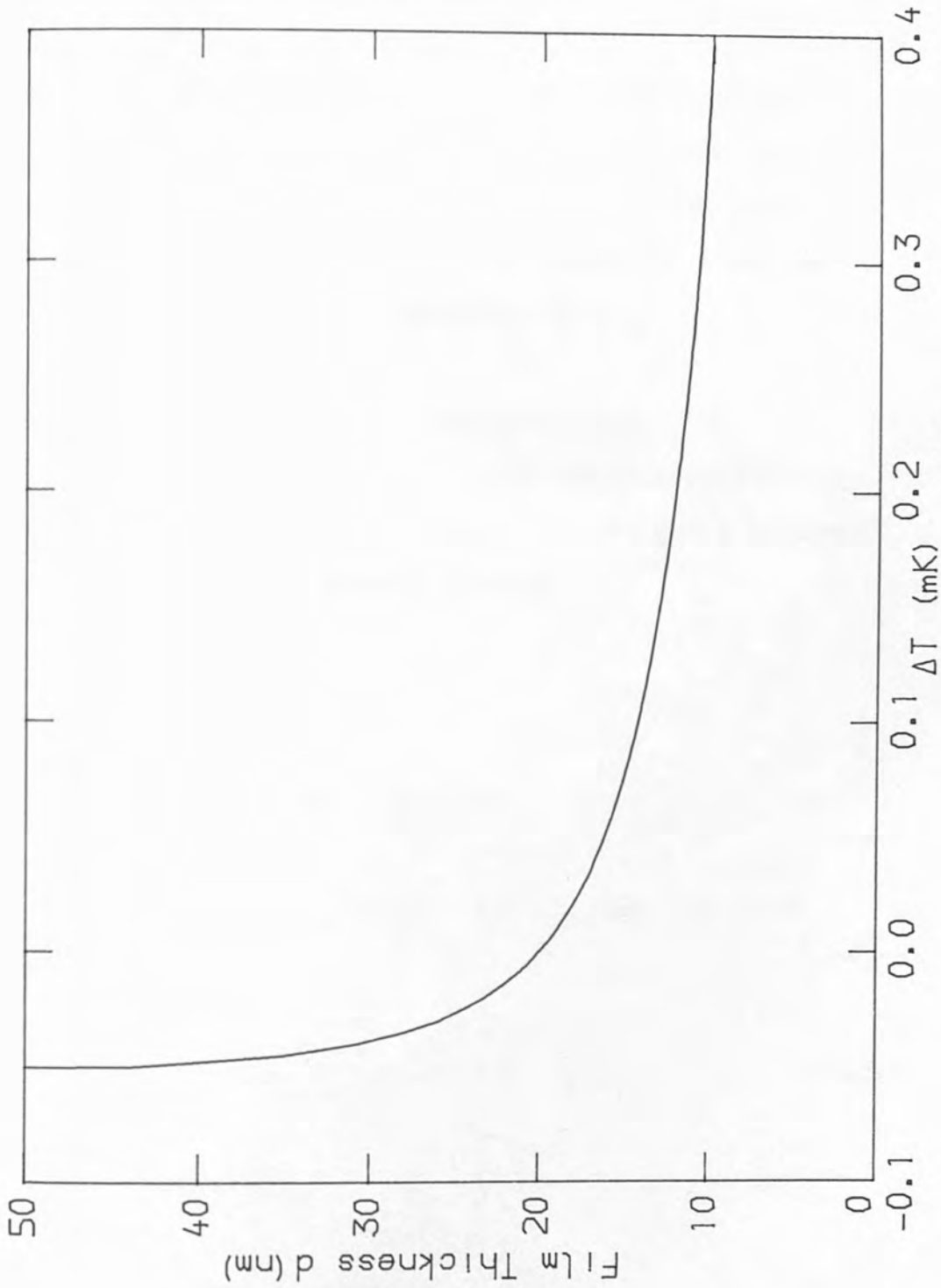

Figure 4.1

The change of film thickness d with temperature difference $\Delta T = T_x - T_o$ between the crystal and the bulk liquid helium below it, for a film of equilibrium ($\Delta T = 0$) thickness 20 nm at 3 K .

The temperature of the cell was locked to the required value using the temperature controller, both resistance thermometer and heater being mounted on the cell body holding the crystal as described in section 3.4. The copper body of the cell, with the crystal and its helium film therefore reacted rapidly to an abrupt change in the heat input to the system, the thermal inertia of the liquid in the tube being sufficient to ensure the formation of ΔT .

4.3 Transmission Line Theory for a Homogeneous Film

A homogeneous film of thickness d adsorbed on the crystal surface at $x = 0$ and with its free surface in contact with a homogeneous, viscous vapour has a local impedance given by

$$z(x) = (1 - i)\,(\omega\rho_f\eta_f/2)^{\frac{1}{2}} = (1 - i)r \qquad 0 < x < d$$

$$= (1 - i)\,(\omega\rho_v\eta_v/2)^{\frac{1}{2}} = (1 - i)r_v \qquad x > d$$

The impedance measured by the crystal, $Z(0)$ is therefore, from equation (2.4.7),

$$Z(0) = (1 - i)r \tanh(\psi + \gamma d) \tag{4.3.1}$$

where

$$\tanh(\psi) = r_v/r$$

Simplifying this gives the equation

$$Z(0) = (1 - i)r\,\frac{r_v/r + \tanh(1 - i)d/\delta}{1 + r_v/r \tanh(1 - i)d/\delta} \tag{4.3.2}$$

where δ is the penetration depth of the wave in the film.

For a film in a vacuum, $z_v = (1 - i)r_v = 0$ and

$$Z(0) = (1 - i)r \tanh(1 - i)d/\delta \tag{4.3.3}$$

In this case, the real and imaginary parts of $Z(0)$, R and X can be written as

$$\frac{R}{r} = \frac{\sinh(2d/\delta) - \sin(2d/\delta)}{\cosh(2d/\delta) + \cos(2d/\delta)} \qquad \text{(a)}$$

$$\frac{X}{r} = \frac{\sinh(2d/\delta) + \sin(2d/\delta)}{\cosh(2d/\delta) + \cos(2d/\delta)} \qquad \text{(b)} \tag{4.3.4}$$

and are plotted in Figure 4.2 as functions of d/δ. As d increases, R and X increase and pass through a series of heavily damped maxima and minima corresponding to standing waves in the film. For $d/\delta \gg 1$, the measured impedance $Z(0)$ tends towards that of the bulk homogeneous liquid. This behaviour is shown in the Argand diagram of Figure 4.5, with X plotted versus R; the locus of $Z(0)$ is a spiral starting at $Z/r = 0$ and rapidly converging to the bulk value, $Z = (1 - i)r$.

When the film is very thin, $d/\delta \ll 1$, equation (4.3.4) gives $R = 0$ and $X = 2rd/\delta = \rho\omega d$ i.e., the measured impedance is purely imaginary,

$$Z(0) = -i\omega\rho d \tag{4.3.5}$$

From equation (2.2.8) this gives a change in the resonant frequency of the crystal of

$$\Delta f = -\frac{4f^2\rho d}{nR_q} \tag{4.3.6}$$

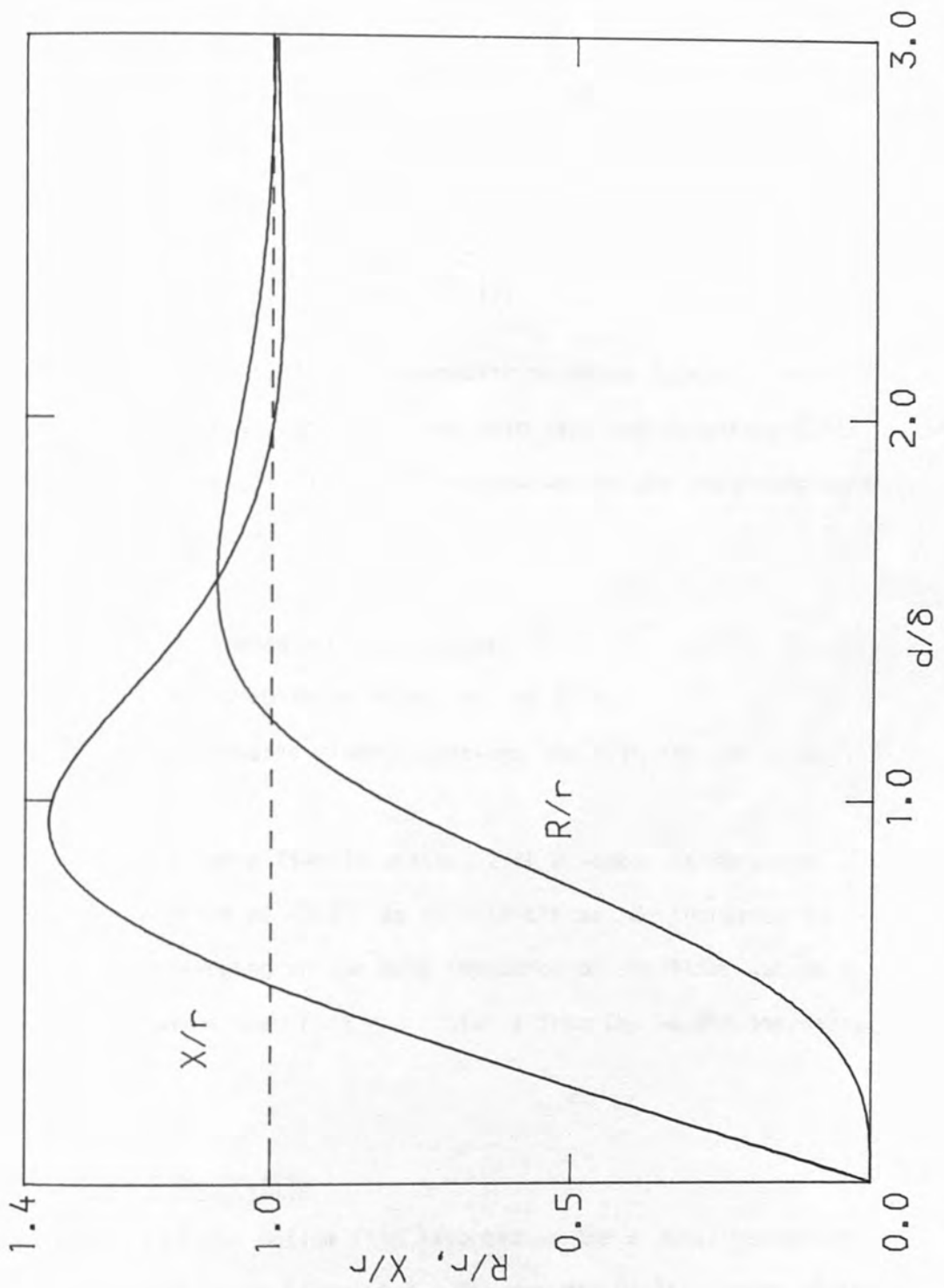

Figure 4.2

The real and imaginary parts, R and X, of the transverse acoustic impedance of a film, thickness d, in vacuum. The bulk liquid has an impedance (1 - i)r and δ is the penetration depth of the viscous wave.

which is the microbalance equation (2.2.2) with $\sigma = \rho d$ being that portion of the film which vibrates without slip with the crystal.

If the thin film is in contact with helium vapour of impedance $Z_v = (1 - i)r_v$,

$$Z(0) - Z_v = - i\omega\sigma\left[1 - \left(\frac{r_v}{r}\right)^2\right] \qquad (4.3.7)$$

and the term $(1 - (r_v/r)^2)$ is an acoustic mismatch factor. The measured impedance $Z(0)$ therefore has both real and imaginary parts, the real part being equal to that of the vapour and the imaginary part having three contributions:

i) from the impedance of the vapour;

ii) from the microbalance effect of the film;

iii) from the acoustic mismatch between the film and the vapour.

The Argand diagram for a film in contact with a vapour is shown in Figure 4.5. The locus of $Z(0)$ as film thickness d increases is again a spiral converging on the bulk impedance of the film, but to a good approximation, since $r >> r_v$, starts from the vapour impedance $z_v = (1 - i)r_v$.

4.4 The Helium Film Profile

The profile of the helium film adsorbed on the crystal resonator is shown schematically in Figure 4.3. The van der Waals' forces of the crystal cause, in the vicinity of the solid/liquid interface, an enhancement in the pressure and density of the fluid above the 'bulk' values. A layer model is often used to describe the adsorption of helium on a

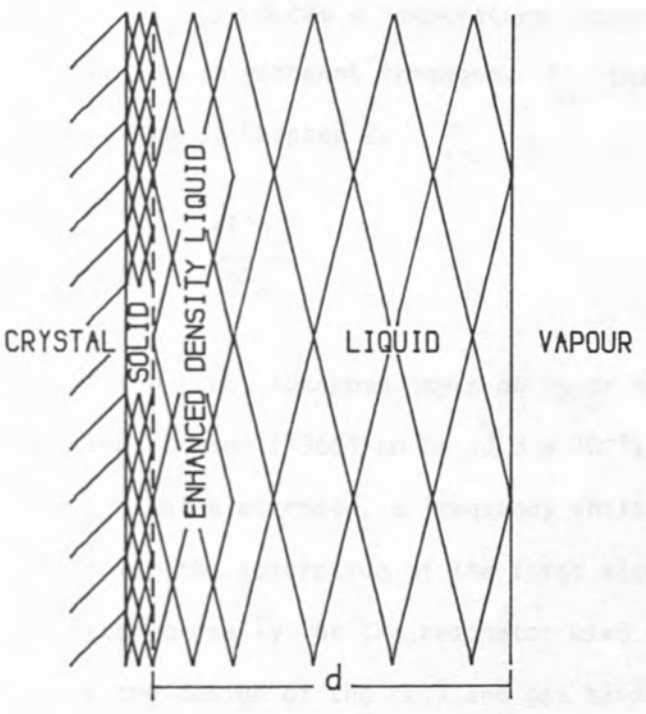

Figure 4.3

The profile of a ^{4}He film, thickness d , adsorbed on the crystal, showing the localised atomic layer and the region of enhanced density liquid caused by the van der Waals' forces.

substrate; the first atomic layer of statistical thickness 3.6 Å is considered to be localised on the substrate with successive layers consisting of helium liquid under high pressure. The atomic layer is assumed to be localised on the crystal electrodes at low pressures with a binding energy of 211 K as given by Ezell, Pollock and Daunt (1981) for ^{4}He atoms on a gold substrate. This adsorbed solid layer, of mass per unit area σ_ℓ produces a temperature independent frequency shift relative to the vacuum resonant frequency f_o that is given by the microbalance equation of Chapter 2:

$$\Delta f_\ell = f_s - f_o = - \frac{4f^2\sigma_\ell}{nR_q}$$

The areal density of the first adsorbed layer on Vycor has been given by Brewer, Symonds and Thomson (1966) to be $7.3 \times 10^{-8} kgm^{-2}$, giving, if adsorbed on the crystal electrodes, a frequency shift $\Delta f_\ell = - 5$ Hz . This frequency shift for the adsorption of the first atomic layer has not been verified experimentally for the resonator used in the studies reported here, since the design of the cell and gas handling system was not suitable for the control of small quantities of gas. However, Lea and Fozooni (1984), using the same crystal resonator, observed a frequency step, $\Delta f = - (6 \pm 1)$ Hz in superfluid helium at a pressure of 10 bar. Since there are no viscous losses in the superfluid, this was identified with the localisation of the second layer of helium atoms on the surface of the crystal as the pressure was increased.

The layers of helium adjacent to the adsorbed atomic layer are compressed under the van der Waals' forces of the crystal, but remain fluid though at high pressure. The density and viscosity of this helium are therefore enhanced and have values greater than ρ_f and η_f , the density and viscosity in the 'bulk' film - where its properties are

unaffected by the surface potential.

The effect of the density and viscosity of the fluid being a function of x, the distance from the crystal surface, can be deduced from the transmission line theory of Chapter 2. Assuming the helium is everywhere locally hydrodynamic, equation (2.4.8) gives

$$\frac{dZ(x)}{dx} = \frac{-Z^2(x)}{\eta(x)} - i\omega\rho(x) \qquad (4.4.1)$$

Since the range of the enhancement of the helium's properties is on an atomic scale, and therefore very much less than δ, the penetration depth of the viscous wave, the acutal impedance at x $Z(x) \simeq Z_f$, the impedance of the film. The difference between the impedance measured for a homogeneous film of thickness d and that measured for the same film but with enhanced density layers is therefore

$$\Delta Z = - i\omega \int_{x_o}^{d} \rho(x) \left[1 - \frac{\rho_f \eta_f}{\rho(x)\eta(x)}\right] dx \qquad (4.4.2)$$

where x_o is the position of the solid/liquid interface.

The change in impedance due to the enhanced density layers therefore has only an imaginary component; the resonant frequency of the crystal is decreased but its Q remains constant. If the viscosity of the helium is assumed independent of its density, equation (4.4.2) becomes

$$\Delta Z = - i\omega \int_{x_o}^{d} (\rho(x) - \rho_f)\, dx \qquad (4.4.3)$$

where the integral now gives the excess mass density and the crystal responds to it as a microbalance with a change in frequency proportional to the adsorbed mass.

The effect of the enhanced density liquid layers is therefore simply to produce a shift in the resonant frequency of the crystal which, since the range of the density enhancement is small, is essentially complete before the film grows sufficiently thick for viscous losses to become appreciable.

4.5 Results and Interpretation

As the film thickness is swept at constant temperatures, the signal S, representing the Q-factor of the crystal and the resonant frequency f are recorded; Figure 4.4 shows $\Delta f = f_o - f$ versus S for $T = 3.11$ K where f_o is the resonant frequency of the crystal in vacuum. The data is uncorrected for the shift in frequency (11 Hz) caused by the vapour pressure on the crystal (Chapter 3.2.2) and shows the large change in both S and f ($\sim$100 Hz) that occurs as the film thickness changes. In the thin film limit, the crystal is only minimally loaded and both S and f are high. As the film condenses, f initially decreases at constant S, the crystal behaving as a microbalance with frequency decreasing in proportion to the mass adsorbed, while the Q of the crystal ($\alpha S^{\frac{1}{2}}$) remains unchanged. As the film continues to thicken, viscous losses in the liquid become appreciable, decreasing both f and Q, and the locus of Δf versus S spirals around to the thick film values.

Converting S to Q and calculating X and R from the data of Figure 4.4 using equations (2.2.9) and (2.2.10) gives the Argand diagram of X versus R shown in Figure 4.5, the baseline values f_o and Q_o corresponding to $X = 0$ and $R = 0$ are discussed below.

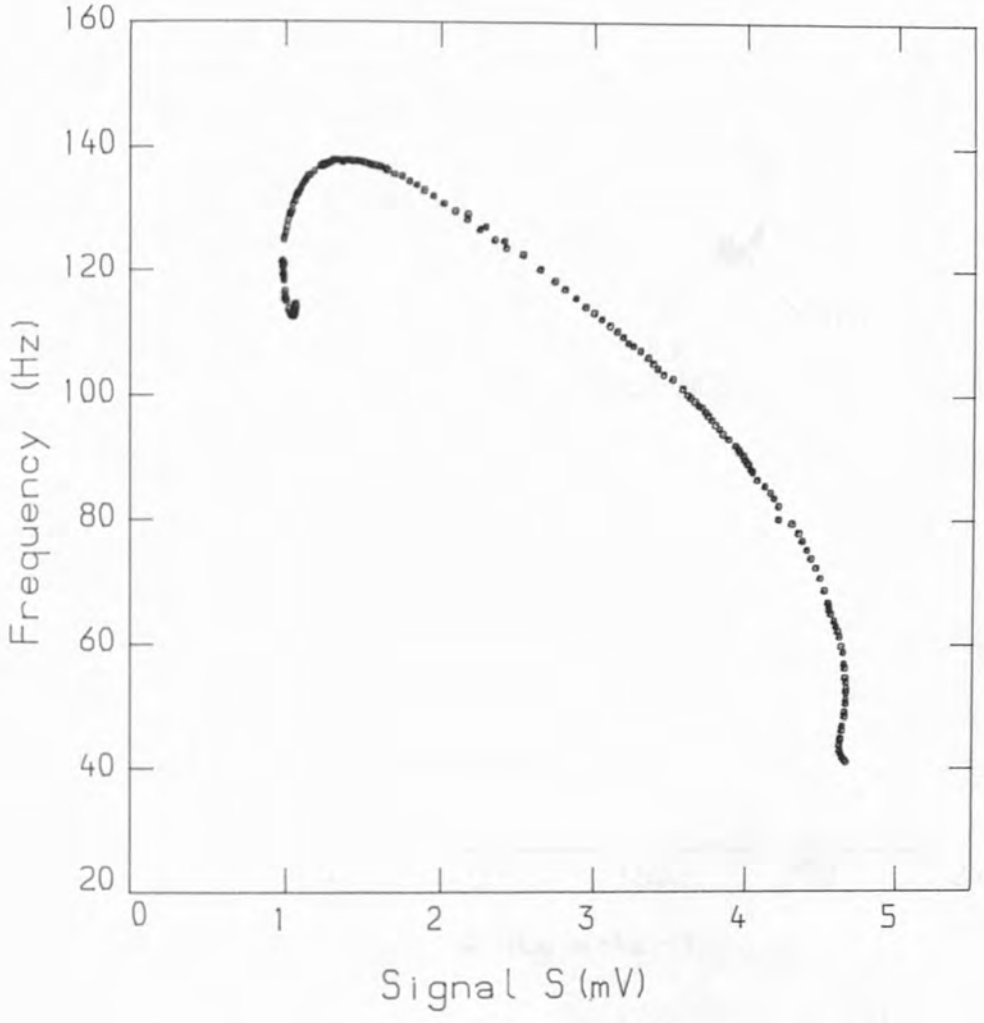

Figure 4.4

The change in resonant frequency $\Delta f = f_o - f$ of the crystal versus the signal s, representing its quality factor ($Q \alpha s^{\frac{1}{2}}$), as the thickness of a He I film is swept at 3.11 K.

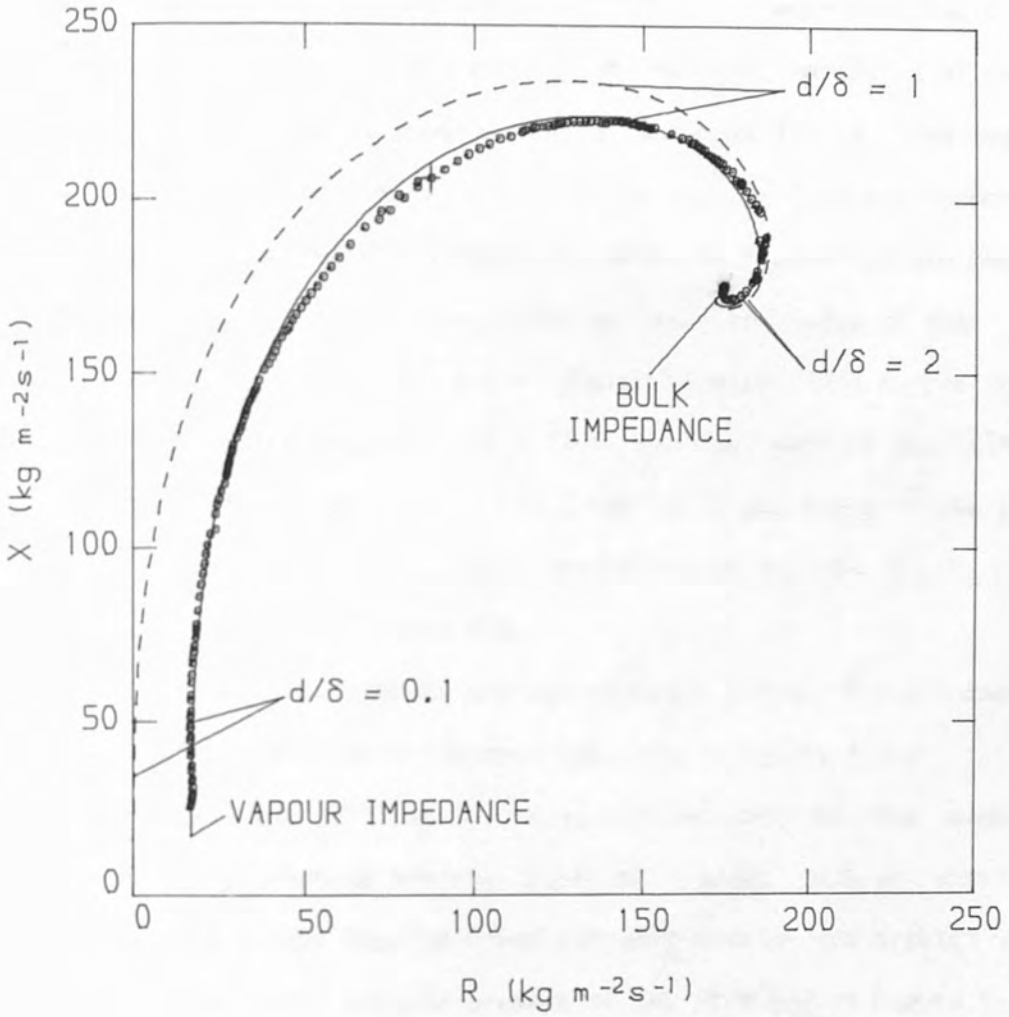

Figure 4.5

X versus R for the data of Figure 4.4, showing the locus of X versus R for a film of bulk impedance 172 $kgm^{-2}\ s^{-1}$ with a vapour impedance of zero (dashed line) and of 16 $kgm^{-2}\ s^{-1}$ (solid line). At 3.11 K , δ = 19 nm .

The film is assumed to have the properties of the bulk liquid at the same temperature and therefore for $d/\delta \gg 1$, when the liquid-vapour interface has negligible effect, the measured impedance of the film $Z_f = R_f - iX_f$ tends towards that of the bulk liquid. The impedance of bulk liquid helium $Z_b = r - ix$ at s.v.p (Lea and Fozooni, 1986 and Lea, Fozooni and Retz, 1984), is shown in Figure 4.6 and the baseline values Q_o and f_o are taken as being the value of the frequency and Q-factor at $T \lesssim 0.6$ K where the superfluid exerts no viscous forces on the crystal. At 3.11 K, the real part of the bulk liquid helium's impedance is $r = 172.3\ kgm^{-2}s^{-1}$ and since in the thick film limit $d \gg \delta$, $R_f = r$, this was used to define the $R = 0$ baseline for the data of Figure 4.5.

For a homogeneous, viscous and hydrodynamic fluid, $R = X = (\omega\rho\eta/2)^{\frac{1}{2}}$ (equation (2.3.6)) and the difference apparent in Figure 4.6 of $\Delta x = x - r = 27.7\ kgm^{-2}s^{-1}$ at 3.11 K is attributed to the mass loading of the crystal by enhanced density layers of liquid; $\Delta x = \omega\sigma$ where σ is the effective excess mass adsorbed per unit area on the crystal surface. This effect will also be present in the film and in Figure 4.5 is compensated for by setting $X_f = R_f = r$ in the thick film limit; the data therefore represents a homogeneous film with the properties of the bulk liquid throughout.

At the start of the spiral of Figure 4.5, the film is very thin $d/\delta \ll 1$ and is therefore locked to the crystal's motion with no viscous losses. The viscous wave propagated by the crystal samples predominantly the helium vapour over the film and it is therefore principally the vapours impedance Z_v which determines the starting point of the spiral. Z_v can be estimated by assuming the vapour to be hydrodynamic, at 3.11 K $\omega\tau = 0.004$, and hence taking $Z_v = (1 - i)r_v$ where $r_v = (\omega\rho_v\eta_v/2)^{\frac{1}{2}}$.

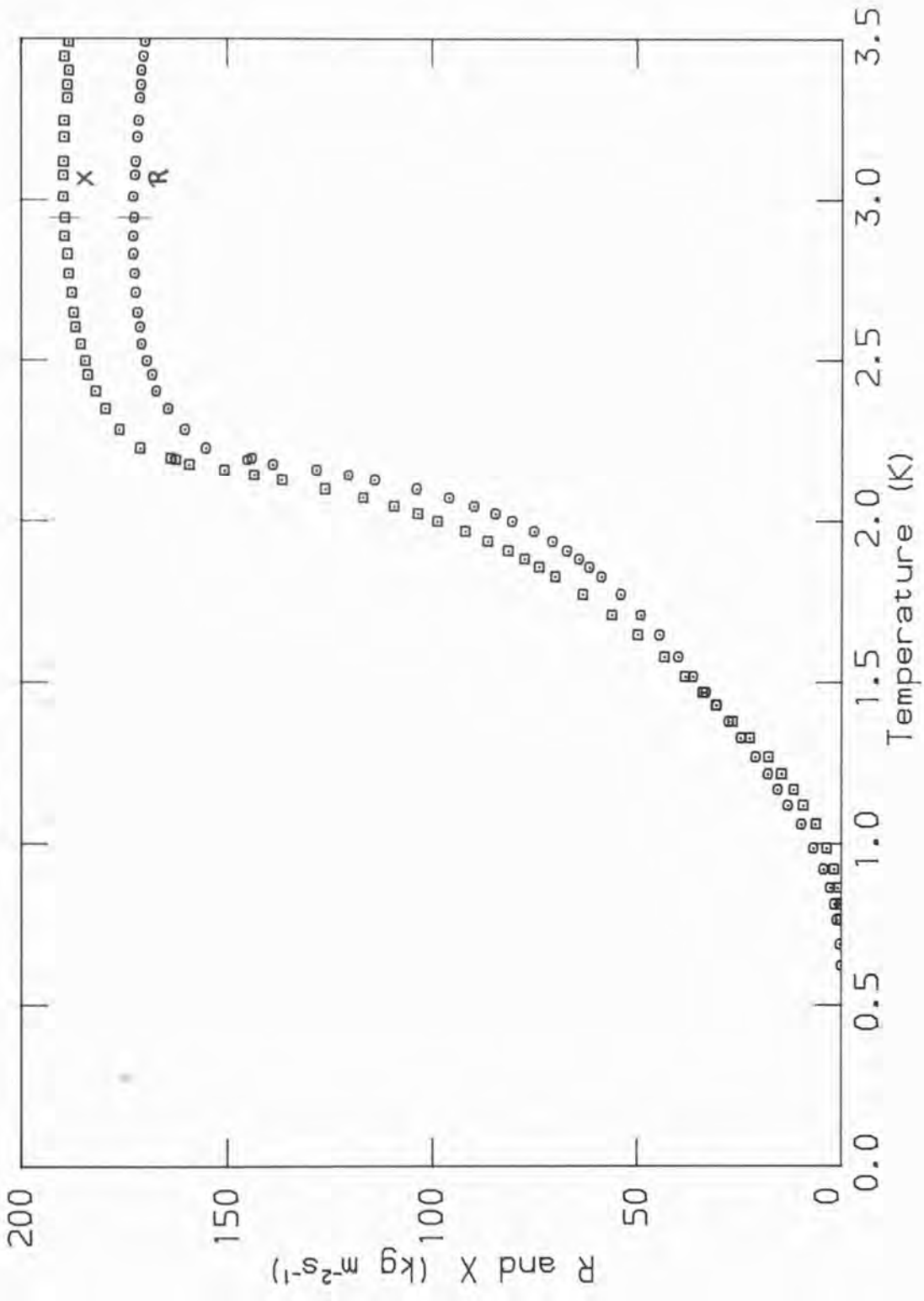

Figure 4.6

The temperature dependence of the real and imaginary parts R and X of the impedance of bulk liquid ^{4}He at 20 MHz .

The vapour's density ρ_v is found from McCarty (1973) and η_v is taken as being the zero pressure viscosity given by Betts (1976) as

$$\eta_v = \frac{8.17\ T^{\frac{1}{2}}}{\Omega(2,2)^*} \qquad \text{micropoise} \qquad (4.4.4)$$

where $\Omega(2,2)^*$ is the collision integral tabulated as a function of temperature by Monchick et al (1965). At 3.11 K, $\eta_v = 7.9\ \mu P$ and $r_v = 16\ kgm^{-2}s^{-1}$.

The locus of X versus R is calculated using transmission line theory, equation (4.3.2), and is shown in Figure 4.5 for $r = 172.3\ kgm^{-2}s^{-1}$ and for both $r_v = 0$ and $r_v = 16\ kgm^{-2}s^{-1}$, representing the film in a vacuum and in contact with helium vapour at s.v.p. respectively. At 3.11 K the penetration depth $\delta = \eta/r$ of the viscous wave in the film is 19 nm and the film thickness, although not measured directly is seen to have been swept from ~ 1.5 nm to $\gtrsim 60$ nm .

The bulk liquid impedance and the impedance of the helium vapour are both temperature dependent; r is seen in Figure 4.6 to increase above the λ-point before decreasing at higher temperatures, while r_v increases with the density and viscosity of the vapour. Figure 4.7 shows data for the sweeping of the film thickness at temperatures of 2.33 and 2.78 K, together, for the purposes of comparison, with the theory curve shown in Figure 4.5 for 3.11 K. The $R = 0$ and $X = 0$ baselines in Figure 4.7 were found in the manner described previously and r , $x - r$, η_v , r_v and δ are tabulated in Figure 4.8 for all three temperatures. The bulk liquid impedance r changes little between 2.78 and 3.11 K and these two sets of data are virtually coincident for thick films, though the increase of r_v with temperature

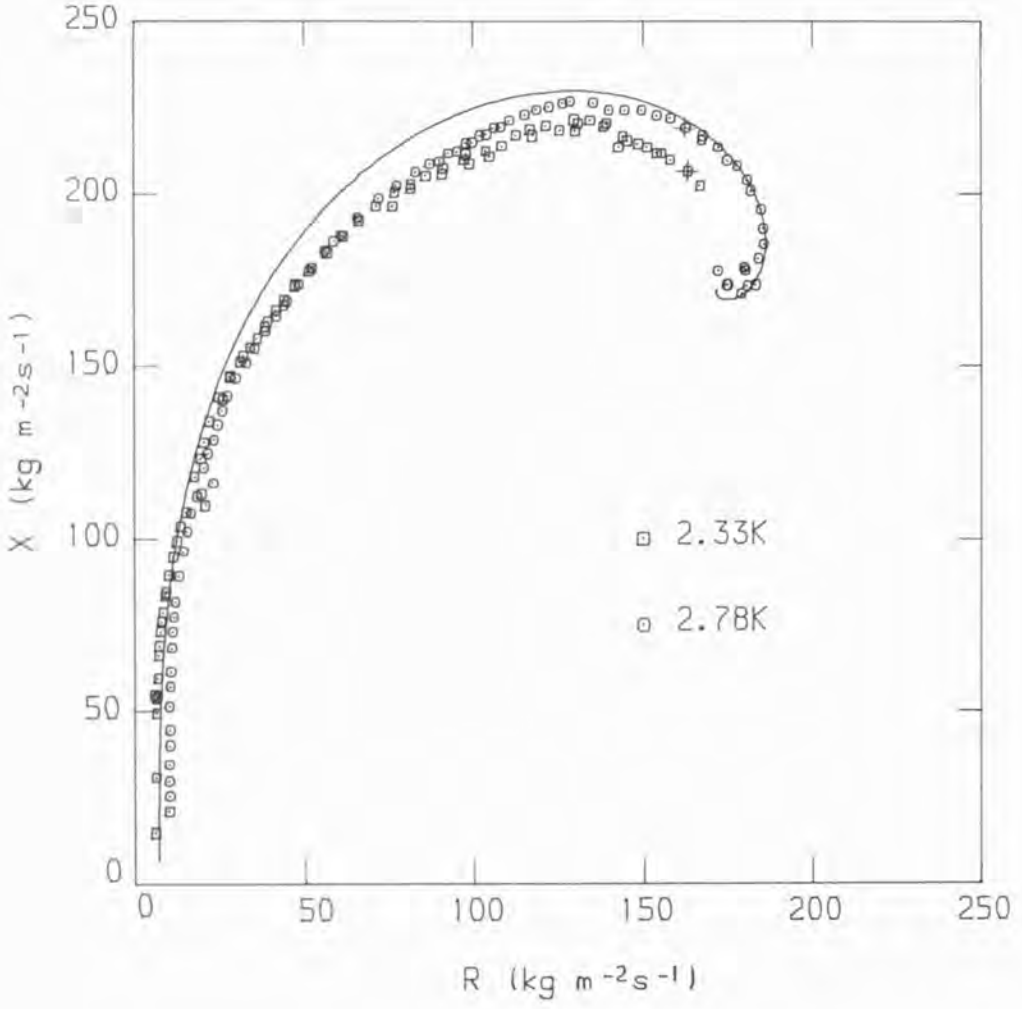

Figure 4.7

X versus R for ^{4}He films at 2.33 and 2.78 K . The solid line is the same as that drawn in Figure 4.5 and represents the data at 3.11 K .

separates the spirals in the thin film limit. The spiral at 2.33 K is incomplete due to difficulty in sweeping the film near the λ-point, though it shows the expected decrease in the bulk liquid impedance.

Chester, Yang and Stephens (1972) used a quartz crystal vibrating in shear to investigate the superfluid properties of unsaturated helium films adsorbed on the crystal electrodes. They found that as the pressure of the vapour over the film increased towards the saturated vapour pressure P_o, the change in resonant frequency Δf of the crystal increased, as would be expected if it were responding simply as a microbalance, but then as observed in Figure 4.4, Δf turned around and began to decrease. Chester et al did not offer any reasons for this behaviour but later Yang (1973) proposed an explanation, based on the viscous properties of the liquid, that is very similar to that described here. He, however, was unable to confirm it since he had no simultaneous measurements of the crystal's Q, as there are in Figure 4.4 $(Q\alpha S^{\frac{1}{2}})$, and could not determine the film's thickness from the pressure of the vapour over the film since the exact form of the crystal's surface potential was not known.

Migone et al (1985) have used an AT-cut quartz crystal vibrating in shear at a frequency of 8 MHz to investigate the formation of helium films at pressures close to the saturated vapour pressure P_o. They measured only the resonant frequency of their crystals and for some observed a frequency reversal similar to that found by Chester et al which they attributed to instabilities in the crystal's resonance mode. However, they present an analysis of the viscous losses in the film and derive a function $F(d/\delta)$ which is identical to equation (4.3.4)(b), plotted in Figure 4.2 and which has been used in this chapter to successfully explain the frequency reversal. Migone et al interpreted the

frequency measurements where no reversal occurs as evidence for the abrupt condensation of bulk helium on the crystal.

T (K)	r ($kgm^{-2}s^{-1}$)	x - r ($kgm^{-2}s^{-1}$)	δ (nm)	η_v (μP)	r_v ($kgm^{-2}s^{-1}$)
3.11	172.3	27.7	19.1	7.9	16.0
2.78	172.6	26.1	18.7	7.0	12.2
2.33	163.2	25.3	17.4	5.8	7.7
T_λ	138.9	20.9	14.8	5.3	6.3

Figure 4.8

Table giving the impedance $z = r - ix$ of bulk liquid helium, the penetration depth δ of the viscous wave in the liquid and the viscosity η_v and impedance r_v of the helium vapour at various temperatures.

Chapter 5

Helium Films $T < T_\lambda$

5.1 Introduction

At $T < T_\lambda$, the superfluid film on the crystal is in equilibrium with the liquid helium in the tube attached to the cell, and is stable with a thickness d that depends upon the height of the crystal above the liquid surface. The real and imaginary parts of the impedance of films with thickness in the range $14 < d < 23$ nm have been measured for $0.4 < T \lesssim T_\lambda$.

In the hydrodynamic region, $T \gtrsim 1.2$ K, the film is assumed to have the properties of the bulk liquid and as with the He I film of the previous chapter, its impedance will be affected by the presence of the liquid-vapour interface through the ratio d/δ, where the penetration depth $\delta = (2\eta_n/\rho_n\omega)^{\frac{1}{2}}$ is now temperature dependent (section 5.3). The film thicknesses were deduced from the data in the hydrodynamic region and have been used to estimate the van der Waals' surface potential of the crystal (section 5.5).

For $T \lesssim 1$ K, the film enters the ballistic region with $\omega\tau >> 1$ and the impedance measured depends upon the fraction of rotons α diffusely scattered from the liquid-vapour interface. The fraction α may be deduced from the data and is assumed to represent the fraction of rotons, incident upon the interface within the critical angle, which cause the evaporation of an atom from the film (section 5.4).

The data shows a large thickness and temperature dependent resonance which has tentatively been identified with vortices pinned to the crystal resonating in the $\lambda/4$ mode (section 5.6). Alternative explanations of the resonance are also considered (section 5.7).

5.2 The Superfluid Film Data

The data presented in this chapter consists principally of measurements of the real and imaginary parts of the transverse acoustic impedance at 20 MHz of six superfluid helium films. Figures 5.1-5.6 show R and X for these films, thickness 14.5, 15.5, 17.5, 19.5, 21.0 and 22.5 nm respectively, the values of d being deduced from the hydrodynamic theory of section 5.3. At T_λ, as the film warms slowly through the λ-transition, its superfluid properties are destroyed and it begins to evaporate; R and X change rapidly with temperature as the loading of the crystal decreases, providing an independent method of estimating the film thickness, as discussed below. Below T_λ, R and X decrease with temperature, the measured impedance depending on the ratio d/δ where the penetration depth $\delta = (2\eta_n/\omega\rho_n)^{\frac{1}{2}}$ and η_n and ρ_n are the viscosity and density of the normal fluid component. At the λ-point, $\delta = 14.5$ nm.

The data exhibits unexpected features in both R and X that represent an extraneous resonance coupling into the main AT-shear resonance of the crystal. The temperature of this resonance decreases with film thickness, the largest effect being at 21 nm where $\Delta R = 40\ \mathrm{kgm^{-2}\ s^{-1}}$, equivalent to 30% of R at $T = T_\lambda$.

The power dissipated in the crystal during these measurements was kept as small as possible, typically 2 nW. In general the film impedance measured was independent of crystal power dissipation, though slight power dependency was found in the region of the resonances. In particular, at $d = 21$ nm, $T \lesssim 1$ K at a frequency of 34 MHz, there was extreme power dependence of the crystal resonance, the implications of which are discussed later.

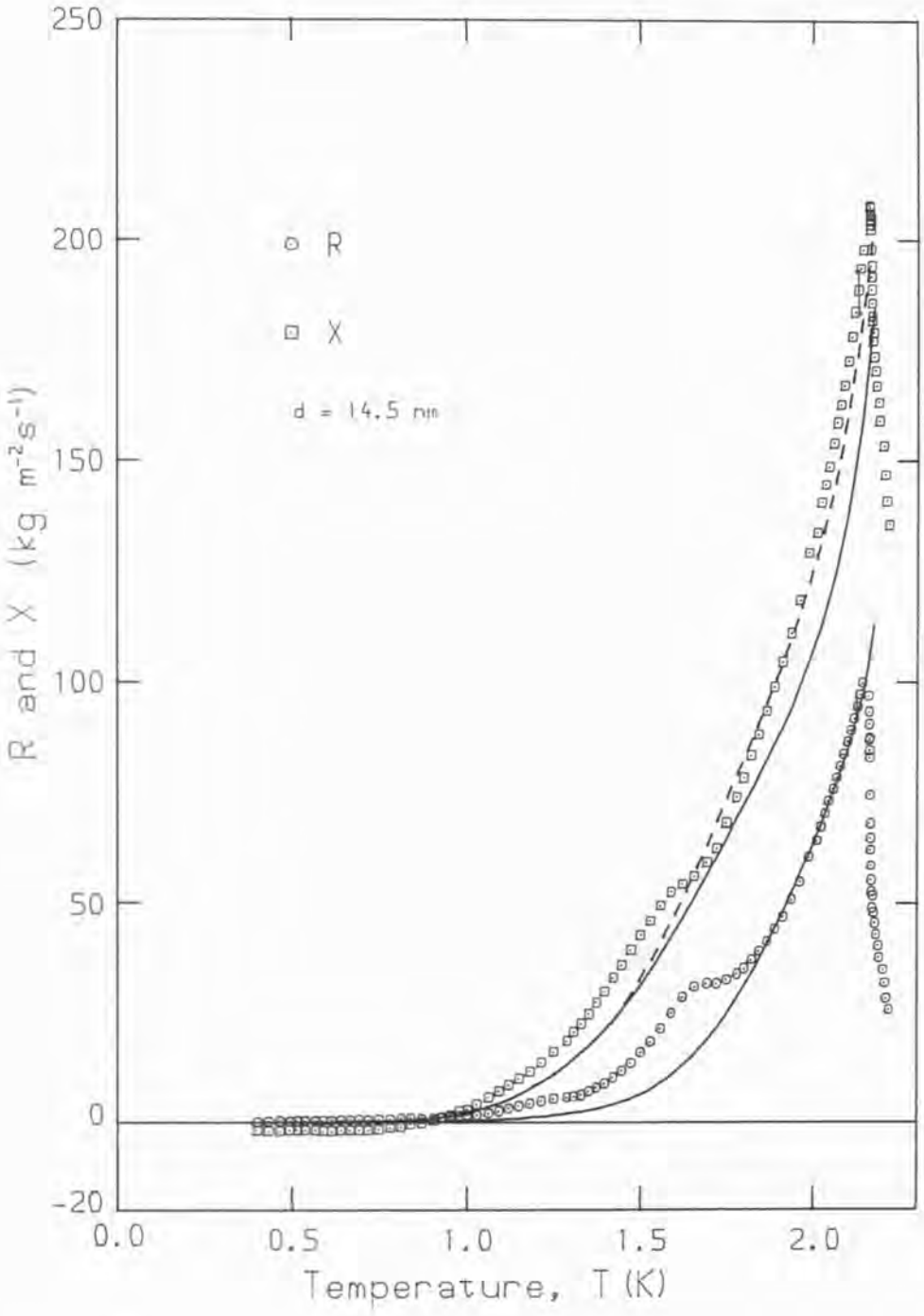

Figure 5.1

Temperature dependence of the real and imaginary parts R and X of the acoustic impedance of a film of thickness 14.5 nm . Also shown is the impedance calculated for a homogeneous film (solid lines) and that corrected for the effects of the enhancement of the density of the helium close to the crystal (dashed line).

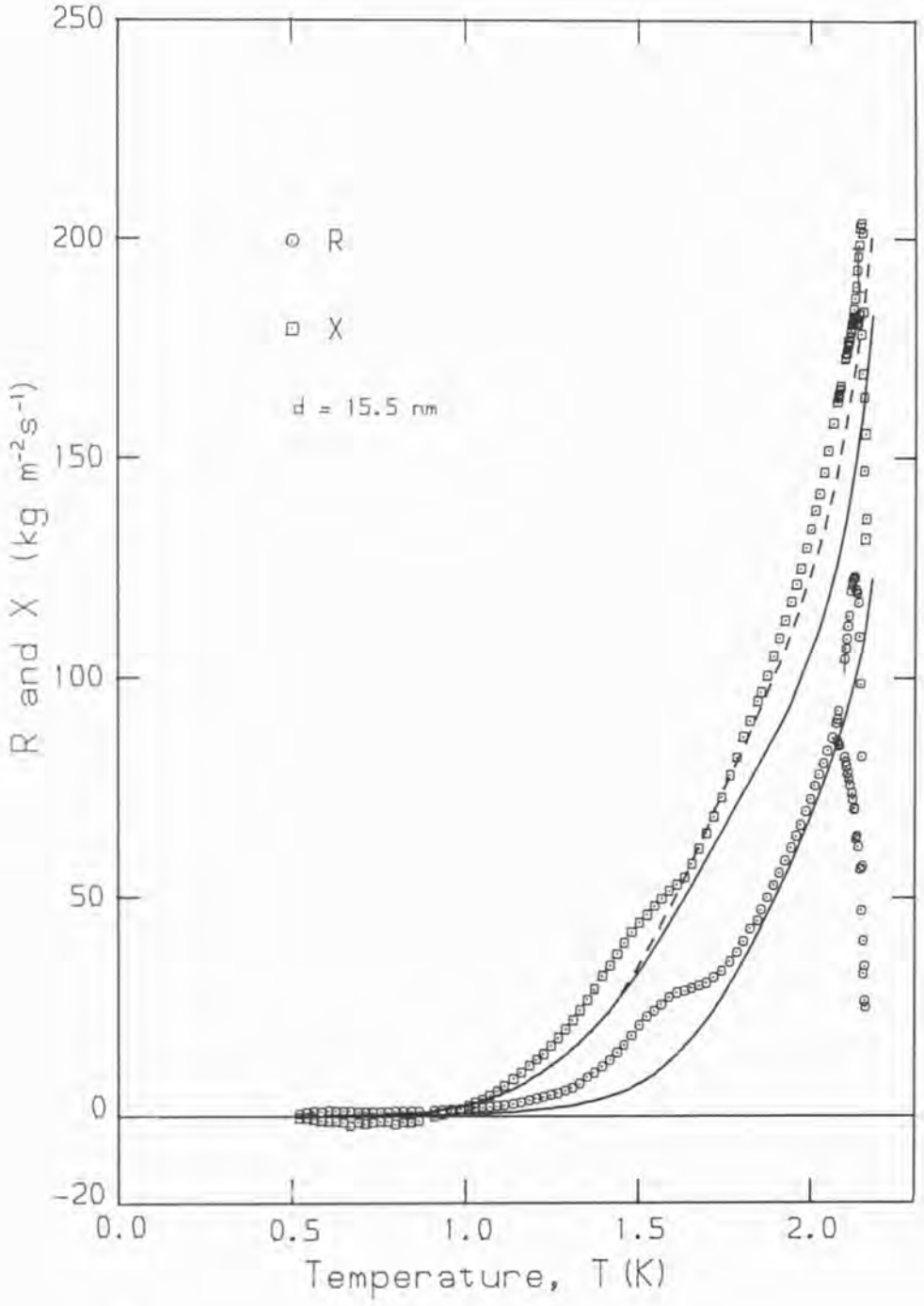

Figure 5.2

Temperature dependence of R and X of a film of thickness 15.5 nm .

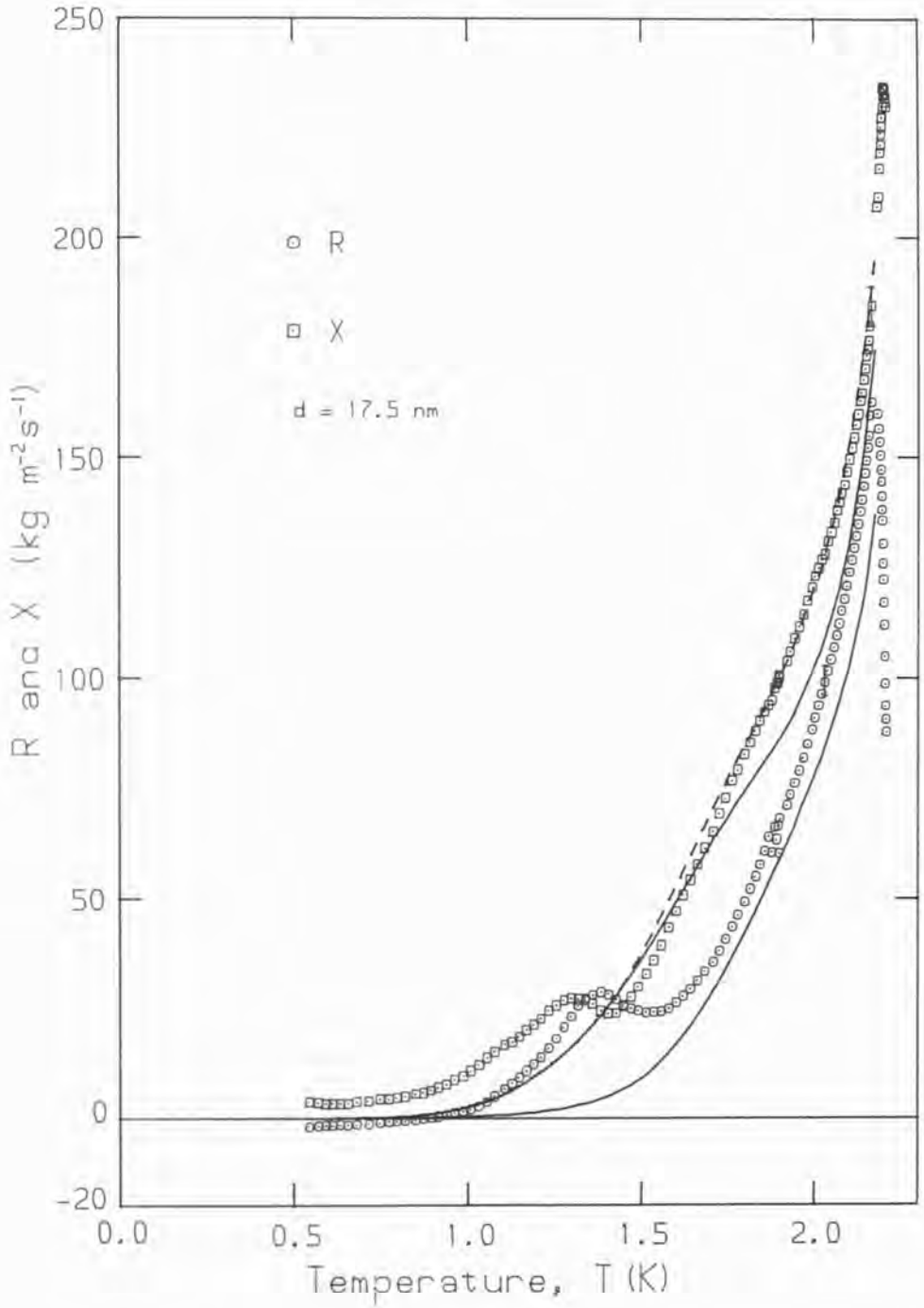

Figure 5.3

Temperature dependence of R and X of a film of thickness 17.5 nm .

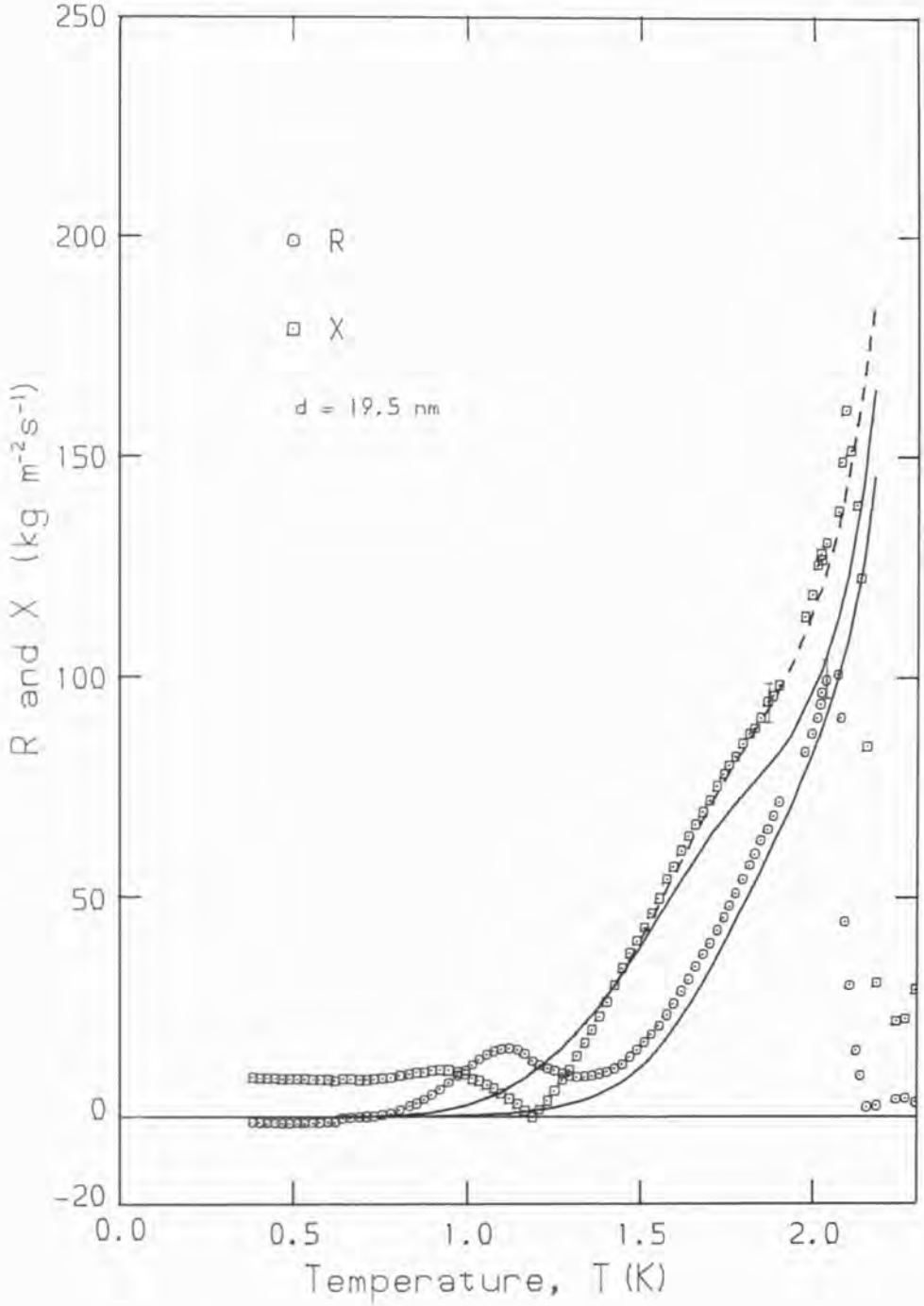

Figure 5.4

Temperature dependence of R and X of a film of thickness 19.5 nm .

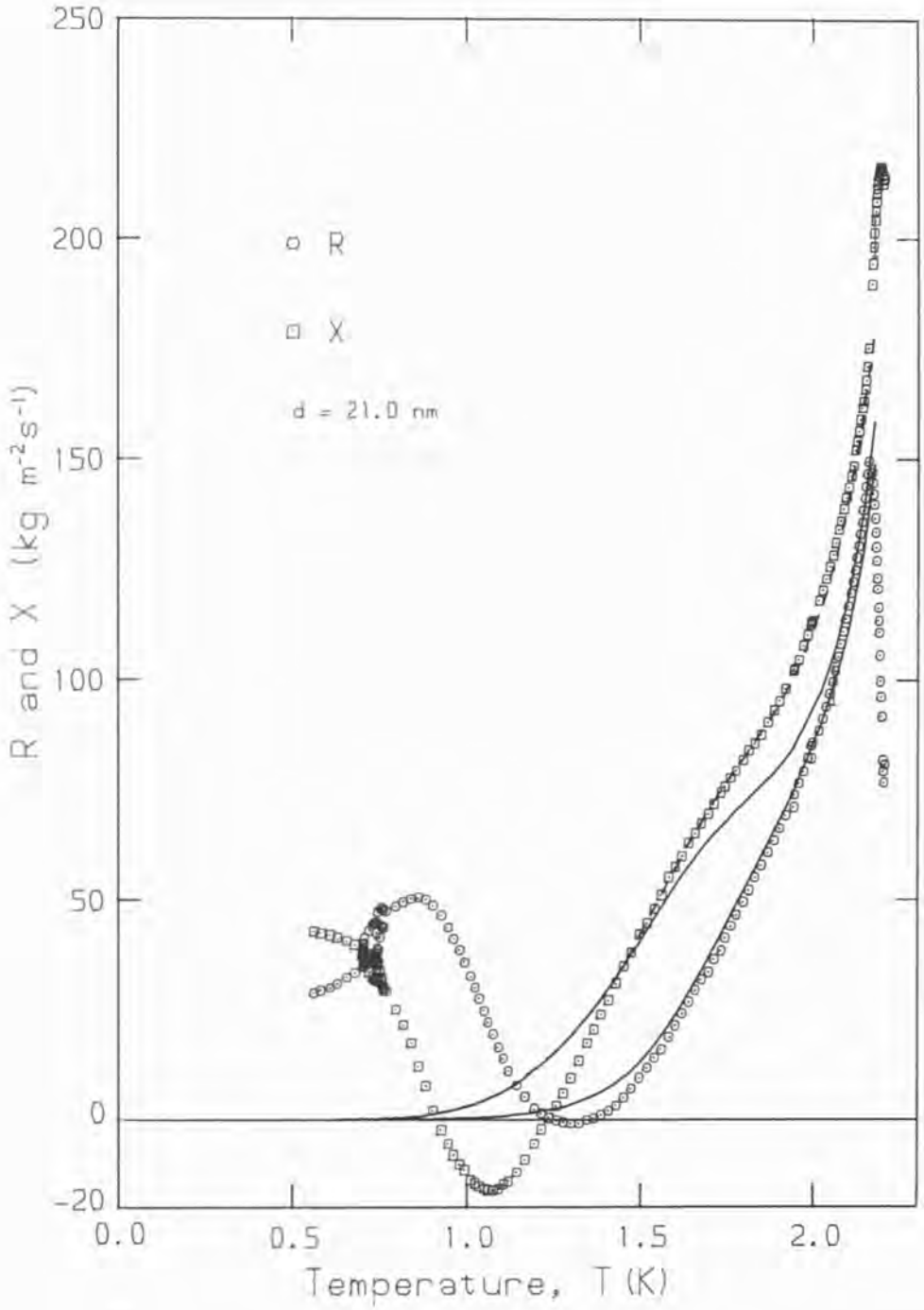

Figure 5.5

Temperature dependence of R and X of a film of thickness 21.0 nm .

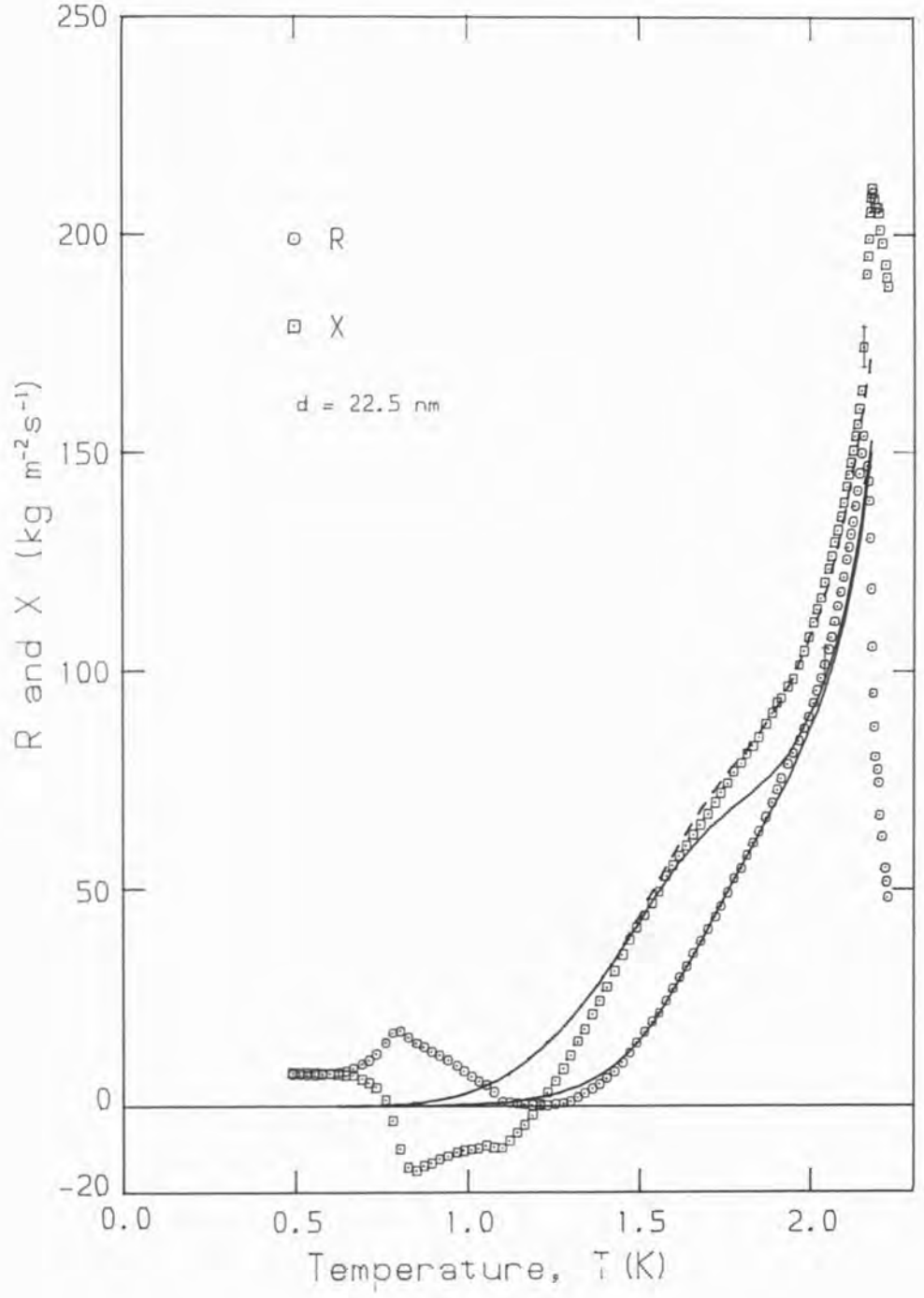

Figure 5.6

Temperature dependence of R and X of a film of thickness 22.5 nm .

$R(T)$ and $X(T)$, the real and imaginary parts of the film's impedance are found from the crystal's quality factor and resonant frequency using the equations of Chapter 2.2:

$$R(T) = \frac{n\pi R_q}{4} \left(Q^{-1}(T) - Q_o^{-1}\right) \tag{2.2.9}$$

$$X(T) = \frac{n\pi R_q}{2f_o} \left(f_o - f_s(T)\right) \tag{2.2.10}$$

where Q_o and f_o are reference or baseline values of the quality factor and resonant frequency of the crystal and correspond to $R = 0$ and $X = 0$ respectively.

Superfluid helium exerts no viscous drag or loading upon the resonator and at $T = 0$ its transverse acoustic impedance should be zero, $Z = R - iX = 0$. In practice, for bulk helium as shown in Figure 4.6, $Z = 0$ for $T < 0.6$ K and the corresponding temperature independent values of Q and f define the baselines $R = 0$ and $X = 0$. Unfortunately, as mentioned previously, it was not possible to directly obtain the bulk superfluid baselines, $Q_{o,s}$ and $f_{o,s}$ and the film data were initially referenced to the vacuum values $Q_{o,v}$ and $f_{o,v}$ and later corrected to the superfluid baselines as described below. It has been noted previously (Lea, Fozooni and Retz, 1984) that these are not the same; $Q_{o,v} > Q_{o,s}$ by approximately 20%, while $\Delta f_o = f_{o,v} - f_{o,s} = 14 \pm 3$ Hz. The vacuum values of the crystal's resonant frequency and quality factor are found after prolonged pumping on the cell at room temperature in an attempt to remove all traces of helium gas.

The difference in frequency Δf_o, between the vacuum and superfluid baselines can in part be attributed to the localisation on the

crystal electrodes of the first atomic layer of helium, giving, as discussed in Chapter 4, a microbalance frequency change of $\Delta f = 6$ Hz. The gold plating of the crystal electrodes is smooth at optical wavelengths, though with a thickness of around 500 atoms, it must be assumed rough on an atomic scale. Chester and Yang (1973) estimated a roughness of 5–15% for their gold plated crystals. Helium atoms trapped in the irregularities of the electrode surface would find themselves constrained to vibrate with the crystal, thus producing a microbalance frequency shift in excess of that produced by the first atomic layer. If this is the case, the observed excess frequency shift of ~ 8 Hz indicates that the equivalent of approximately one additional atomic layer is locked to the crystal electrodes and vibrates with them.

For the adsorption of relatively small amounts of helium onto its electrodes, the crystal should behave purely as a microbalance, its frequency decreasing in proportion to the adsorbed mass with no accompanying change in its quality factor. The observed difference between the vacuum and superfluid baselines for Q, representing an additional loss of energy from the crystal to the superfluid, must therefore be attributed to different causes, perhaps to a leakage of the crystal's vibrational energy from under the electrodes into the periphery of the crystal.

The appropriate baseline for the data presented in this chapter is that of $z = 0$ in the bulk superfluid at low temperatures, representing the effects of the bulk superfluid on the crystal. Since it was not possible to obtain $f_{o,s}$ and $Q_{o,s}$ directly, the $R = 0$ and $X = 0$ baselines were taken as being those values of R and X at $T \lesssim 0.6$ K where there is no viscous loading of the superfluid on the crystal.

For some thicknesses the resonance so affected the data as to make this impossible, in these cases the baselines were deduced from the λ-point data as follows.

As the temperature of the film is increased and it passes slowly through the λ-transition, its superfluid properties are destroyed and a temperature difference is created between the film on the crystal and the liquid in the tube, causing the film to evaporate as described in the previous chapter. Figure 5.7 shows X versus R for films of thickness 14.5 and 21 nm , X and R increase at constant d as $T \to T_\lambda$ until, at the λ-point the film ceases to be superfluid and the locus of X versus R follows that of a normal film at T_λ , with decreasing d and constant viscous penetration depth, $\delta = 14.5$ nm .

The normal film spiral plotted in Figure 5.7 assumes the liquid is homogeneous and viscous with $R = X$. The imaginary part X of the film data is therefore corrected for the enhanced density liquid close to the crystal surface by the quantity $(x - r)$, the difference between the real and imaginary parts of the bulk impedance. The spiral at T_λ is determined by the vapour impedance r_v and the bulk liquid impedance r (tabulated in Figure 4.8) and can therefore be used to define the $R = 0$ and $X = 0$ baselines for the film data. The value of d/δ at the intersection of the superfluid locus with the normal film spiral gives an estimate of d for the two films in Figure 5.7, thicknesses 14.5 and 21 nm, of (14.1 ± 0.3)nm and (22.2 ± 0.7)nm respectively.

5.3 The Hydrodynamic Region $\omega\tau << 1$

The He II film, thickness d , adsorbed on the crystal is assumed to have the properties of the bulk liquid, the measured impedance being modified by the presence of the liquid-vapour interface via the ratio

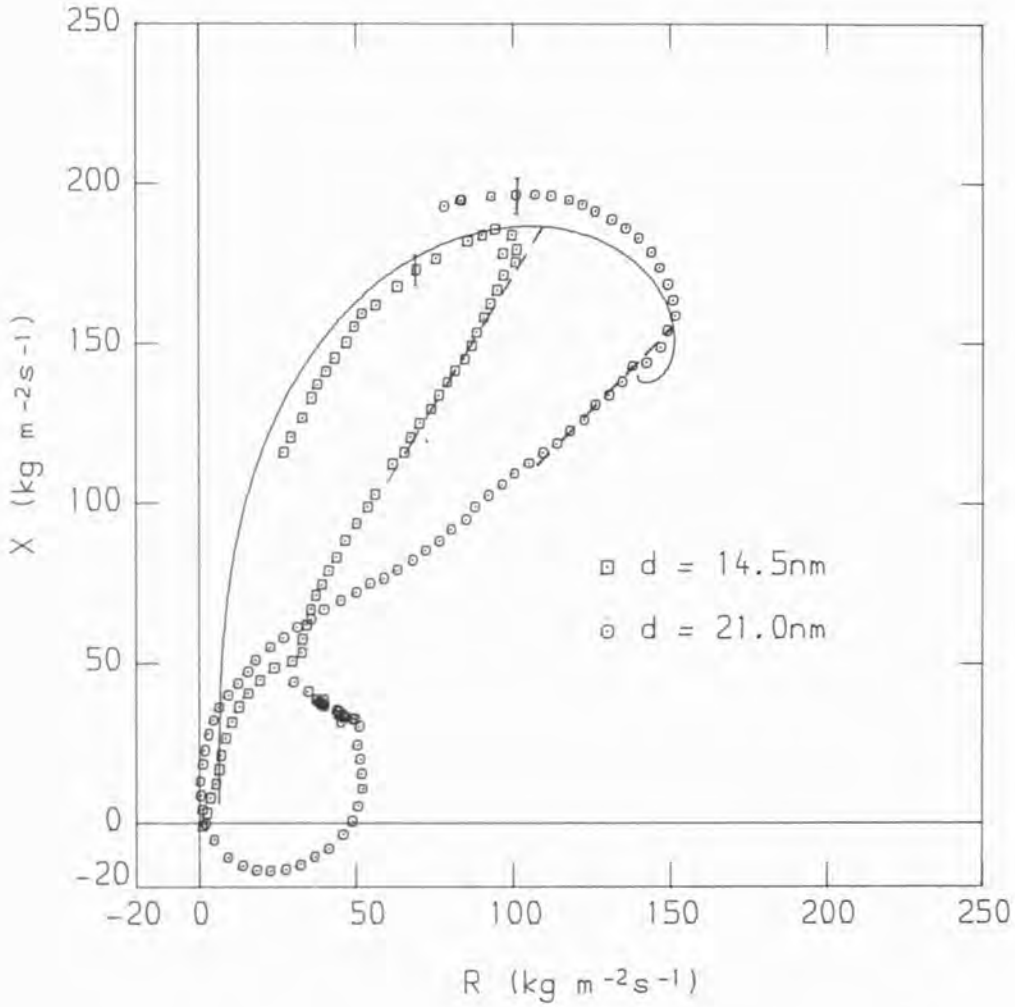

Figure 5.7

The impedance X versus R for films of thickness 14.5 and 21 nm, showing the normal liquid spiral at T_λ .

d/δ . The viscous penetration depth $\delta = (2\eta_n/\rho_n\omega)^{\frac{1}{2}}$ increases with decreasing temperature and as in Chapter 4 where the film thickness was swept at constant δ , it is appropriate to use transmission line theory to calculate the impedance of the film. From equation (2.4.7), the measured impedance $Z_f(0)$ is given by

$$Z_f(0) = R_f - iX_f$$

$$= (1 - i)r \tanh(\psi + \gamma d) \qquad (5.3.1)$$

where

$$\tanh\psi = r_v/r$$

and

$$\gamma = (1 - i)/\delta$$

r and r_v being the impedances of the bulk liquid and of the vapour in contact with the film respectively. As in section 4.3, $r_v = (\omega\rho_v\eta_v/2)^{\frac{1}{2}}$ is calculated assuming the vapour to be hydrodynamic, $\omega\tau < 1$, η_v being the zero pressure viscosity of the gas. This assumption is valid for $T > 1$ K ; for temperatures below this ρ_v is very small and the effect of the viscous loading of the vapour on the measured impedance is negligible.

The real and imaginary parts of the bulk liquid impedance at 20 MHz, $z = r - ix$ are plotted as functions of temperature in Figure 4.6. The behaviour of r at frequency f is interpreted in terms of the viscosity,

from equation (2.3.6)

$$\eta = \frac{r^2}{\pi f \rho_n} \qquad (5.3.2)$$

where ρ_n is the normal fluid density. The viscosity at 20 MHz thus calculated (Lea, Fozooni and Retz, 1984) exhibits a sharp decrease below the λ-point, levelling out at a value of 12.5 μP between 1.2 and 1.5 K before decreasing rapidly to zero.

The hydrodynamic viscosity for $T < 1.8$ K has been given by Khalatnikov (1976) as the sum of the roton viscosity η_r and the phonon viscosity η_p

$$\eta = \eta_r + \eta_p$$

At $T > 1.4$ K the behaviour of the hydrodynamic viscosity and that at 20 MHz is similar, both phonons and rotons are in the hydrodynamic region but the phonon viscosity η_p is small and the measured viscosity is therefore essentially that of the rotons, η_r .

Below 1.3 K the hydrodynamic viscosity increases exponentially, due to the rapid rise in η_p as phonon-roton scattering decreases. At 20 MHz the phonons are in the non-hydrodynamic region with $\omega\tau_p > 1$ and $\ell_p/\delta > 1$ where τ_p and ℓ_p are the relaxation time and mean free path of the phonons. In the ballistic limit $\omega\tau_p >> 1$, the impedance of the phonons is found from equation (2.3.9)

$$R_{\infty,p} = \tfrac{1}{4}\, \alpha_p \rho_p u_1$$

$$= 1.06\, \alpha_p\, T^4 \qquad \text{kgm}^{-2}\ \text{s}^{-1}$$

where ρ_p is the phonon density, α_p the fraction of excitations diffusely scattered at the crystal surface and u_1 is the velocity of first-sound. $R_{\infty,p}$ therefore decreases to zero as T^4 and the rapid rise in the hydrodynamic viscosity (seen at low temperatures) is not observed at 20 MHz. Below 1.2 K the effective roton viscosity also decreases rapidly to zero as the rotons enter the non-hydrodynamic region, and in the limit of $\omega\tau_r >> 1$ and $\ell_r/\delta >> 1$ where $\ell_r = \bar{v}_r \tau_r$ is the roton mean free path, R is given by

$$R_{\infty,r} = \tfrac{1}{4} \alpha_r \rho_r \bar{v}_r$$

$$= 1.2 \times 10^5 \, \alpha_r e^{-\Delta/K_b T} \qquad \text{kg m}^{-2} \text{ s}^{-1}$$

where the mean velocity of the rotons has been taken as $\bar{v}_r = (2K_b T/\pi\mu)^{\frac{1}{2}}$, μ being their effective mass.

R_f and X_f, the real and imaginary parts of the film's impedance calculated from equation (5.3.1) are plotted in Figures 5.1-5.6. $R_f(T)$ is in general in good agreement with the data for the hydrodynamic region at $T > 1.2$ K. $X_f(T)$ exhibits an inflection, the temperature and magnitude of which is film thickness dependent and which is not apparent in the data. The inflection occurs at that value of δ that gives $d/\delta \sim 1$ and corresponds to the top of the film spiral in Figure 4.5 where X remains approximately constant as the ratio d/δ is swept.

The analysis leading to equation (5.3.1) for Z_f assumes that the helium film adsorbed on the crystal is homogeneous and has the properties of the bulk liquid through-out, $Z(x) = (1 - i)r$ for $0 < x < d$ where $r = (\omega\rho_n\eta_n/2)^{\frac{1}{2}}$. The presence of the crystal surface,

however, leads to inhomogeneities in the liquid as in the He I film of Chapter 4. Firstly, the pressure in the layers of helium close to the crystal is increased above the bulk value by van der Waals' forces, and secondly, the superfluid density at an immersed surface must go to zero.

The van der Waals' forces between a plane substrate and an adsorbed film are discussed in general in Chapter 2.5 and with specific reference to the quartz crystal in section 5.5. Briefly, the van der Waals' forces between the crystal and the helium produce an attractive potential of the form

$$V(y) = \frac{-AK_b}{y^n}$$

where n increases from $n = 3$ to $n = 4$ as y, the distance from the crystal increases. The pressure and normal fluid density of the liquid close to the surface are therefore enhanced above the bulk values, and the local impedance of the fluid increases as the crystal is approached. For $T > 1.8$ K the pressure dependence of the λ-line means that the high density helium near the crystal may be in the normal state.

The superfluid fraction decreases to zero at an immersed solid surface in accordance with the boundary condition for the superfluid order parameter at a plane wall, $\rho_s(y = 0) = 0$. The distance over which the superfluid density rises from zero at $y = 0$ to the bulk value $\rho_s(\infty) = \rho - \rho_n(\infty)$ is characterised by the superfluid healing length, $a(T)$ which is small for $T < 2$ K, but diverges as $T \to T_\lambda$. Thus excess layers of normal liquid are present adjacent to the crystal surface, their thickness being temperature dependent.

The range of these surface induced inhomogeneities is small and, except near the λ-point, much less than the penetration depth of the viscous wave, therefore, as discussed in Chapter 4, their effect on the impedance measured by the crystal is simply that of mass loading. X is thus increased in direct proportion to the equivalent mass of the enhanced density helium layers while R remains unchanged.

The mass loading due to the density enhancement of the layers of helium close to the crystal is the same in both the bulk liquid and the film, and in the hydrodynamic region $T \gtrsim 1.2$ K is given by $\Delta\sigma = \Delta x_b/\omega$ where $\Delta x_b = x - r$ is the difference between the imaginary and real parts of the bulk liquid impedance. The impedance of the film is therefore $X_f + \Delta x_b$ where X_f, from equation (5.3.1) is the impedance of the homogeneous film. $X_f + \Delta x_b$ is plotted in Figures 5.1-5.6 for the appropriate film thickness and is a relatively good fit to the data.

The thickness of the films of Figures 5.1-5.6 was estimated (±1 nm) from the fit of the data in the hydrodynamic region to equation (5.3.1), with X_f corrected for the effect of the enhanced density layers as described above, and d together with h, the height of the crystal above the bulk helium liquid level, is tabulated in Figure 5.16.

5.4 The Ballistic Region $\omega\tau >> 1$

Bulk liquid helium enters the non-hydrodynamic region $\omega\tau > 1$ when the mean free path ℓ of the excitations becomes comparable with or greater than the penetration depth δ, $\omega\tau\alpha(\ell/\delta)^2$. A similar effect occurs in the film adsorbed on the crystal when, as temperature decreases, ℓ becomes comparable with the film thickness d.

For the thicker films, the low temperature data is distorted by the resonance and so analysis is restricted to the films of thickness 14.5 and 15.5 nm, the real part of the impedance being plotted in Figure 5.8 and the imaginary part in Figure 5.9.

In the non-hydrodynamic limit, $\omega\tau >> 1$, it is possible to find the impedance of the film measured by the crystal using a similar argument to that used in Chapter 2 to calculate the ballistic impedance of the bulk liquid. The excitations in the He II film in the limit $\omega\tau >> 1$, $\ell/\delta >> 1$ are scattered at the crystal and travel unimpeded across the film to be reflected at the liquid-vapour interface. On returning to the crystal, their contribution to the measured impedance will depend upon whether they were specularly reflected or diffusely scattered at the film surface. The impedance is defined as $Z = \pi/u$ where $u = u_o e^{-i\omega t}$ is the velocity of the crystal surface and the shear stress or flux of transverse momentum on the crystal for a film of thickness d is

$$\pi = n_s m(u_1 - u_2)$$

where $u_2 = s_2[\alpha_1 u_o e^{-i\omega(t - T)} + s_1 u_2]$ is the velocity of the excitations as they approach the crystal and $u_1 = \alpha_1 u_o e^{-i\omega t} + s_1 u_2$ is their velocity after reflection. Thus

$$\pi = n_s mu\alpha_1 \left(1 - \frac{\alpha_1 s_2 e^{i\omega T}}{1 - s_1 s_2}\right) \qquad (5.4.1)$$

where as previously, $\alpha_1 = 1 - s_1$ is the fraction of excitations diffusely scattered from the crystal, s_2 is the fraction specularly reflected at the liquid-vapour interface and $T = 2d/\bar{c}\cos\theta$ represents

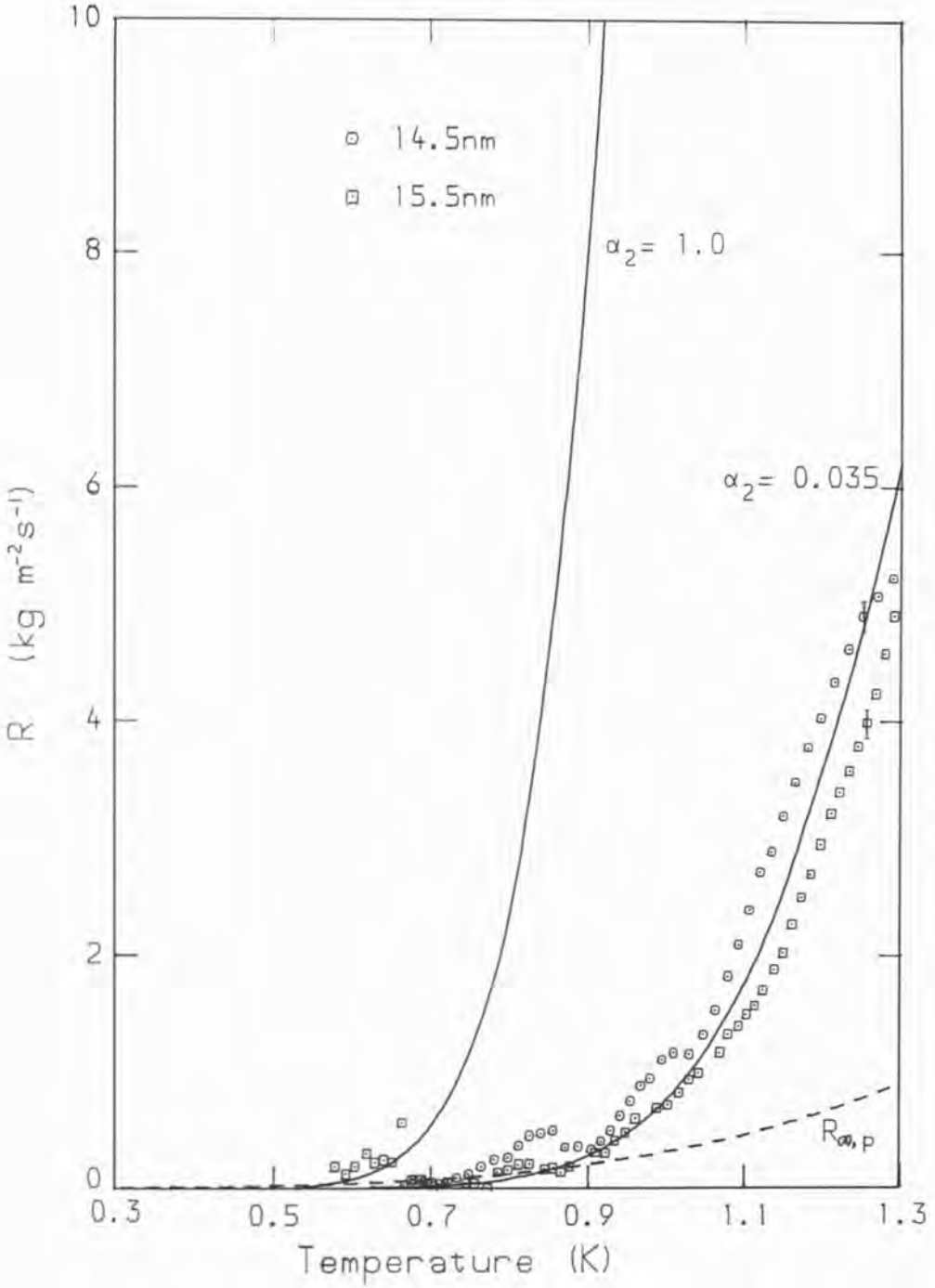

Figure 5.8

The real part R of the impedance of films of thickness 14.5 and 15.5 nm at low temperature. Also shown is the ballistic impedance calculated for rotons (solid lines) and phonons (dashed line).

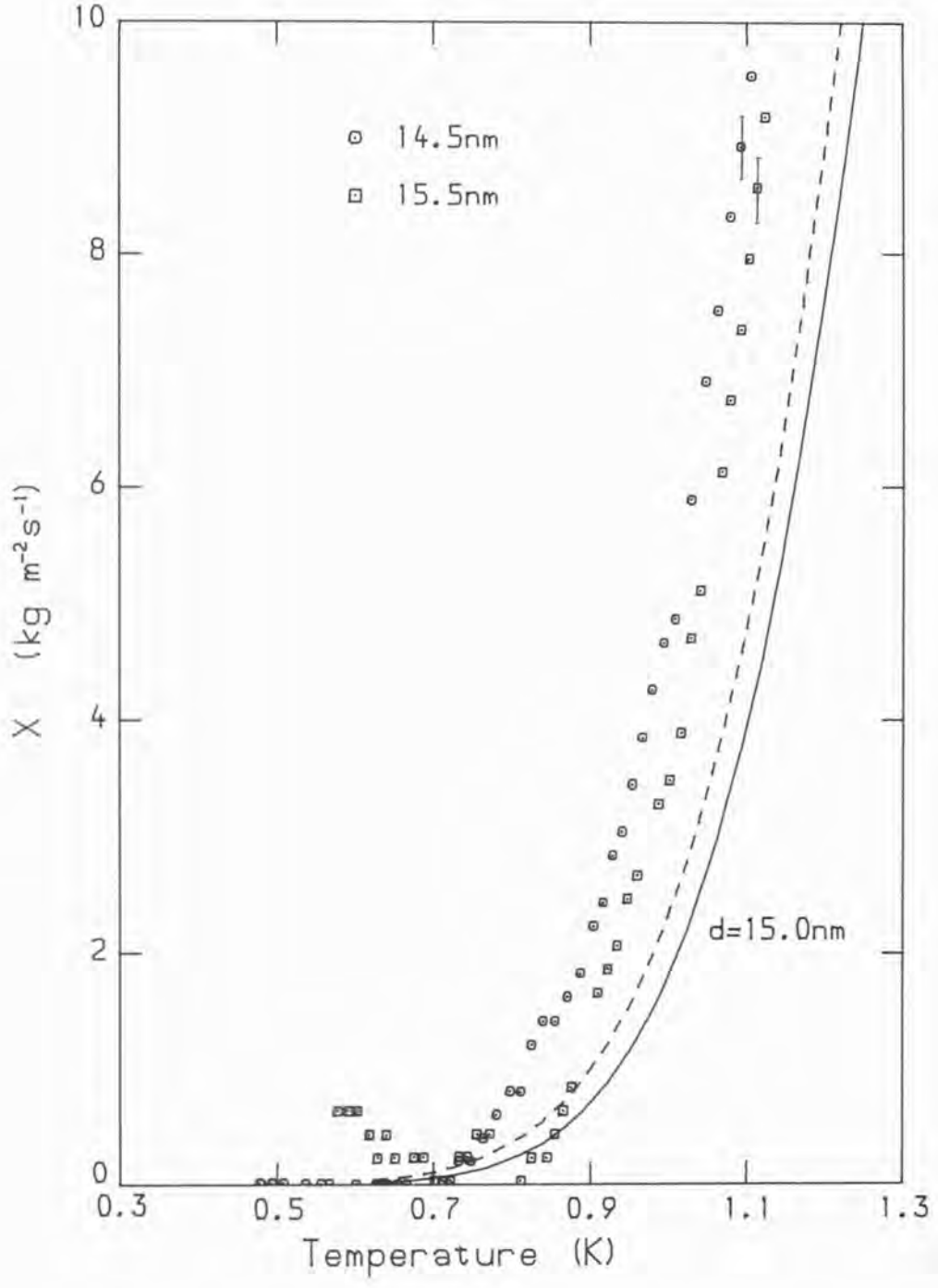

Figure 5.9

The imaginary part X of the impedance of the 14.5 and 15.5 nm films, showing the roton ballistic impedance for a 15 nm film (solid line) and including the effects of two-dimensional rotons (dashed line).

the time between the excitation's interactions with the crystal. n_s is given by equation (2.3.7)

$$n_s = \frac{n\bar{c}}{2} [\sin^2\theta]_0^{\pi/2} \qquad (5.4.2)$$

and hence the ballistic impedance of the film is

$$Z_\infty = \tfrac{1}{4} \frac{\alpha_1\alpha_2}{1 - s_1s_2} \rho\bar{c} - i \frac{\alpha_1^2 s_2}{1 - s_1s_2} \omega\rho d \qquad (5.4.3)$$

where ρ is the density of the excitations and $\bar{c}$ is their mean velocity. Z_∞ for a film therefore has both real and imaginary parts, in contrast to the bulk ballistic impedance which is purely real (equation (2.3.10)). R_∞ is independent of film thickness and X_∞ is proportional both to thickness and to frequency ω.

Lea, Fozooni and Retz (1984) give a value for the diffusive scattering coefficient of phonons from the surface of the crystal of $\alpha_1 < 0.3$ and $R_{\infty,p}$, the real part of the ballistic impedance for phonons is plotted in Figure 5.8 for $\alpha_1 = 0.3$ and $\alpha_2 = 1$. In reality α_2, the fraction of phonons diffusely scattered from the liquid-vapour interface, will be less than unity and the contribution of the phonons to the impedance in the non-hydrodynamic region will be very small.

Assuming therefore that it is only the rotons that contribute significantly to the impedance in the ballistic region, the data of Figure 5.8 shows that for $\alpha_1 = 1.0$ (Lea, Fozooni and Retz, 1984) α_2, the fraction of rotons diffusely scattered from the liquid-vapour interface is approximately 0.035. Following the analysis of Wyatt (1984),

the fraction α_2 of rotons are considered to cause the evaporation of an atom from the surface of the film, equilibrium being maintained by atoms of the vapour above the liquid condensing and creating excitations in the reverse process. A roton incident on the film surface and evaporating an atom must satisfy the energy conservation relation

$$\varepsilon(p) = E_b + \frac{\hbar^2 k^2}{2m} \tag{5.4.4}$$

where $\varepsilon(p) = \Delta + (p - p_o)^2/2\mu$ is the energy of the roton, $E_b = 7.16$ K is the binding energy of the atom in the liquid and $\hbar k$ is the momentum of the free atom, mass m. Conservation of momentum parallel to the liquid surface gives the condition

$$q \sin\theta = k \sin\phi \tag{5.4.5}$$

where $q = p/\hbar$ and k are the wave vectors of the roton and free atom respectively and θ and ϕ are the angles between their paths and the normal to the surface. For a roton of momentum p and energy $\varepsilon(p)$, θ will thus have a maximum allowable value, the critical angle θ_c, corresponding to the evaporation of an atom with wave vector parallel to the surface

$$\theta_c = \sin^{-1}(k/q) \tag{5.4.6}$$

which is dependent on the energy of the roton through the wave vector q. A roton approaching the surface with an incident angle greater than this value will be specularly reflected. For $p = p_o$, $\theta_c = 15°$.

The fraction of rotons incident upon the liquid-vapour interface within the critical angle θ_c can be estimated as follows. From equation (5.4.2) the number of rotons of energy $\varepsilon(p)$ and velocity V_g striking the film surface with an angle $\theta < \theta_c$ is given by

$$\frac{n(\varepsilon)}{2} V_g \sin^2\theta_c \tag{5.4.7}$$

where V_g is the group velocity of the rotons, $V_g = \partial\varepsilon/\partial p$ and $n(\varepsilon)$ is taken as having the Boltzmann form $\exp[-\varepsilon(p)/K_bT]$. Hence β, the fraction of rotons incident on the surface within the angle θ_c is, from equations (5.4.4), (5.4.6) and (5.4.7),

$$\beta = \frac{\int_{-\infty}^{\infty} \exp\left[-\frac{\varepsilon(p)}{K_bT}\right] \cdot \frac{|p - p_o|}{\mu} \cdot \frac{2m}{p^2}\left[\varepsilon(p) - E_b\right] \cdot \frac{p^2}{2\pi^2\hbar^3}\, dp}{\int_{-\infty}^{\infty} \exp\left[-\frac{\varepsilon(p)}{K_bT}\right] \cdot \frac{|p - p_o|}{\mu} \cdot \frac{p^2}{2\pi^2\hbar^3}\, dp} \tag{5.4.8}$$

Substituting $x = |p - p_o|/2\mu K_bT$ and noting that $p^2 \simeq p_o^2$, this becomes

$$\beta = \frac{2m}{p_o^2} \frac{\int_0^{\infty} xe^{-x^2}(\Delta - E_b + K_bT\, x^2)dx}{\int_0^{\infty} xe^{-x^2}\, dx} \tag{5.4.9}$$

where the integrals are now in standard form and are evaluated to give

$$\beta = \frac{2m}{p_o^2}(\Delta - E_b + K_bT) \tag{5.4.10}$$

$$= 0.0452\ (1.49 + T)$$

Thus β , being the fraction of rotons incident upon the interface within the critical angle is temperature dependent, rising from 0.090 at 0.5 K to 0.112 at 1 K . If $\beta = 0.1$ is taken as being a representative value over this temperature interval then, since from Figure 5.8 the fraction of rotons evaporating an atom is $\alpha_2 = 0.035$, the probability of the evaporation of an atom from the surface of the film by a roton within the critical angle is approximately 0.35 . This compares very favourably with the value of $\frac{1}{3}$ given by Wyatt (1984) from consideration of the dynamic equilibrium of helium liquid at $T < 2$ K with its saturated vapour for the evaporation of an atom by an excitation.

In bulk ^{4}He, the ballistic impedance has no imaginary component. In the film however, the possibility of excitations being specularly reflected from the liquid-vapour interface introduces a thickness dependent contribution to the imaginary part of the impedance, equation (5.4.3)

$$X_b = \frac{\alpha_1^2 s_2}{1 - s_1 s_2} \omega \rho_n d \qquad \text{for} \quad \omega\tau >> 1 \tag{5.4.11}$$

The contribution of phonons to X_b is very small, taking $\alpha_1 = 0.3$ as before for the fraction of phonons diffusely scattered from the crystal and assuming total specular reflection from the film surface, $s_2 = 1$, then for $d = 15$ nm ,

$$X_{b,p} = 0.004\ T^4$$

which is negligible in comparison with the measured impedance in Figure 5.9. The roton contribution to the imaginary part of the ballistic impedance, $X_{b,r}$ is plotted in Figure 5.9 for $d = 15$ nm ,

$\alpha_1 = 1 - s_1 = 1$ and $s_2 = 1$ and is a substantial contribution to the measured impedance X. The excess impedance $\Delta X = X - X_{b,r}$ can, as previously, be defined in terms of an effective excess mass per unit area associated with the surface of the crystal

$$\Delta\sigma = \frac{\Delta X}{\omega} \tag{5.4.12}$$

Other experiments have also measured an excess normal fluid density near a solid surface, such as those of Bishop et al (1981) using 4th sound, and the heat capacity measurements of Brewer et al (1965). The enhancement of the normal fluid density due to van der Waals' forces is considered to be insufficient to account for the size of effect observed and it has been suggested (Chester et al, 1980; Bondarev, 1982) that the excess normal fluid density can be associated with rotons localised at the solid/liquid helium interface.

Neutron-scattering (Thomlinson, Tarvin and Passell, 1980) has shown these two-dimensional rotons to have an energy gap, $\Delta \sim 5.85$ K, substantially less than the bulk roton gap ($\Delta \sim 8.67$ K) at SVP, but consistent with the bulk gap at pressures comparable with those in the enhanced density layers close to the substrate. The two-dimensional rotons appear to be confined to within three atomic layers of the substrate and their contribution to the excess normal fluid surface density has been estimated by Bondarev (1982),

$$\Delta\sigma = \frac{\mu_1^{\frac{1}{2}}(p_o')^3}{2(2\pi)^{\frac{1}{2}}(K_b T)^{\frac{1}{2}}h^2}\, e^{-\Delta'/K_b T} \tag{5.4.13}$$

where $\Delta' = 5.85$ K and $\mu_1^{\frac{1}{2}}(p_o')^3 = 1.1\,\mu^{\frac{1}{2}}p_o^3$, μ and p_o having their bulk values.

Thus from equations (5.4.12) and (5.4.13) the excess impedance due to two-dimensional rotons can be found and the total impedance is plotted in Figure 5.9. The discrepancy still apparent between the data and the impedance thus calculated may be due to the comparatively large uncertainty in the position of the baseline, $X = 0$, due to the effects of the resonance discussed in section 5.6.

5.5 The Surface Potential of the Crystal

As discussed in section 5.3, the fit of the hydrodynamic theory, equation (5.3.1), to the data of Figures 5.1-5.6 provides an estimate (± 1 nm) of the thickness of the films adsorbed on the crystal. It is therefore possible to investigate the form of the van der Waals forces between the gold plated quartz crystal and the helium film. The potential of a helium atom, mass m, at the surface of a saturated film, thickness d, adsorbed on the crystal has the form (Chapter 2.5)

$$V(d) = -mgh = \frac{-AK_b}{d^n} \qquad (5.5.1)$$

where n increases from 3 to 4 as d increases and retardation effects become important, and A is a constant of proportionality that is substrate dependent. The height h of the crystal above the liquid helium surface is found from the amount of gas at room temperature and known pressure that is condensed into the tube attached to the experimental cell, and is tabulated along with d in Figure 5.16.

The log-log plot of h versus d is shown in Figure 5.10, the gradient of the line drawn through the data points is 4.0 ± 0.4. At

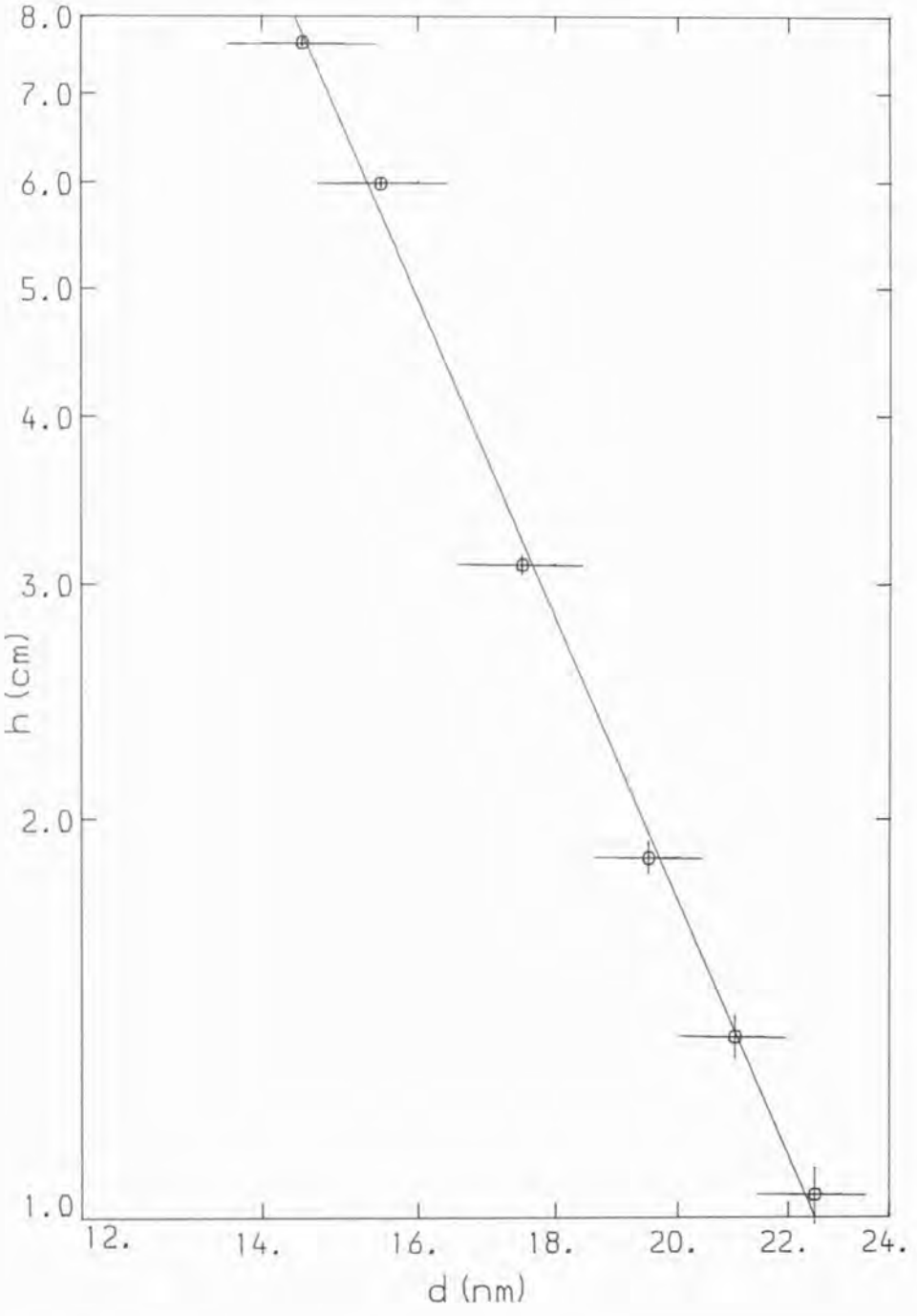

Figure 5.10

The height h of the crystal above the surface of bulk liquid helium versus the film thickness.

these film thicknesses, the exponent n of equation (5.5.1) should be approaching $n = 4$; the data of Sabisky and Anderson (1973) for a helium film adsorbed on a SrF_2 cleaved crystal substrate shows n is approximately 3.6 at $d = 20$ nm . The data presented in this chapter are the transverse analogue of Sabisky and Andersons experiment in which they generated longitudinal acoustic waves at frequencies of around 30 GHz in ^{4}He films. The sharp standing wave resonances they observed as a function of the vapour pressure over the film are in contrast with the heavily damped resonances of transverse waves and the film thickness obtained from transverse measurements is correspondingly less precise.

Sabisky and Anderson compared their data for $V(d)$ with calculations based on the DLP theory of film thickness, in which the potential is completely specified by the imaginary part of the complex frequency dependent dielectric susceptibilities of the interacting media (Chapter 2). Using models for the dielectric constants of the substrate and the helium film, they obtain excellent agreement between theory and experiment for their SrF_2 substrate and have also calculated the van der Waals potential of a helium film adsorbed on various other substrates, some of which are shown in Figure 5.11. The potential $V(d)$ is expressed so as to show the deviation at large film thicknesses from the simple inverse-cube law $V \alpha 1/d^3$

$$A(d) = \frac{mgh}{K_b} \left(\frac{d}{d_o}\right)^3 \qquad (5.5.2)$$

where $d_o = 0.36$ nm is the standard thickness of ^{4}He monolayer and the units of $A(d)$ are therefore $°K(\text{layers})^3$. $A(d)$ for the 6 films of

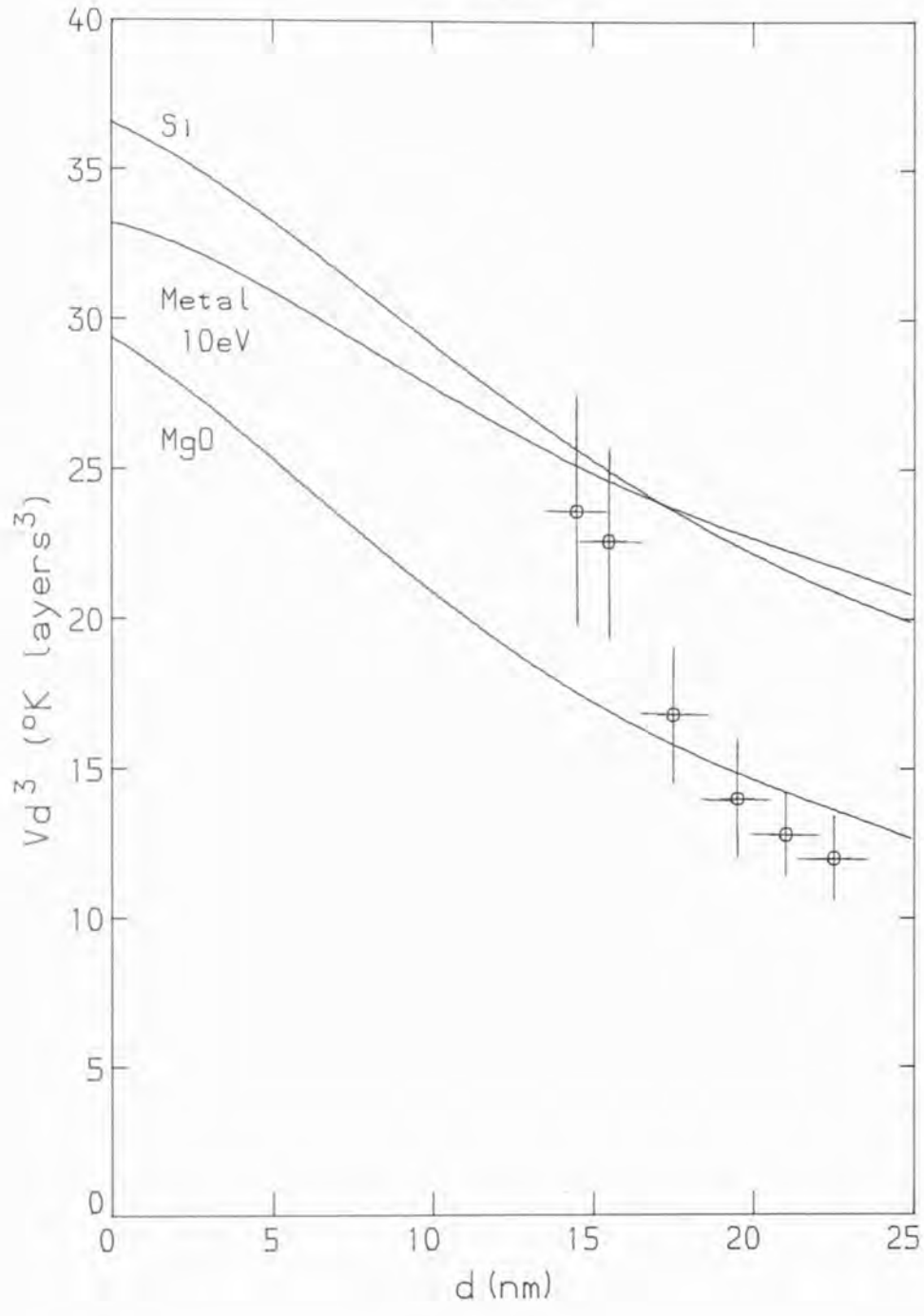

Figure 5.11

$A(d) = (mgh/K_b)(d/d_o)^3$ as a function of film thickness d for the data of Figure 5.10 and for various substrates.

Figures 5.1-5.6 are tabulated in Figure 5.16 and are plotted against film thickness d in Figure 5.11, together with $A(d)$ calculated by Sabisky and Anderson for helium films adsorbed on substrates of Si, MgO and a metal with a plasma frequency of 10 eV.

The quartz crystal resonator appears to have a van der Waals surface potential similar to that of MgO, though the presence of the gold plating, thickness 150 nm, on the crystal will complicate the potential by introducing the effects of a different substrate. Gold has a plasma frequency $\omega_p = ne^2/\varepsilon_o m_e$ of 9 eV and for the purpose of comparison the potential $A(d)$ of a metal with $\omega_p = 10$ eV is plotted in Figure 5.11. For thin films, $A(d)$ tends to a constant value; Chester, Yang and Stephens (1972) estimate a value of 40 °K(layers)^3 for similar gold plated crystals.

Hemming (1971) used an ellipsometric technique to measure the thickness of saturated helium films adsorbed on both polished quartz and on a gold film of thickness 210 nm evaporated onto the quartz. At temperatures just below the λ-point and for a height 1 cm above a bulk liquid helium surface, he gives $n = 3.9 \pm 0.2$ with $d = (32.3 \pm 0.3)$nm for the gold substrate and $n = 3.1 \pm 0.1$ with $d = (22.8 \pm 0.2)$nm for the quartz. These compare with $n = 4.0 \pm 0.4$ and $d = (22.5 \pm 1)$nm found here for the helium film adsorbed on the gold electrodes of the quartz crystal at a height 1 cm above the bulk liquid helium level.

5.6 The Vortex Resonance

5.6.1 The Vortex Wave Dispersion Relation

The data of Figures 5.1-5.6 shows features that are not predicted by the theory of the previous sections for the film in its hydrodynamic and ballistic regions. The locus of X versus R for film thickensses of 14.5 and 21 nm is shown in Figure 5.7; in the region of the anomally

the data describes a circle, the diameter of which increases with film thickness. The presence of such a circle on the Argand diagram is reminiscent of the electrical impedance plot of a resonant circuit with parasitic resonances, implying that there is some type of resonance coupling into and driven by the crystal's oscillation. The likelihood that this resonance is due to the crystalitself is discussed in section 5.7, a more interesting possibility is that the oscillation of the crystal is exciting waves on vortices pinned to its surface. These would resonate at $d = \lambda/4$ with a node at the crystal surface and an antinode at the free film surface.

Vortex waves were first reported by Hall (1958) who interpreted the resonance effects obtained when a stack of closely spaced discs were set into oscillation in a rotating cryostat as due to $n\lambda/2$ resonances of vortices pinned between the plates. This was followed by the identification of the $\lambda/4$ resonance between an oscillating disc and a free helium surface (Andronikashvili and Tsakadze (1960), Hall (1960), and Nadirashvili and Tsakadze (1968)). These observations were at frequencies of a few Hertz, with correspondingly long wavelengths, typically 500-1000 μm . At much higher frequencies, 10 MHz, Ashton and Glaberson (1979) have reported exciting the pure Kelvin wave (Chapter 2.6) by coupling a circularly polarised electrical field to ions moving along the vortex line. In vortex arrays, where the interaction between vortex lines becomes non-negligible, more complex lattice displacement waves are observed (Glaberson (1982), and Andereck and Glaberson (1982)).

Figure 5.12 shows the film thickness plotted against the temperature of the resonance, taken as being the temperature of the maximum in the response of R at 20 MHz. Since the film thickness determines the

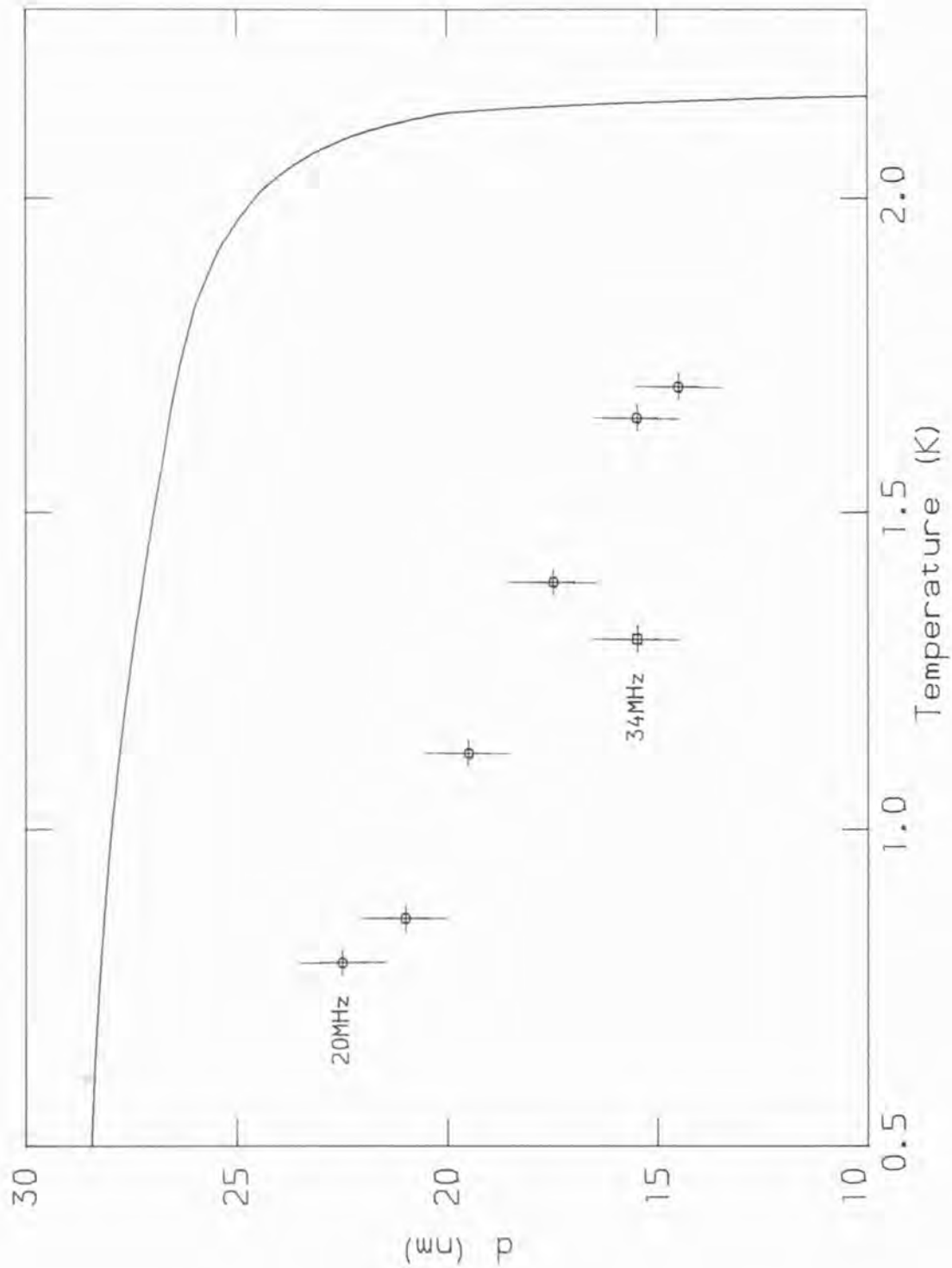

Figure 5.12

The temperature dependence of the resonance in the superfluid film and of the resonance at $d = \lambda/4$ of Kelvin waves on pinned vortices at 20.5 MHz .

wavelength of the vortex wave, $\lambda = 4d$, Figure 5.12 shows the wavelength of the resonant wave decreasing approximately linearly with temperature over the range of the data. In addition to these six resonances observed at 20.5 MHz, a similar resonance was also seen at 34.1 MHz, the frequency corresponding to the 5^{th} harmonic shear mode of the crystal, at a film thickness of 15.5 nm as shown in Figure 5.12.

The dispersion relation for vortex waves is given in Chapter 2, equation (2.6.15) as

$$\omega = (T_o/\rho_s\kappa)k^2 \qquad (5.6.1)$$

where $k = 2\pi/\lambda$ and for the lowest order resonance, with a node at the crystal surface and an antinode at the liquid-vapour interface, $\lambda = 4d$. At resonance therefore, assuming the tension T_o is independent of k the frequency of the wave is given by

$$f_v \alpha\ d^{-2} \qquad (5.6.2)$$

The resonance observed at 34 MHz occurred at a temperature of 1.30 K in a film of thickness $d_{34} = 15.5$ nm . At 20 MHz, this would be equivalent to a resonance in a film of thickness d_{20} where

$$d_{20} = d_{34}\sqrt{\frac{34.142}{20.496}} = 20.0 \text{ nm} \qquad (5.6.3)$$

As can be seen from the data at 20 MHz in Figure 5.12, this is within the error bars of the film thickness that would be expected for a resonant temperature of 1.30 K and a frequency of 20 MHz. The resonances at 20 and 34 MHz are thus consistent with the dispersion relation expected of a vortex wave, equation (5.6.1).

In the long wavelength limit, $\lambda >> a$, the dispersion relation, equation (5.6.1), for the Kelvin wave is

$$\omega = \frac{\kappa k^2}{4\pi} \left[\ell n \left(\frac{1}{ka} \right) + 0.1159 \right] \qquad (5.6.4)$$

for a hollow core vortex (equation 2.6.15). Here the tension T_o of equation (5.6.1) is both wavelength and temperature dependent through the superfluid density ρ_s and the effective core radius a, taken as increasing from 0.1 nm at 0.6 K to 0.3 nm at 2.0 K (Barenghi, Donnelly and Vinen (1983)). Taking the frequency of equation (5.6.4) to be 20.5 MHz, it is possible to find the resonant wavelength $\lambda(T)$ and hence the film thickness $d = \lambda/4$ predicted for the resonance. As shown in Figure 5.12, the film thickness for the resonance of the hollow core vortex is far larger than that observed, and decreases sharply as $T \rightarrow T_\lambda$ and the core parameter diverges.

Barenghi, Donnelly and Vinen (1985) have estimated the shift in the frequency of a vortex wave caused by the interaction of the vortex line with the excitations of the normal fluid. The fractional change in frequency is given by (equation (2.6.19)a)

$$\frac{\Delta f}{f} = \frac{\gamma(\rho_s \kappa - \gamma_o')}{\gamma_o \rho_s \kappa} - 1$$

where γ_o , γ_o' and γ are the coefficients of mutual friction given in Chapter 2.6. $\Delta f/f$ increases rapidly as $T \to T_\lambda$, but over the temperature range of interest here, the change in frequency is less than 2% of the frictionless value and the change in the resonant film thickness of the Kelvin wave, equation (5.6.4), is negligible.

The tension T_o of equation (5.6.1) represents the energy per unit length of vortex line at $T = 0$ K . The tension, however, is in general equivalent to the free energy/unit length of line and therefore for $T > 0$ K will have contributions from waves thermally excited on the vortex such that the effective tension T_{eff} is given by

$$T_{eff} = T_o + F_W \qquad (5.6.5)$$

where F_W is the free energy/unit length of the waves excited on the line,

$$F_W = - K_b T \ell n Z_W \quad .$$

The partition function Z_W is given by Barenghi et al (1985) as

$$\ell n\, Z_W = - \sum_{i=1}^{N} \{\ell n\left[1 - e^{-\frac{\hbar\omega_i^+}{K_b T}}\right] + \ell n\left[1 - e^{-\frac{\hbar\omega_i^-}{K_b T}}\right]\}$$

where n is a Debye cutoff, and the energy of the wave is considered to be quantised in units of $\varepsilon^{\pm} = \hbar\omega^{\pm}$.

Since $F_W < 0$, the excitation of vortex waves reduces the effective tension of the line and the ratio ω/k^2 will be lower than that of the Kelvin wave, as observed; at 1.3 K, the data gives

$\omega/k^2 = 1.7 \times 10^{-5}\ m^2\ s^{-1}$, equation (5.6.4) gives $\omega/k^2 = 3.6 \times 10^{-5} m^2 s^{-1}$.

Barenghi et al point out that $|F_W|$ becomes very large as $T \to T_\lambda$ and at $T_\lambda - T \simeq 0.3$ K a free energy catastrophe occurs, the system lowering its energy by the spontaneous creation of vortices. This is inconsistent with experiment and is due, they suggest, to their assumption that the helium's excitations are unaffected by the presence of a vortex.

5.6.2 The Impedance of a Vortex Line

The waves associated with the dispersion relation of equation (5.6.1) are circularly polarised with a helical deformation that propagates along the vortex line. Of the two possible modes, the positive wave ω^+ has a sense of rotation in the same direction as the superfluid velocity circulation, and as discussed in Chapter 2.6, is evanescent for frequencies less than $\omega_o/2\pi = 3 \times 10^{11}$ Hz . The negative wave ω^- , with a rotation in the opposite sense to the superfluid circulation is a propagating mode and for frequencies $\omega << \omega_o$, $k_+ = ik_-$.

A vortex line pinned to the crystal is constrained to move with the crystal's oscillatory motion at its pinning site. The resulting displacement will propagate along the line and the vortex will experience a force transverse to its initial displacement due to the Magnus force effect. If the displacement of the vortex at any point z along its length is $(\xi, \eta, 0)$ as before in Chapter 2, with the crystal lying in the xy plane and vibrating along the y axis, then the boundary conditions for the vortex at the crystal surface are

$$\eta(z = 0) = \eta_o e^{i\omega t}$$

$$\xi(z = 0) = 0 \qquad (5.6.6)$$

The free end of the vortex terminates on the film surface, perpendicular to the interface, leading to the conditions

$$\left.\frac{\partial \eta}{\partial z}\right]_{z = d} = \left.\frac{\partial \xi}{\partial z}\right]_{z = d} = 0 \qquad (5.6.7)$$

At any point z, the total vortex line displacement is the sum of the amplitudes of both forward travelling and reflected positive and negative waves. From equation (2.6.15), the relation between the x and y displacements of the line is $\eta_{\pm} = \mp i\xi$, hence the total displacement is

$$\xi(z) = ie^{i\omega t}(A_1 e^{-ik_- z} + A_2 e^{ik_- z}) - ie^{i\omega t}(B_1 e^{-ik_+ z} + B_2 e^{ik_+ z})$$

$$\eta(z) = e^{i\omega t}(A_1 e^{-ik_- z} + A_2 e^{ik_- z}) + e^{i\omega t}(B_1 e^{-ik_+ z} + B_2 e^{ik_+ z}) \qquad (5.6.8)$$

where A_1 and A_2 are the amplitudes of the forward travelling and reflected negative wave ω^-, respectively, and B_1 and B_2 are the amplitudes of the evanescent wave ω^+.

Recalling that $k_+ = ik_- = ik_o$, equations (5.6.6) - (5.6.8) are solved to give

$$A_1 = \frac{\eta_o}{2(1 + e^{-2ik_o d})} \quad ; \qquad A_2 = A_1 e^{-2ik_o d} \qquad (5.6.9)$$

and

$$B_1 = \frac{\eta_o}{2(1 + e^{2k_o d})} \quad ; \quad B_2 = B_1 e^{2k_o d} \tag{5.6.10}$$

The amplitude of the forward travelling negative wave ω^- diverges for $e^{-2ik_o d} = 1$ giving a resonance condition for the vortex wave at

$$d = (2n - 1)\frac{\lambda}{4} \quad , \quad n = 1, 2, 3, \ldots$$

as required.

In summary, therefore, the boundary conditions of linear oscillation imposed by the crystal on the motion of the vortex at its surface can be satisfied by assuming that the vortex line is able to support waves of frequency ω^- and ω^+, with wavevectors k_- and k_+ respectively, where ω^- is a propagating mode which resonates in a film of thickness $d = \lambda/4$, and ω^+ may be evanescent.

A vortex has associated with it a tension/unit length T_o, and as it moves will therefore exert a force upon the crystal. If the vortex is inclined to the direction of the crystal vibration such that the angle between the normal to the crystal plane and the vortex is α, then the shear stress on the crystal is given by

$$T_o \sin\alpha \simeq T_o[\partial\eta/\partial z]_{z=0}$$

The transverse acoustic impedance measured by the crystal is defined (equation (2.3.5)) as the ratio of the shear stress on the crystal to its surface velocity, hence for an array of N vortices/unit area pinned to the crystal, the impedance is

$$Z_v = - T_o N \frac{[\partial\eta/\partial z]_{z=0}}{[\partial\eta/\partial t]_{z=0}} \qquad (5.6.11)$$

Setting $k_+ = ik_o$ and $k_- = (1 - i\nu)k_o$ where ν characterises the damping of the negative wave, and using equation (5.6.8) for $\eta(z)$

$$Z_v = \frac{T_o N}{2\omega} k_o[(\nu + i)\tan((1 - i\nu)k_o d) - i\tanh(k_o d)] \qquad (5.6.12)$$

where the tension, given by equation (2.6.15) is $T_o = \rho_s \kappa\omega/k_o^2$. Hence

$$R_e(Z_v) = \frac{\rho_s \kappa N}{2k_o} \frac{\nu\tan(k_o d)[1 - \tanh^2(\nu k_o d)] + \tanh(\nu k_o d)[1 + \tan^2(k_o d)]}{1 + \tan^2(k_o d)\tanh^2(\nu k_o d)} \qquad (5.6.13)$$

$$\ell m(Z_v) = \frac{\rho_s \kappa N}{2k_o} \frac{\tan(k_o d)[1 - \tanh^2(\nu k_o d) - \nu\tanh(\nu k_o d)[1 + \tan^2(k_o d)]}{1 + \tan^2(k_o d)\tanh^2(\nu k_o d)} - \tanh(k_o d)$$

For each film thickness d, there are therefore two parameters characterising the resonance; ν, determining the quality factor of the wave and N, the number of vortices pinned per unit area to the crystal.

5.6.3 Discussion

The vortex impedance $Z_v(T) = R_v(T) - iX_v(T)$ given by equations (5.6.13) (a) and (b) is, for a given film thickness d, dependent on temperature only through the superfluid density ρ_s and the wave vector of the vortex wave $k_o = 2\pi/\lambda$. $k_o(T)$ at a frequency of 20 MHz is found from Figure 5.12 by assuming a linear relation between the film thickness $d = \lambda/4$ and temperature T. The vortex impedance calculated from equations (5.6.13) is shown added to the impedance of

the film in the hydrodynamic region (equation (5.3.1)) in Figures 5.13 and 5.14 for $d = 14.5$ and 21 nm respectively. Comparison of figures such as these with the data of Figures 5.1-5.6 gives $N = (25 \pm 10) \times 10^{12}$ m^{-2} and $\nu = 0.06 \pm 0.01$ for the films with $d < 20$ nm and $\nu = 0.08 \pm 0.01$ with $N = (30 \pm 10) \times 10^{12}$ m^{-2} for $d = 21$ nm. The quality factor of the resonance, $Q_v = 1/2\nu$ therefore has a value ~ 8 for $d < 20$ nm and ~ 6 for $d = 21$ nm. As discussed below, it is possible to attribute the decrease in Q_v at 21 nm and the distortion of the resonance at 22.5 nm to unpinning of vortices at high amplitudes of crystal vibration.

As discussed in Chapter 2.6.2, the wave is damped as a consequence of the interaction of the vortex line with the excitations of the normal fluid. The quality factor of the resonance is therefore determined by the mutual friction coefficients of the drag force, and from equation (2.6.19)(b)

$$Q_v = \frac{\rho_s \kappa}{2\gamma} \qquad (5.6.14)$$

where γ is tabulated as a function of temperature by Barenghi, Donnelly and Vinen (1983). Q_v thus calculated is tabulated in Figure 5.16 for each resonance temperature, and is seen to increase from ~ 4 at 1.7 K for the thinnest film to ~ 1000 at 0.8 K for the thickest. This is in contrast with the behaviour actually observed of the resonance, with Q_v constant for $T \gtrsim 1$ K and lower for $T \lesssim 1$ K.

The frictional force of the excitations interation with the vortex core is applied over the fluid within a distance ℓ of the vortex line, where ℓ is the mean free path of the excitations. The vortex

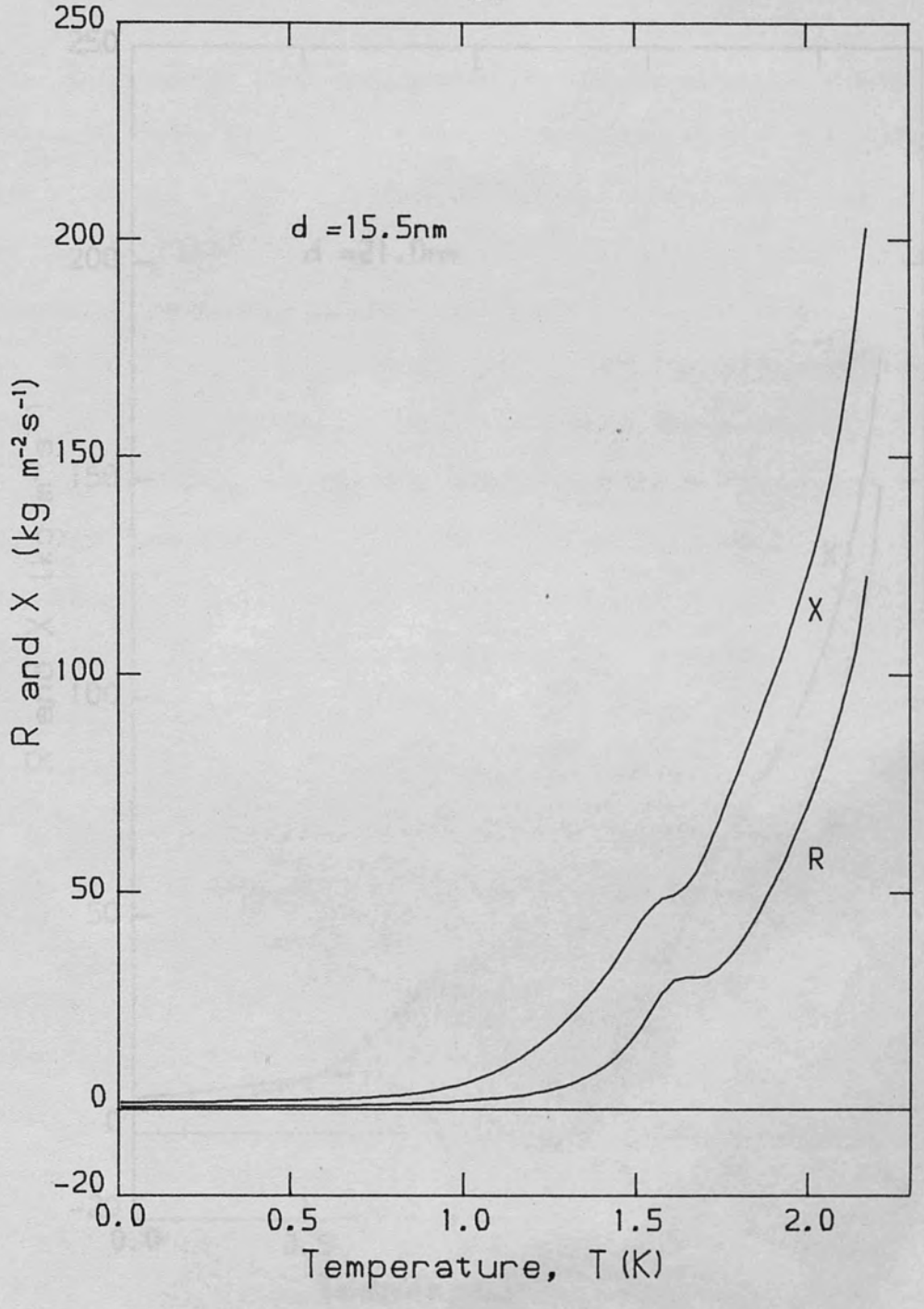

Figure 5.13

The temperature dependence of R and X for a film of thickness 15.5 nm with a vortex resonance at 1.65 K .

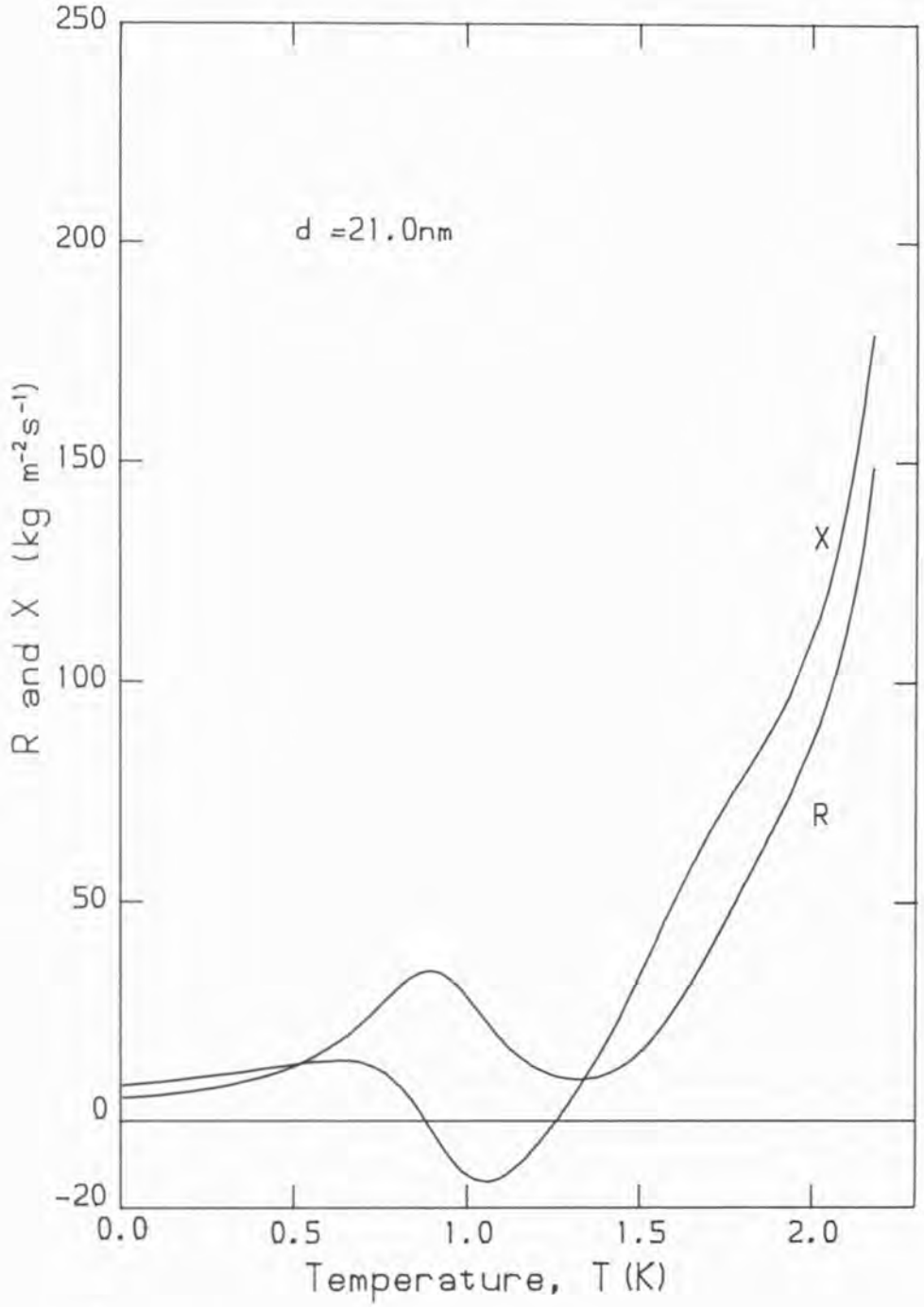

Figure 5.14

The temperature dependence of R and X for a film of thickness 21 nm with a vortex resonance at 0.06 K .

also drags normal fluid around with it, and the effective friction force on the vortex line is frequency dependent through the ratio ℓ/δ , where δ is the viscous penetration depth. Following Barenghi et al (1983) the value of γ at 20 MHz can be estimated for $\ell/\delta \ll 1$. The resulting quality factors are lower than Q_v at zero frequency; at 1.7 K $Q = 2.5$ compared with 4.0 , and the difference becomes less at lower temperatures. The frequency of the measurements thus lowers the quality factor to be expected of the resonance, and the discrepancy between the actual Q_v and that calculated from mutual friction considerations remains unresolved.

In his observations of the resonance of vortex lines pinned between oscillating discs, Hall (1958) found $Q_v \sim 3$ for the main $\lambda/2$ resonance and $Q_v \sim 10$ for the $3\lambda/2$ resonance at 1.7 K . He attributed the low values of the Q's and the discrepancy between them to the slipping of the vortex lines over the surface of the discs at high amplitudes of oscillation. If slipping of the vortex lines occurs in a similar manner on the crystal electrodes, it will depend upon the amplitude and velocity of vibration of the crystal surface, these both increase as temperature decreases, becoming large for $T \lesssim 1$ K where the mass and viscous loading of the helium film is least.

In support of the above argument is the behaviour of the resonance of the crystal itself. The crystal's response showed a similar type of instability to that observed at $d = 21$ nm and $T = 0.75$ K , though to a much greater extent, at 34 MHz for $T \lesssim 1$ K . In both cases the Q of the crystal was not a smooth and continuous function of frequency as in Figure 3.3, but exhibited features that could not be explained by the simple parallel resonance model for the crystal of Chapter 3. Figure 5.15 shows typical Q-curves of signal S versus

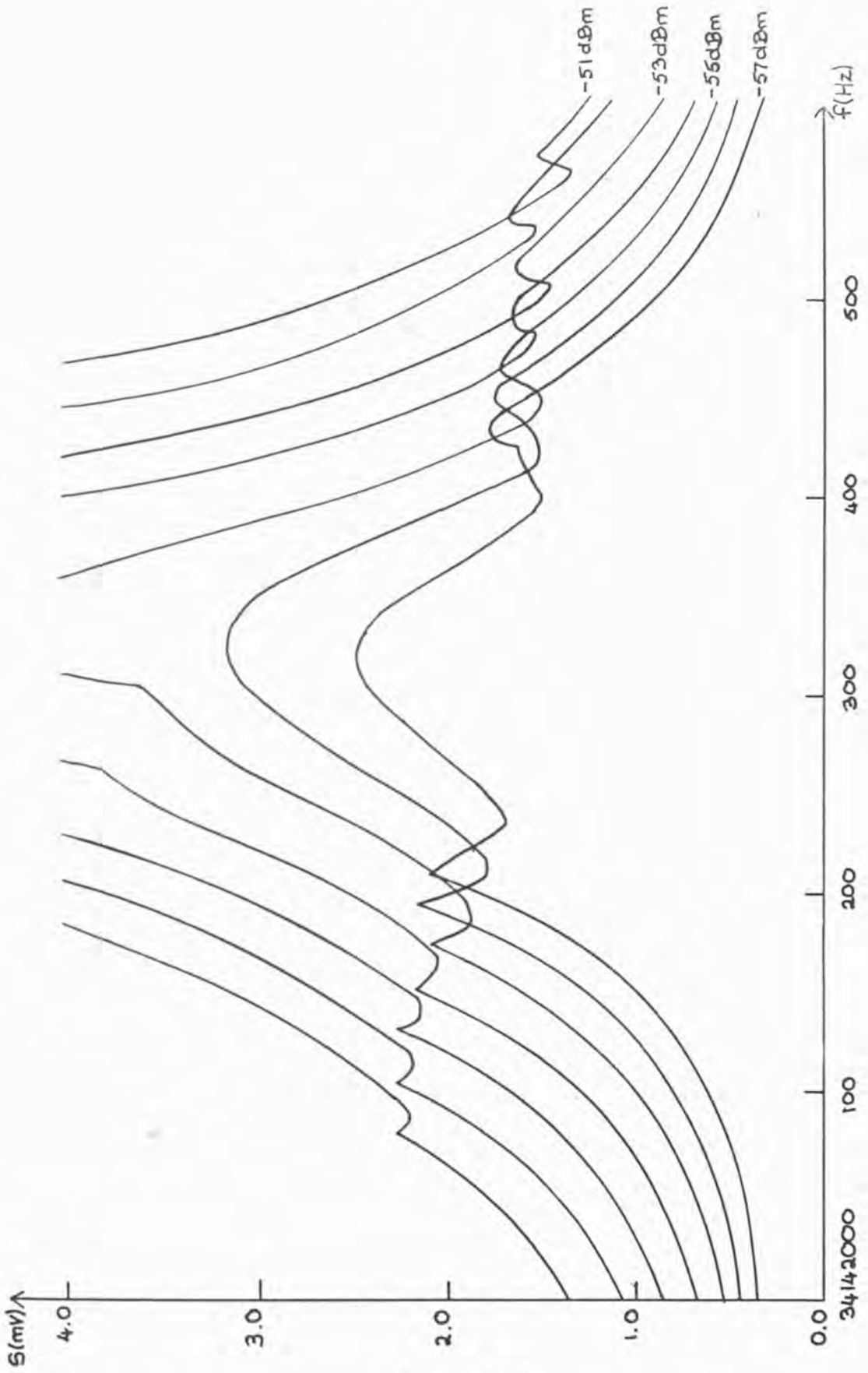

Figure 5.15

The signal S as a function of frequency at 34 MHz for various power levels.

frequency for the crystal at 34 MHz for input power levels of between -57 and -51 dBm (corresponding to power dissipations in the crystal of between 0.9 and 4 nW). Since $s \propto \sqrt{i}$ where i is the current through the crystal, from equations (3.2.4) and (3.2.5), the amplitude and velocity of the crystal's vibration at which the break in signal occurs is approximately independent of power input and in the vortex resonance model must represent the magnitude of the crystal motion at which vortex lines become unpinned from the surface.

A classical vortex tends to stick to a surface protuberance because of the Bernoulli pressure drop at the centre of the line associated with the fluid's circulatory velocity field. Slipping of the line then occurs when the vortex detaches itself from its original pinning site and jumps to a neighbouring protuberance. Counter flow experiments in narrow channels filled with arrays of vortices pinned to surfaces of varying degrees of roughness (Yarmchuk and Glaberson (1978), and Hedge and Glaberson (1980)) indicate the existance of critical velocities associated with the unpinning of vortex lines. Similar conclusions have been reached by Schwartz (1985) using a vortex filament model to analyse boundary-line interactions. In a steady superfluid flow, a pinned vortex moves to assume a stationary configuration such that its self-induced velocity balances the applied velocity field. As the superfluid velocity increases, so does the deformation of the vortex until the line at its pinning site lies parallel to the surface and it is swept away.

The vortex lines pinned to the crystal will have a large amplitude displacement at resonance. For $T \lesssim 1$ K the high vortex resonance quality factor will exaggerate the large crystal vibration amplitude and the vortex motion may be sufficiently violent to cause unpinning of the lines. Pinning vortices will attach themselves preferentially to the largest surface protuberances, hence as the density of lines increases

and less favourable pinning sites are occupied, the force associated with the mass unpinning of lines is reduced. Yarmchuk and Glaberson (1978) estimate an average pinning force of $\sim 10^{-12}$ N per line for a vortex array of density 2×10^8 lines/m^2 on a glass surface. Simultaneous unpinning of a large line density of vortices will obviously have a major effect on the crystal's behaviour, and it is possible that this is the cause of the discontinuity in the crystal resonance curves of Figure 5.15.

It was mentioned earlier that the expressions derived for the vortex resonance, equations (5.5.13), when fitted to the data, yield a vortex density N of $(25 \pm 10) \times 10^8$ lines/cm^2. This corresponds to a line spacing of approximately 0.2 μm and it is not clear whether the existance of such a large vortex line density is possible. In rotating helium, the line density n_o of the vortex array is proportional to its angular velocity, equation (2.6.3), typically $n_o = 10^4$ lines/cm^2, equivalent to a spacing of ~ 0.1 mm.

The presence of vortices in non-rotating helium, a so-called primordial vortex line density has been confirmed by Awschalom and Schwarz (1984) using an ion-trapping technique. If negative ions are drifted between two parallel plates with vortex lines pinned between them, some will be captured by the vortices and under the influence of a suitable electric field, will be delivered to the collector plate. The signal was calibrated against measurements in rotating helium with a known vortex line density, and a remnant line density of approximately 15 lines/cm^2 was found for a plate spacing of 1 cm. Awschalom and Schwarz estimate the maximum line density present by noting that to avoid recombination of neighbouring vortices, the maximum displacement of each line must be less than about half the interline spacing. They give

$$N \lesssim \frac{2\ell n(D/a)}{D^2}$$

where a is the vortex core radius, which for $D = 1$ cm gives $N \lesssim 35$ lines/cm^2, in very good agreement with the experimental determination. For a helium film of thickness $d \equiv D/2$ of 20 nm, this gives $N \lesssim 10^{12}$ lines/cm^2.

The primordial line density measured by Awschalom and Schwarz was independent of the history of the system and the vortices must therefore be created as helium passes through the λ-transition such that its total vorticity is zero. Equal numbers of vortices with opposite senses of superfluid velocity circulation then exist and are stabilised by pinning. Such vortices may then, under suitable conditions, initiate the growth of a vortex line tangle and hence superfluid turbulence, either by acting as a continuous source of vorticity as suggested by Glaberson and Donnelly (1966) or else, as implied by the interpretation of the data presented here, by actually becoming unpinned from the surface and being swept away with the flow (Schwarz, 1985).

5.7 Alternative Resonances

5.7.1 Crystal Effects

It is possible that changes in the quality factor and resonant frequency of the crystal such as those represented by the anomalous behaviour of R and X in Figures 5.1-5.6 may be due to the crystal rather than the film. Specifically, coupling of unwanted modes of vibration to the main resonance mode or a change in the energy trapping properties of the crystal may cause abrupt changes in both Q and f.

An AT-cut crystal is designed to resonate in a thickness-shear (TS) mode with a frequency determined principally by its thickness. The finite dimensions of the crystal plate and non-linearities in its elastic properties however, mean that unwanted modes of vibration - flexural, face-shear or anharmonic TS modes, will be present in the crystal's vibrational spectrum. If the frequency of an unwanted mode approaches that of the main TS resonance, there is a coupling between the two, resulting in a frequency jump and an activity dip (a reduction in the Q of the crystal). The flexural and face-shear modes are generally weak, being high overtones of fundamental frequencies dependent on the diameter of the crystal, but the anharmonic TS modes with frequencies a few percent higher than the corresponding harmonic mode may be quite strong. Under favourable conditions, both are able to couple to the harmonic TS mode. The development of the theory of mode coupling and of design features used to supress it are reviewed by Bahadur and Parshad (1982).

If the crystal plate is bevelled, its activity is forced away from the crystal edges, reducing both energy loss through the crystal mounting and coupling of flexural vibrations to the TS mode. For high frequency resonators, $f > 10$ MHz , the motional area of the crystal becomes increasingly confined to that part of the plate covered by the electrodes. In this case, bevelling has little effect and the crystal is usually plane parallel (Birch, 1965).

The crystal electrodes can themselves be very effective in supressing unwanted vibrations by a process known as mode trapping. The mass of the electrodes can be considered to increase the effective density of the quartz beneath. Thus the cut-off frequency, below which no wave will propagate in the quartz will be higher in the unelectroded region than in the electroded region; $\omega_e < \omega_s$. If a vibrational mode has

frequency ω with $\omega > \omega_s$, the wave propagates freely in the entire crystal and dies out due to mounting and other losses. If $\omega_e < \omega < \omega_s$, the wave will propagate freely in the region beneath the electrodes but will suffer exponential attenuation in the unelectroded region. Waves with $\omega < \omega_e$ will obviously not propagate at all. Therefore only energy in the vibrational modes with $\omega_e < \omega < \omega_s$ is trapped beneath the electrodes and it is possible to restrict the range of trapped frequencies by controlling the amount of electrode mass deposited on the crystal. The electrodes therefore also affect the resonant frequency of the TS mode, the fractional lowering of frequency due to the increased effective density of the quartz beneath the electrodes is known as plateback and elsewhere in this thesis has been called 'the mass loading effect'.

Werner and Dyer (1976) have estimated the degradation of Q due to imperfect energy trapping for an AT-cut quartz crystal at its 3rd harmonic $n = 3$ at frequency 20.1 MHz. At low mass loading Q is small due to loss of energy from the electrode region into the periphery of the crystal, but for a fractional mass loading $\Delta M/M > 0.004$, where M is the mass of the crystal plate per unit area and ΔM is its total surface loading, Q is approximately constant. At very high mass loading unwanted vibrations become trapped. The AT crystal used in these measurements was driven at 20.5 MHz ($n = 3$) and had gold electrodes of thickness 150 nm, giving a fractional mass loading $\Delta M/M = 0.0087$. The effect of the helium on the crystal's energy trapping behaviour can be estimated by assuming that all the helium, density 145 kgm^{-3}, within a distance 20 nm of the crystal surface will be mass loading it. This gives $\Delta M/M = 8 \times 10^{-7}$, negligible in comparison with the effect of the electrodes. When much of the film is

superfluid and does not load the crystal, as is the case in the region of anomalous behaviour of Figures 5.1-5.6, $\Delta M/M$ will be correspondingly much less.

In general, the presence of unwanted vibrations coupling into the main resonant TS mode leads to 'bandbreaks' - irregularities in the frequency-temperature and activity-temperature characteristics of the crystal in vacuum. It is possible that the anomalous behaviour of R and X may be due to coupling driven by changes in the mass loading of the crystal with both temperature and film thickness. Below 1.2 K however, where the largest effects occur, the film is predominently superfluid, $\rho_n = 4\ kgm^{-3}$ at 1.2 K , and the change in fractional mass loading between film thicknesses of 14 and 22 nm at a given temperature will be very small.

Extensive measurements in bulk ^{4}He, both normal and superfluid and in liquid at high pressures where the ratio $\Delta M/M$ would have been swept over a larger range than it was here, have shown no anomalous behaviour that may be attributed to the crystal itself.

At liquid helium temperatures, the properties of quartz change only very slowly with temperature, f_s and Q were found to be virtually independent of temperature below 4 K in vacuum (Chapter 3). In all measurements, the power dissipation in the crystal was kept as low as possible (typically 3 nW) to avoid heating of the film, and though there was a slight power dependence of the crystal resonance in the 21 nm film at 0.7 K , the power levels were much lower than those reported by Birch and Weston (1976) (5-10 mW) to cause drive level sensitive coupling due to the non-linear elastic properties of the quartz.

An attempt was made to find unwanted modes directly by breaking the feedback loop of the frequency locking system and observing the output signal S of the crystal on an oscilloscope as a function of frequency. Resonances were found at 13.6 and 27.3 MHz corresponding to the TS modes at $n = 2$ and $n = 4$, and at frequencies of 20.54 and 20.56 MHz, probably the anharmonic TS resonances. In addition there were smaller resonances at 20.67, 20.77 and 29.15 MHz, these may be either face-shear or flexure modes. All these resonances were very weak, at least 30 dB down on the main harmonic ($n = 3$) TS mode and, as far as could be determined, were independent of temperature and mass loading and thus unlikely to couple into the wanted mode with as much temperature and mass loading dependence as observed.

An obvious way to determine whether mode coupling is present is to use a different crystal. Unfortunately there was insufficient time to do this, though it must be noted that Forder, Halse and Brown (1975), using an AC-cut crystal vibrating in a shear thickness mode at frequencies of 3 and 10 MHz found that the smooth crystal response to the film had superimposed upon it a small variation which was periodic in the height of the crystal above the helium bath. This they attributed to the coupling of flexure vibrations into the main resonant mode. It does not however, seem likely that two different types of crystal should exhibit mode coupling under similar conditions and it would appear more likely that the effect is connected with the helium film adsorbed on the crystal rather than with the crystal itself.

5.7.2 Resonances in the Film

It is necessary to consider whether the resonance observed could be due to anything other than pinned vortex lines or mode coupling in the crystal.

If the crystal does not vibrate in a purely shear mode as an AT-cut crystal is designed to do, any longitudinal component of surface particle motion could excite sound waves in the helium. If this occurs, however, there would be an energy loss $\Delta(Q^{-1})$ from the crystal proportional to ρu_1, where u_1 is the speed of first sound. Such a loss would have been observed as a function of density in measurements of the impedance of He II under pressure and was not (Lea and Fozooni, 1984). There is, therefore, no reason to presuppose the excitation of sound waves in the film and with a speed $u_1 = 238\ ms^{-1}$ for $T \lesssim 1\ K$ and hence a wavelength of $\sim 12\ \mu m$ at 20 MHz , no resonance would occur.

A further possibility that needs to be considered is the excitation of surface waves on the film by the transverse motion of the crystal. For thin films, $d << \delta$, the relevant wave is third sound; the normal fluid component is clamped to the substrate by its viscosity and the wave motion is confined to the oscillation of the superfluid. The velocity of third sound is typically $\sim 300\ cms^{-1}$ (Atkins and Rudnick, 1970), which is considerably higher than the critical velocity of the film, $V_c \sim 30\ cms^{-1}$ at $d = 20\ nm$. Pure third sound propagation, however, will not occur under the experimental conditions appropriate to the film impedance measurements since $d \sim \delta$ and the normal fluid component is not fully locked to the crystal and will participate in any surface motion. It is necessary therefore, to consider more general types of surface waves (see for example, Landau and Lifshitz, 1959), with frequency $f = \omega/2\pi$

$$\omega^2 = \left(f_m k + \frac{\alpha k^3}{\rho} \right) \tanh(kd)$$

where $\alpha \simeq 3.3 \times 10^{-4}$ Nm^{-1} is the surface tension of the film and f_m is the restoring force per unit mass which for the film on the crystal is $f_m = 3AK_b/md^4$, assuming the d^{-3} form of the van der Waals' surface potential. For $d = 20$ nm and $f = 20$ MHz, this corresponds to a wavelength of $\lambda \sim 900$ nm. This, however, assumes both normal and super-fluid components move together, which is unlikely since the vibration of the normal fluid component will be damped by its viscosity. It appears though, that any surface wave will have a wavelength short in comparison with the size of the crystal electrodes (2.5 mm) and will be heavily damped. Taking into account the geometry and configuration of the film on the crystal, it therefore seems unlikely that any surface motion will be able to form a standing wave and resonate on the film.

h (cm)	d (nm)	$A(d) = Vd^3$ ($°K(layers)^3$)	Temperature of resonance	Q_v (zero frequency)
7.64	14.5	23.6	1.70	4.0
5.99	15.5	22.6	1.65	4.5
3.10	17.5	16.8	1.39	10
1.87	19.5	14.0	1.12	40
1.37	21.0	12.8	0.86	450
1.04	22.5	12.0	0.79	1000

Figure 5.16

Table giving the crystal surface potential A(d) for film thickness d at height h above the bulk liquid surface, the temperature of the resonance observed and the quality factor calculated for the vortex resonance.

Chapter 6

The Helium Film at $T > T_c$

6.1 Introduction

At a temperature above that of the liquid-gas critical point T_c, the increase in fluid density near the crystal caused by van der Waals' forces does not result, as at lower temperatures, in the formation of a film with a well defined interface between the liquid and vapour phases. The density of the helium instead increases smoothly to the solidification pressure as the crystal is approached, though for temperatures only just above T_c, the fluid may become highly compressed under the crystals surface potential, its density changing rapidly from a gas-like to a liquid-like value.

The data presented in this chapter consists of measurements at 20 MHz of the transverse acoustic impedance, $Z = R - iX$, of ^4He at a temperature of 5.239 K, $((T - T_c) = 49$ mK) for pressures less than 2000 τ. In the critical region, $P \sim 1700$ τ, the helium has a large compressibility and, since the extent of the high density fluid is small compared with the penetration depth δ, $X - R$, is as before, a measure of the excess effective mass adsorbed on the crystal surface (section 6.2). The effective viscosity of the helium can be found from the real part R of the measured impedance, provided the fluid density $\rho(T,P)$ is known. At low densities the viscosity shows the transition of the helium gas from hydrodynamic to non-hydrodynamic behaviour, (section 6.3).

6.2 The Excess Mass Adsorbed on the Crystal

The transverse acoustic impedance $Z = R - iX$ of ^4He was measured at a temperature 49 mk above the liquid-gas critical point ($T_c = 5.1899 \pm 0.0001$ K , $P_c = 1706.1 \pm 0.1$ τ , $\rho_c = 69.64 \pm 0.07$ kgm^{-3} , (Kierstead, 1971)). The real and imaginary parts, R and X of the impedance are plotted in Figure 6.1 for pressures $P < 2000$ τ . The baselines $R = 0$ and $X = 0$ correspond to the values of the crystal's quality factor and frequency when the cell was pumped as clean as possible at 5.239 K.

At all pressures greater than a few torr $X > R$, representing the effect of the enhanced density of the layers of helium close to the crystal, and $(X - R)$ is plotted in Figure 6.2. As the pressure of the helium gas rises from zero, $(X - R)$ increases and for $T >> T_c$ would smoothly attain an approximately constant value representing the adsorbed mass on the crystal in the liquid-like fluid at high pressure. However, $(T - T_c)$ is small and the high compressibility of the helium in the critical region under the van der Waals' forces of the crystal causes $(X - R)$ to deviate from this behaviour at a pressure as low as 1000 τ . $(X - R)$ then rises with pressure to peak at $\sim$ 1700 τ before falling sharply at $\sim$1800 τ to $(X - R) = 13$ kgm^{-2}s^{-1} , corresponding to the adsorbed effective mass in the liquid-like region.

The van der Waals' equation of state for the behaviour of a gas is

$$\left(P + \frac{a}{V^2}\right)(V - b) = K_b T \qquad (6.2.1)$$

where a and b are constants of the gas, representing the effects of intermolecular forces and the size of the molecules respectively. At the critical point, $(\partial P/\partial V)_T = 0$, $(\partial^2 P/\partial V^2)_T = 0$ and although the van der Waals' equation describes the behaviour of the system qualitatively, it takes no account of the effect of the large scale fluctuations

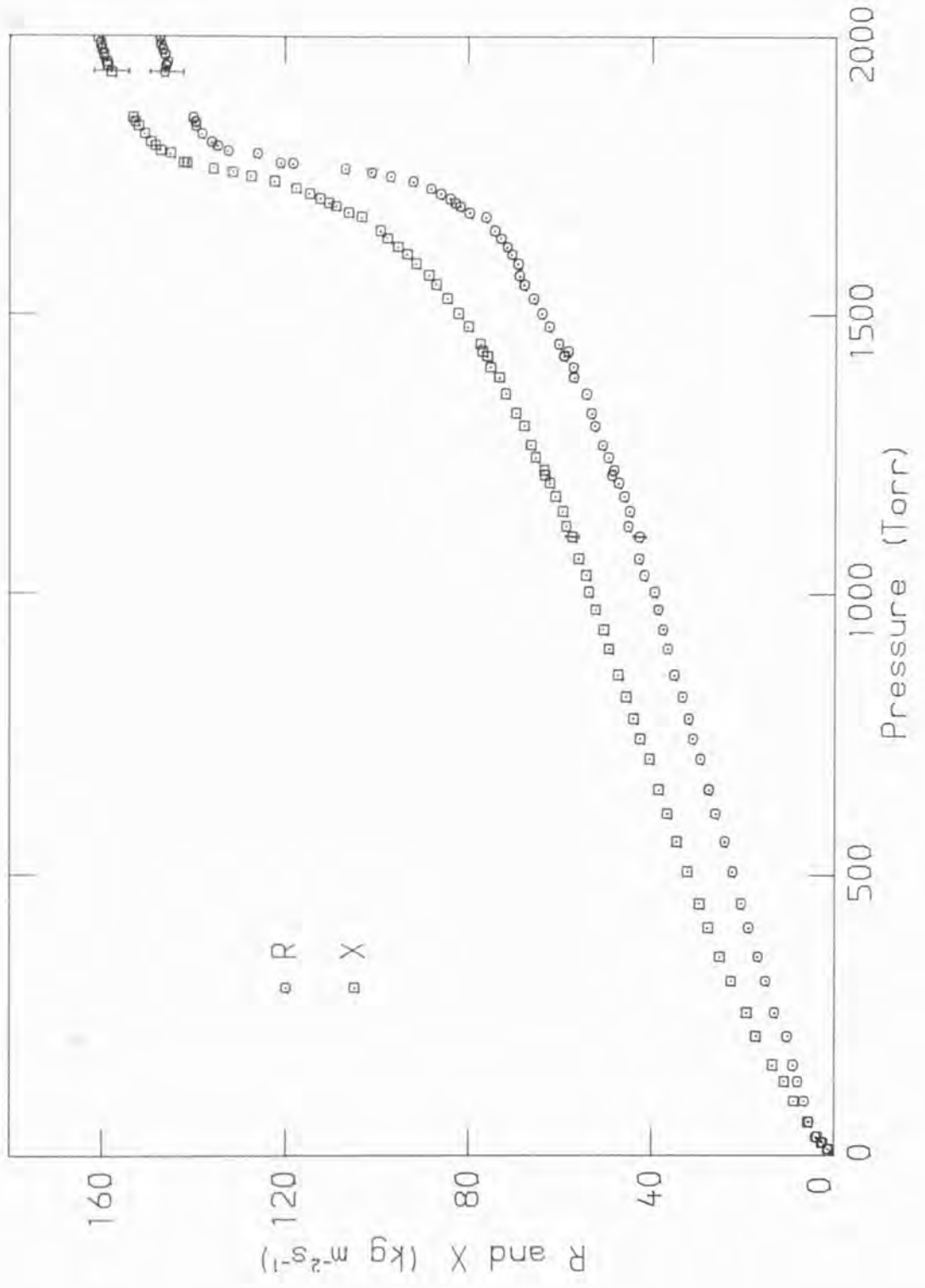

Figure 6.1

The real and imaginary parts, R and X , of the acoustic impedance as a function of pressure at 5.239 K .

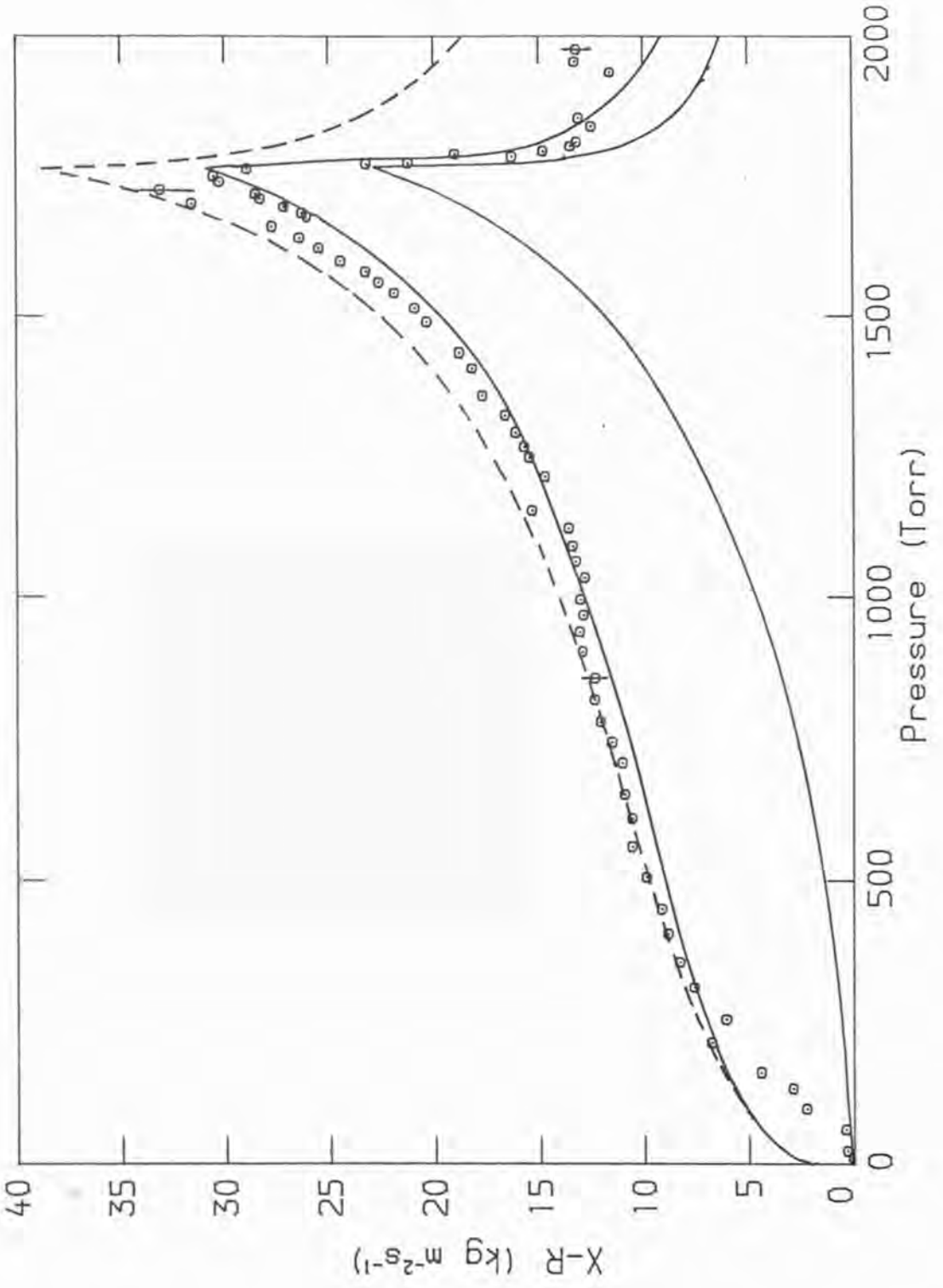

Figure 6.2

X-R for the data of Figure 6.1, showing the excess mass density adsorbed on the crystal for one (upper solid line) and two (lower solid line) adsorbed atomic layers, and for one layer including the effects of viscosity (dashed line).

in density that occur, and is therefore inadequate for a full description. The isothermal compressibility $K_T = 1/\rho \ (\partial\rho/\partial P)_T$ therefore diverges at the critical point as

$$K_T \propto (T - T_c)^{-\gamma} \quad \text{for} \quad \rho = \rho_c \ ; \ T > T_c \tag{6.2.2}$$

where the van der Waals' equation and other mean field theories predict $\gamma = 1$ and experimentally for ^4He, $\gamma = 1.17$ (Tominaga, 1974).

It is possible to estimate $\Delta X = X - R$ using the transmission line theory of Chapter 2. From equation (2.4.8), for a locally hydrodynamic viscous fluid

$$\frac{dZ(x)}{dx} = -i\omega\rho(x)\left[1 - \frac{Z^2(x)}{z^2(x)}\right] \tag{6.2.3}$$

where, as previously, $z(x) = (1 - i)\sqrt{\omega\rho(x)\eta(x)/2}$ is the local impedance and $Z(x)$ the actual impedance at x. If the increase in $Z(x)$ at the crystal surface is small, then

$$\frac{dZ(x)}{dx} = -i\omega\rho(x)\left[1 - \frac{Z^2(\infty)}{z^2(x)}\right] \tag{6.2.4}$$

where $Z(\infty) = (i - i)\sqrt{\omega\rho(\infty)\eta(\infty)/2}$ is the bulk impedance of the fluid, density $\rho(\infty)$ and viscosity $\eta(\infty)$. The change in impedance at the crystal surface due to the enhanced density helium close to its surface is therefore

$$\Delta Z = -i\omega \int_{x_0}^{\infty} \{\rho(x) - \frac{\eta(\infty)}{\eta(x)}\rho(\infty)\}dx \tag{6.2.5}$$

Hence, as previously, the main effect of the short range ($< \delta$) van der Waals forces is to increase X while R remains equal to the bulk value. If the viscosity is independent of density then the integral is equal to the excess mass density per unit area σ :

$$\Delta Z = -i\omega \int_{x_o}^{\infty} \{\rho(x) - \rho(\infty)\} dx \qquad (6.2.6)$$

where x_o is the position of the solid/helium boundary. Thus, if the density profile $\rho(x)$ of the helium is known, the change in impedance $\Delta Z = i\Delta X = i(X - R)$ due to the enhancement in density of the fluid can be found.

The local density $\rho(x) \equiv \rho(T,P)$, where P is the pressure at a distance x from the crystal at temperature T , is given by

$$\frac{1}{\rho(T,P)} = \frac{\partial V_c(T,P)}{\partial P} \qquad (6.2.7)$$

where V_c is the chemical potential of the helium. Following Oestereich and Stenschke (1977), equation (6.2.7) is integrated from the position of interest x to infinity, with the condition that the chemical potential is constant everywhere:

$$\int_{P(\infty)}^{P(x)} \frac{dP}{\rho(T,P)} = -V_c(x) \qquad (6.2.8)$$

$$= \frac{AK_b}{x^3}$$

where $P(\infty)$ is the pressure of the bulk helium and the van der Waals' potential of the substrate, $V(x) = -AK_b/x^3$ has been taken as the inverse cube form for ease of evaluation, with $A = 1.986$ K $(\text{nm})^3$. The density profile $\rho(x)$ of the fluid is therefore obtained by taking a distance x from the crystal and finding the unknown pressure $P(x)$ by numeri-

cally evaluating the integral, increasing the upper limit until the value of the left-hand-side of equation (6.2.8) equals the van der Waals' potential $V(x)$. The density $\rho(T,P)$ was found from the bulk helium equations of McCarty (1973). The density profiles $\rho(x)$ for bulk pressures of between 500 and 2000 τ are plotted in Figure 6.3 for $T = 5.239$ K . These show the effects of the van der Waals' forces of the crystal, when combined with the high compressibility of the helium at $\sim$1700 τ , in creating the rapid rise in density that for $T < T_c$ would have developed into a liquid-vapour interface.

Density profiles such as those in Figure 6.3 can be used to evaluate the integral in equation (6.2.6) to find the excess mass $\Delta\sigma$ adsorbed on the crystal, and hence $\Delta X = (X - R) = \omega\Delta\sigma$ for any bulk pressure. The integral was performed for both $x_o = 0.36$ nm and $x_o = 0.72$ nm , corresponding to one and two atomic layers localised on the crystal respectively, and ΔX thus calculated is shown in Figure 6.2. The agreement of the data with the calculation for $x_o = 0.36$ nm is good, showing that only the first atomic layer is tightly bound to the crystal, subsequent layers being fluid. At low pressures, the measured difference $(X - R)$ decreases more rapidly than expected since the helium enters the non-hydrodynamic region where X goes to zero faster than R .

If the viscosity of the helium is not independent of density, the full expression, equation (6.2.5), for the change in impedance due to the enhanced density layers must be used. It is therefore necessary to know $\eta(\rho)$ for densities up to the solidification pressure ($\sim$205 atm. at 5.239 K) . Unfortunately data for the viscosity is not available for this temperature over the complete density range, and following Ohbayashi and Ikushima (1974) must be estimated by assuming that the viscosity at a given density and temperature $\eta(\rho,T)$ may be written as the sum of temperature-only and density-only dependent terms

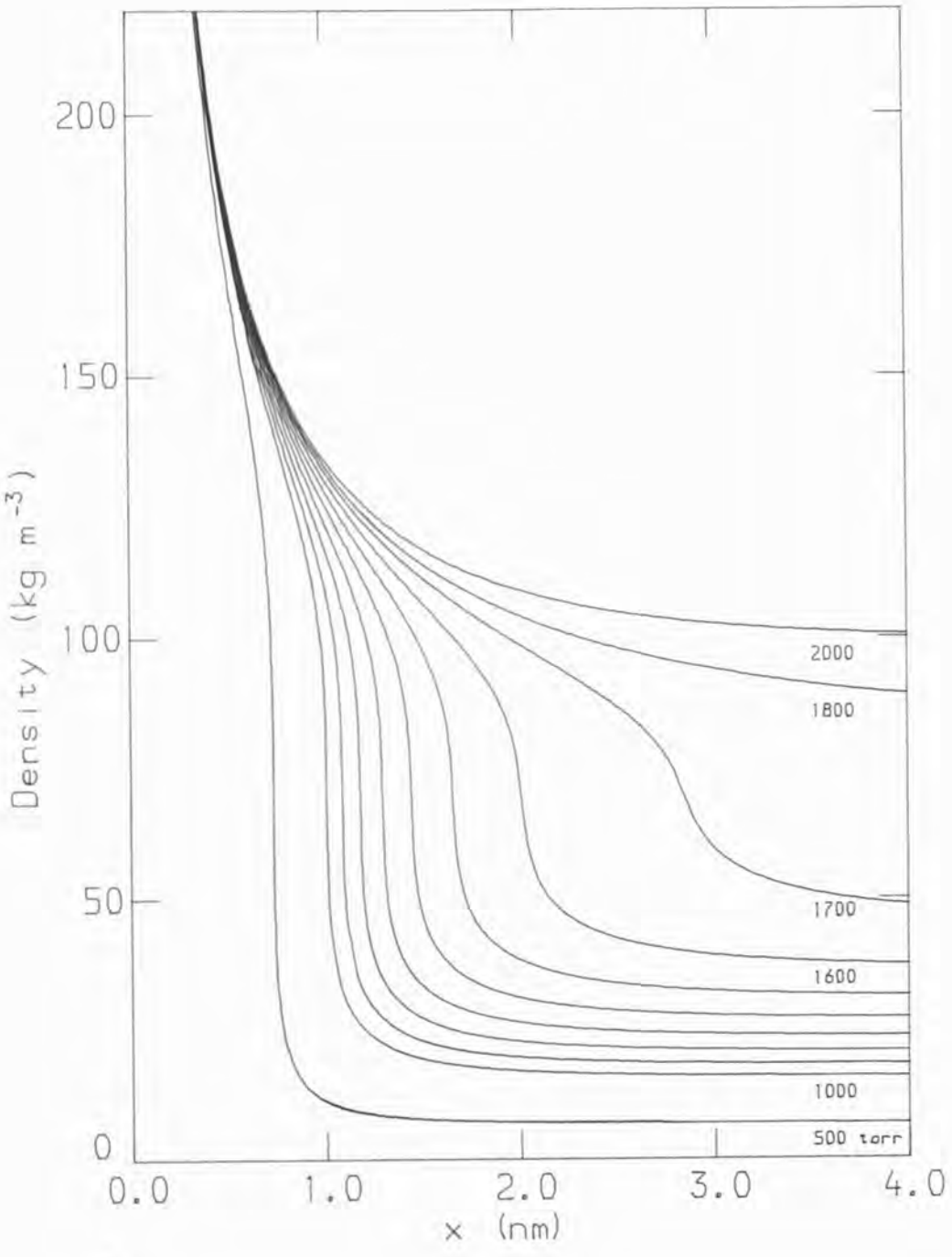

Figure 6.3

Density profile of the helium film on the crystal for various bulk pressures at 5.239 K .

$$\eta(\rho,T) = \eta(0,T) + \Delta\eta(\rho)$$

The zero density viscosity $\eta(0,T)$ is plotted in Figure 6.4 for low pressure data from Landolt-Börnstein (1969), and for 5.239 K $\eta(0,T) = 14 \pm 1$ μP , in fair agreement with $\eta(0) = 13.5$ μP from Betts (1976). $\Delta\eta(\rho) = \eta(\rho,T) - \eta(0,T)$ is plotted in Figure 6.5 for densities in the range 0-150 kgm^{-3} and temperatures of 4.2-500 K for data from Landolt and Börnstein (1969), and at higher densities 140-175 kgm^{-3} and temperatures of 2.5-4.2 K for data from Goodwin (1974). $\Delta\eta(\rho)$ is seen to be independent of temperature, despite the large amount of scatter in the data which has been compiled from many different sources. The fit to the data shown in Figure 6.5 is extrapolated to the density at the solidification pressure, though the exact form is not crucial since the second term in equation (6.2.5) becomes negligible at high densities: $\eta(\infty)\rho(\infty)/\eta(x)\rho(x) \ll 1$. $\eta(\rho)$ is then used to evaluate the integral in equation (6.2.5) for $x_o = 0.36$ nm . ΔX is shown in Figure 6.2 and is a relatively good fit to the data, the major source of discrepancy is probably due to errors in the estimation of the viscosity $\eta(\rho)$, and the use of the van der Waals' approximation of the surface potential $V \propto x^{-3}$.

In summary, at $T = 5.239$ K for $P < 2000$ τ , the first atomic layer of helium is localised on the crystal, producing a pressure independent frequency shift, $\Delta f \sim 6$ Hz . This is not represented in the data of Figures 6.1 and 6.2 since the crystal's quality factor Q and frequency f corresponding to $R = 0$ and $X = 0$ were obtained by pumping the cell as clean as possible at 5.239 K which is not sufficient to remove the localised layer (binding energy of ∿200 K (Ezell, Pollock and Daunt, 1981)). Subsequent layers give a pressure dependent contribution to the impedance which is purely imaginary and

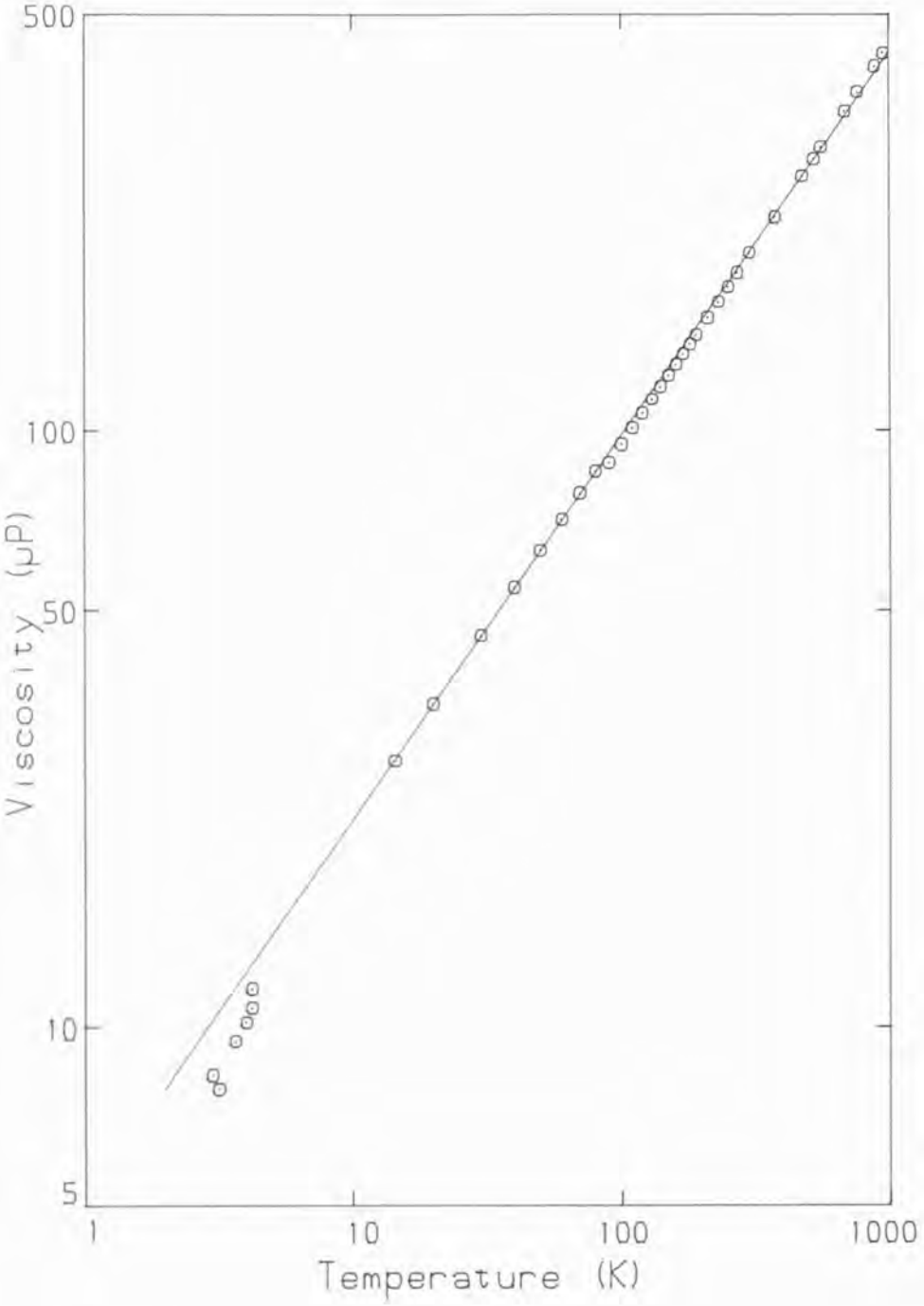

Figure 6.4

Temperature dependence of the low density viscosity of ^{4}He gas.

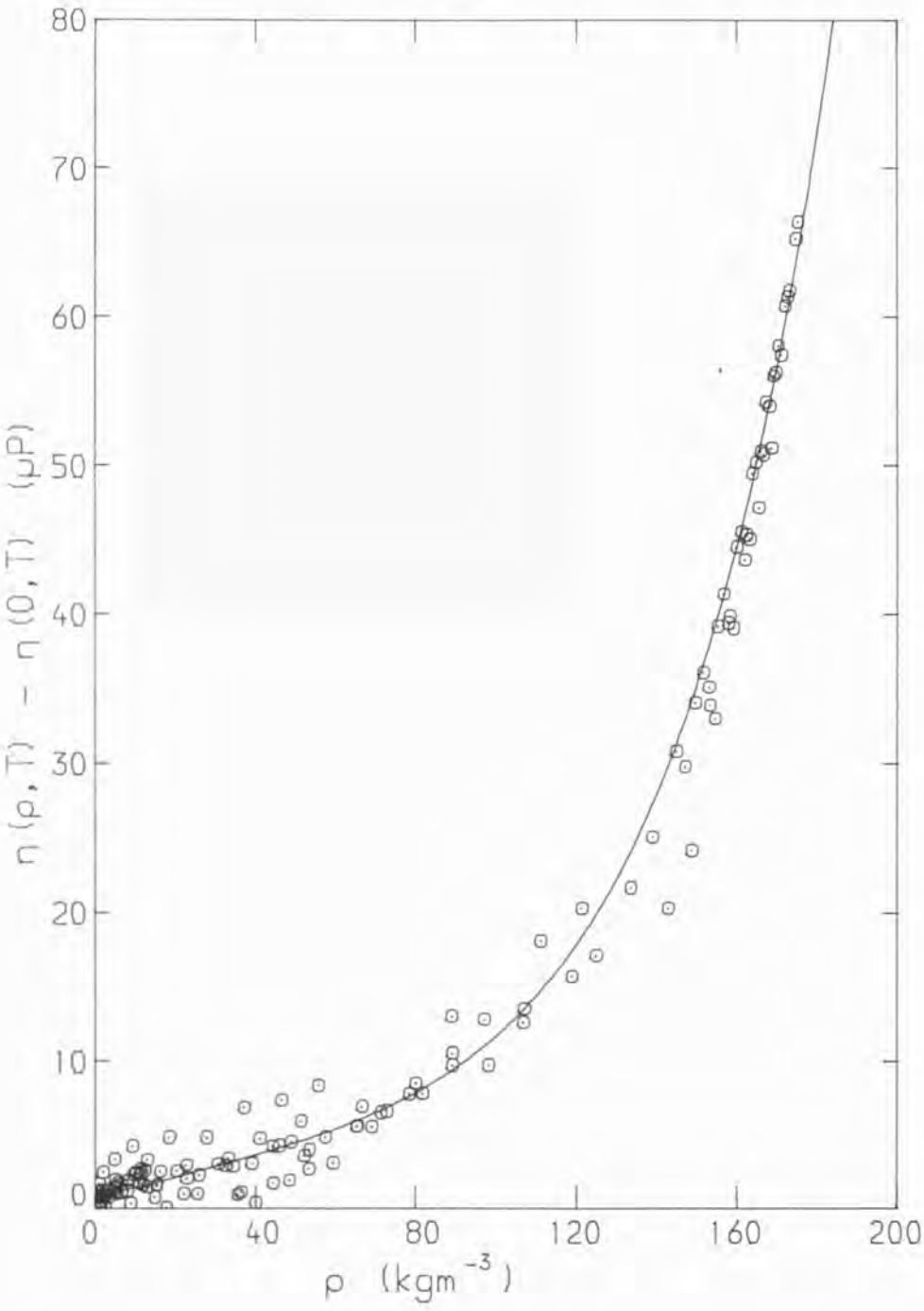

Figure 6.5

The density dependence of $\Delta\eta(\rho) = \eta(\rho,T) - \eta(0,T)$ for ^4He.

due to the enhancement of the density and hence also the viscosity of the helium above the bulk value.

6.3 The Viscosity at 5.239 K

6.3.1 The Viscosity in the Critical Region

The viscosity of the helium is found from equation (2.3.6) using the real part R of the impedance, since, as discussed in the previous section, this best represents the properties of the bulk fluid

$$\eta = \frac{R^2}{\pi \rho f} \tag{6.3.1}$$

The density ρ is found from the measured pressure P using the equation of state given by McCarty (1973) and the viscosity η is plotted against density in Figure 6.6. $\eta(\rho)$ increases from zero at zero pressure and for $\rho \gtrsim 20$ kgm^{-3} rises almost linearly with density. An extrapolation of this region back to $\rho = 0$ gives $\eta = 14 \pm 1$ μP, in good agreement with the value of the low pressure viscosity $\eta(0) = 13.5$ μP from Betts (1976). As $\rho \to 0$, the effective viscosity at 20 MHz decreases rapidly to zero as the gas enters the non-hydrodynamic regime.

Goodwin et al (1981) have measured the viscosity of helium in the critical region using a vibrating wire viscometer at a frequency of 4.5 kHz. For $\rho = 67$ kgm^{-3} and $\varepsilon = (T - T_c)/T_c \simeq 5 \times 10^{-3}$, they find $\eta = 24.8$ μP, lower than the value of (29 ± 2) μP for the data of Figure 6.6 at $\varepsilon = 9 \times 10^{-3}$.

In the hydrodynamic limit, $\omega = 0$, $q = 0$, the shear viscosity in the critical region can be expressed as the sum of a background part, η_o, and a critical part, η_c; (Swinney and Henry, 1973)

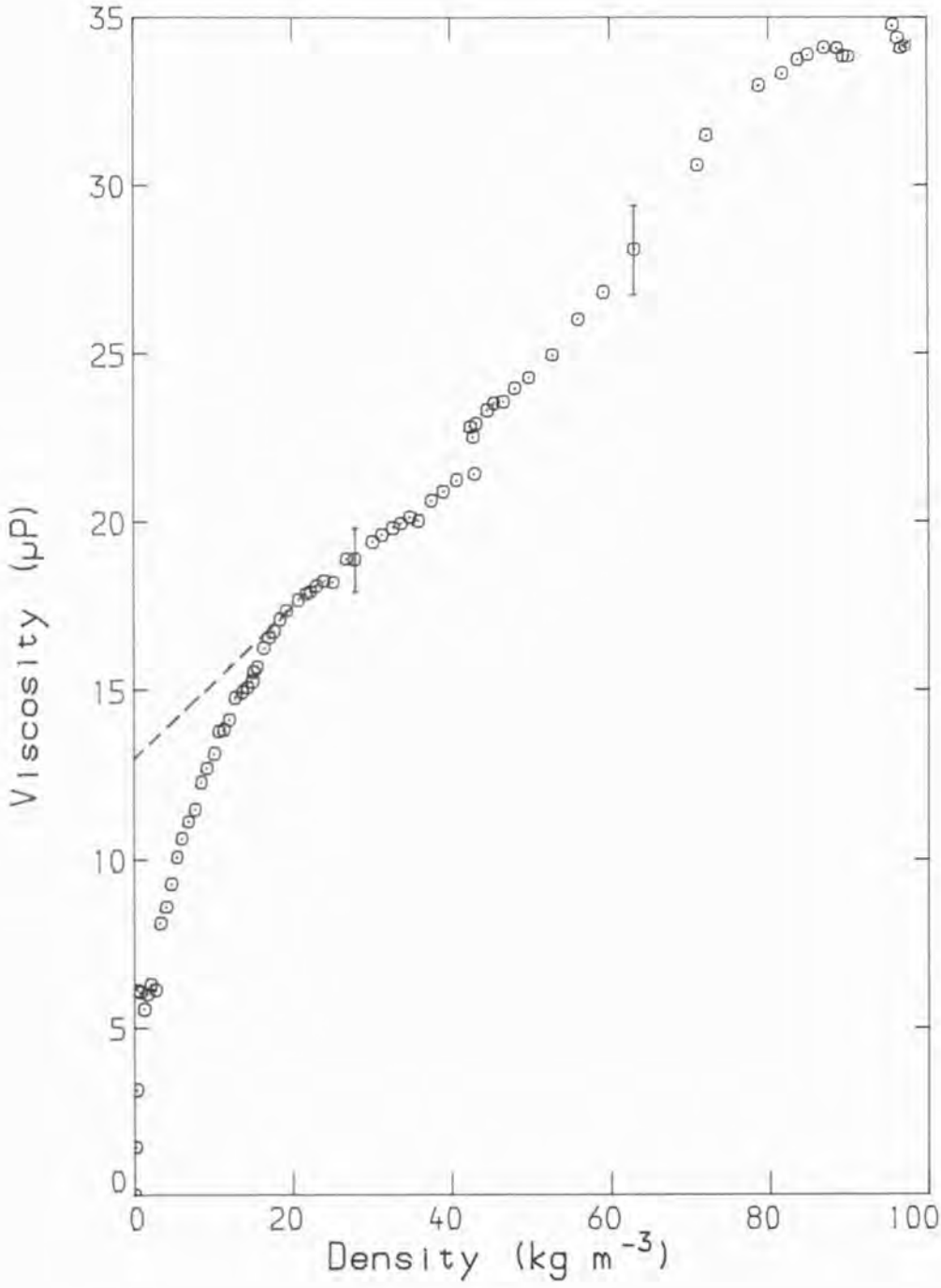

Figure 6.6

The effective viscosity of ^{4}He as a function of density at 5.239 K .

$$\eta(T) = \eta_o + \eta_c \tag{6.3.2}$$

where η_o is the value the viscosity would have in the absence of any critical anomaly. The critical part η_c may be written (Perl and Ferrell, 1972)

$$\eta_c \equiv \eta_c(\xi) = \frac{8}{15\pi^2}\,\eta_o\,\ell n(q_D\xi) \tag{6.3.3}$$

for not too large values of $(q_D\xi)$, where q_D is a Debye cutoff for the wavenumber and $\xi \propto \varepsilon^{-\nu}$ is the correlation length of the density fluctuations in the fluid. For some temperature ranges, therefore, the viscosity exhibits a logarithmic divergence, however it is expected to remain finite at the critical point with

$$\eta_c \propto \varepsilon^{\phi} \tag{5.3.4}$$

where $\phi = 0.036$ (Ohta, 1977).

In general the viscosity is both frequency and q-dependent, Kawasaki and Lo (1972) evaluate the non-local contributions to the shear viscosity and give

$$\eta_q = \eta(T)[1 - F(q\xi)] \tag{6.3.5}$$

Ohbayashi and Ikushima (1974) give the correlation length in helium at the gas-liquid critical point as $\xi = (3.6 \pm 0.8)\varepsilon^{-(0.54 \pm 0.05)}$ Å and hence at 5.239 K, $\xi = 4.5$ nm. Taking $q\xi \equiv 2\pi/\delta$, with $\delta = 24$ nm at the critical point, $q\xi = 1.2$, but $F(q\xi) = 0.02$ and the correction for non-local effects at 20 MHz is negligible.

Thus, for $(T - T_c) = 49$ mK , the impedance of the helium measured by the crystal will be unaffected by the weak divergence of the viscosity at the critical point in the hydrodynamic limit. Non-local effects arising from the finite penetration depth of the viscous wave are also expected to be small, while in contrast to what is observed, the high frequency of the measurements will tend to reduce the effective viscosity (Lo and Kawasaki, 1973).

The viscosity deduced from the real part R of the impedance at 20 MHz is thus 10-15% higher than might be expected. This may be attributed to errors in determining the density of the helium $\rho(T,P)$ to be used in equation (6.3.1). An 0.1% error in the measurement of the pressure in the critical region will result in a much larger error ($\sim 2\%$) in the density due to the characteristics of the isotherms; at T_c , $(\partial P/\partial \rho)_T = 0$. The divergence of the compressibility of a fluid at the critical point also means that in general, equations of state become inaccurate in the critical region; McCarty (1973) whose equation of state was used to find $\rho(T,P)$ estimates errors of 2% on average and 10% at maximum in calculating the density. In addition to the above effects, the helium in the cell is compressed under its own weight in the earth's gravitational field. This introduces density gradients into the fluid and the density of the helium in which the crystal is immersed is greater than the density represented by the pressure measured at the top of the cryostat.

6.3.2 The Effective Viscosity at Low Pressures

The effective viscosity of helium at 20 MHz decreases rapidly to zero for $\rho \lesssim 20$ kgm^{-3} rather than to the low pressure viscosity $\eta(0) = 13.5$ μP given by Betts (1976). The low density viscosity is

plotted in Figure 6.7 and its behaviour can be attributed to the increase in mean free path ℓ of the atoms at low pressures and the subsequent transition from the hydrodynamic to the non-hydrodynamic regime. Borovikov and Peshkov (1976) derived an expression which corrects the hydrodynamic impedance for finite values of ℓ/δ

$$Z = \frac{(1 - i)\eta/\delta}{1 + (1- i)\beta\ell/\delta} \qquad (6.3.6)$$

where η is the hydrodynamic viscosity and $\ell = \bar{c}\tau$, with τ being the collision time of the atoms and $\bar{c}$ their mean speed. The constant $\beta = (2 - \alpha)/\alpha$ enhances the effective value of the ratio ℓ/δ and arises from the possibility that a fraction $s = 1 - \alpha$ of atoms incident on the crystal surface may be specularly reflected from it.

This equation reduces to the correct expression in the hydrodynamic limit $\omega\tau < 1$ but strictly speaking is only valid as a correction to the hydrodynamic region for $\ell/\delta > 1$, $\omega\tau < 1$. However, if β is chosen to be $\beta = 4/3\alpha$, equation (6.3.6) has the correct form in both the hydrodynamic region and in the non-hydrodynamic limit, where

$$Z = R_\infty = \tfrac{1}{4}\alpha\rho\bar{c} \quad \text{for} \quad \ell/\delta >> 1\,,\ \omega\tau >> 1 \qquad (6.3.7)$$

and has been found (Lea, Fozooni and Retz, 1984) to give a good account of the transition between the two regions.

For an ideal gas $\ell/\delta = \sqrt{3\omega\tau/2}$ where $\tau = k\eta/P$, k being approximately unity, and the effective viscosity $\eta = R^2/\pi\rho f$ can be found from the real part R of equation (6.3.6). Figure 6.7 shows such calculations with $\beta = 4/3\alpha$ for $\alpha = 0.1$, 0.2 and 1.0. The best fit appears to be for $\alpha = 0.2$ (and hence $\beta = 6.67$), a value not inconsistent with that of $\alpha = 0.25$ found by Lea and Retz (1981)

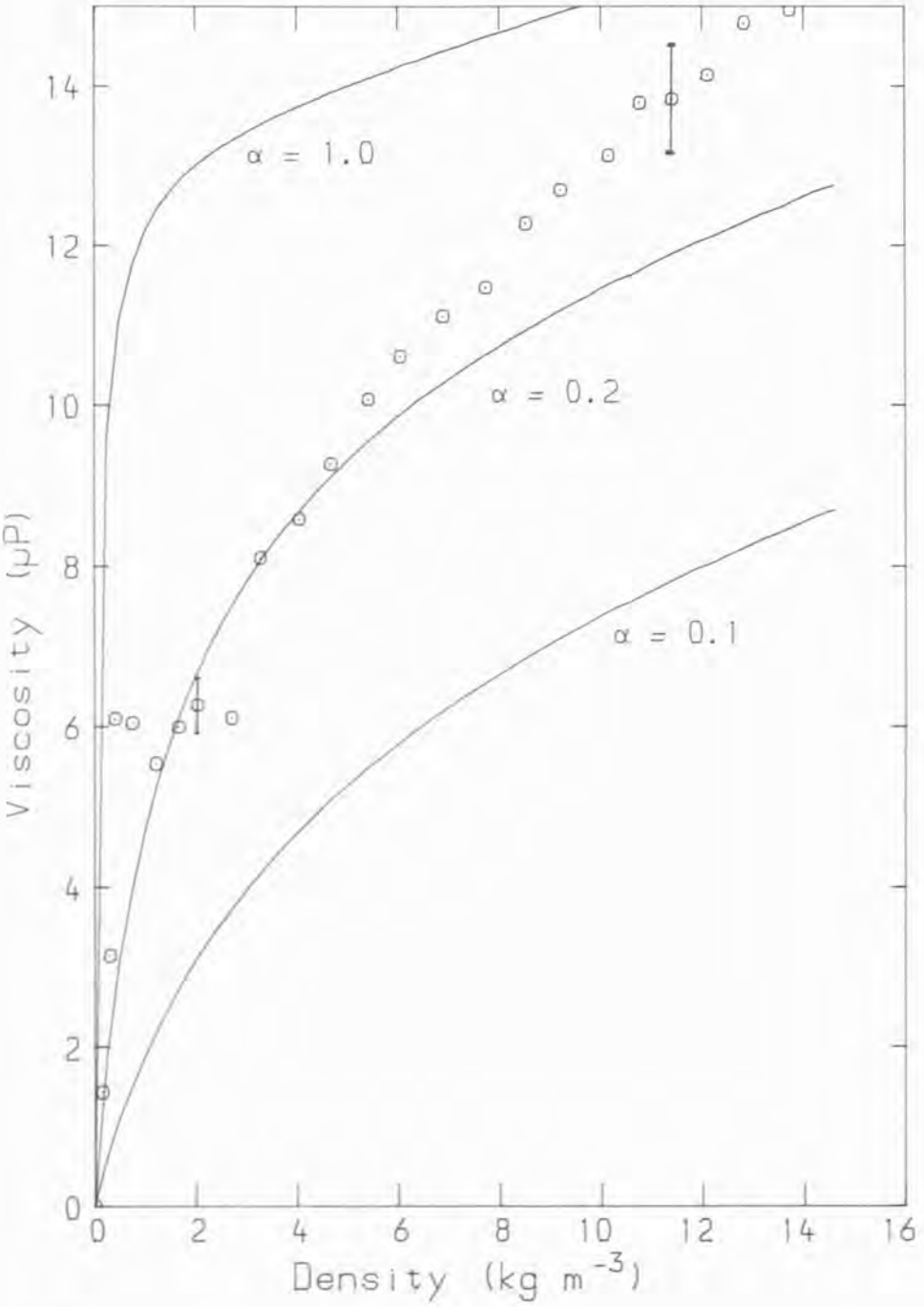

Figure 6.7

The effective viscosity of ^{4}He at low densities, showing the viscosity calculated for a diffusely scattered fraction α of 0.1, 0.2 and 1.0 .

for ^{3}He quasi-particles in superfluid ^{4}He below 0.1 k , implying that diffusive scattering is due to surface roughness. If β is taken as being $\beta = (2 - \alpha)/\alpha$ as found by Borovikov and Peshkov (1976) then $\alpha = 0.26$ and the difference between the two values of α is within the error bars of the data.

Jensen et al (1980) have shown that to a first approximation, for $\omega\tau < 1$,

$$Z = (1 - i)\eta/\delta[1 - (1 - i)\zeta/\delta + O(\omega\tau)]$$

$$\simeq \frac{(1 - i)\eta/\delta}{1 + (1 - i)\zeta/\delta} \qquad (6.3.8)$$

where ζ is the slip length. The length ζ arises from the slippage of a fluid relative to its solid boundary and represents that distance behind the surface at which the fluid's velocity extrapolates to zero. Maxwell's theory of slip (see e.g. Kennard (1938) p. 291) gives $\zeta \sim \ell$, the mean free path of the atoms, and for a fraction α of atoms diffusely scattered at the surface

$$\zeta = k\left(\frac{2 - \alpha}{\alpha}\right) \ell \qquad (6.3.9)$$

where $k \approx 1$. The factor $(2 - \alpha)/\alpha$ is the same as that Borovikov and Peshkov have derived, equation (6.3.6) with $\beta = (2 - \alpha)/\alpha$, directly from kinetic slip theory. Jensen et al (1980) calculated upper and lower bounds for the ratio ζ/ℓ from the Boltzmann equation; for a Maxwell-Boltzmann gas the exact result ($\omega = 0$) for totally diffusive scattering ($\alpha = 1$) is $\zeta/\ell = 1.126$ and therefore in general, for $\alpha < 1$

$$\frac{\zeta}{\ell} = 1.126 \left(\frac{2 - \alpha}{\alpha}\right)$$

using this expression to obtain an estimate of the diffusely scattered fraction gives $\alpha = 0.29$.

The three values of α derived above for the data of Figure 6.7 all arise from an equation of the form (6.3.6) which gives a correction to the hydrodynamic impedance $\omega\tau << 1$ for $\ell/\delta > 1$. Although not strictly valid for $\omega\tau > 1$, the equation can, through a suitable choice of β be made to have the correct impedance in both limiting regions, $\omega\tau << 1$ and $\omega\tau >> 1$, resulting in a value for α which is not unreasonable when compared with those obtained with β appropriate for only $\omega\tau < 1$, $\ell/\delta > 1$.

Chapter 7

Concluding Comments

An AT-cut quartz crystal resonator has been used to excite shear waves with a viscous penetration depth of around 20 nm in ^{4}He films adsorbed on the electrodes of the crystal. The complex transverse acoustic impedance of the film was found from changes in the quality factor and resonant frequency of the crystal, and the technique has been shown to be useful in investigating the properties of films with thickness comparable with the penetration depth.

The He I film has a thickness which may be controlled by the creation of small temperature differences between the crystal and bulk liquid helium below it, while the superfluid film where, except just below the λ-point, such temperature differences are difficult to create, has a constant thickness. In the hydrodynamic region, where $\omega\tau << 1$, we have shown that transmission line theory can be used to calculate the impedance of helium adsorbed on the crystal and to deduce the thickness of liquid films. We are hence able to show that helium completely wets the crystal's gold electrodes and recent suggestions of incomplete wetting of surfaces by helium (Migone et al, 1985) are therefore incorrect, at least for our crystals. Below 1.2 K, the helium film becomes non-hydrodynamic and in the limit $\omega\tau >> 1$ rotons cross the film ballistically. Those rotons incident upon the free surface outside the critical angle are specularly reflected and return to the crystal with unchanged transverse momentum. Within the critical angle a fraction estimated as 0.35 ± 0.03 were found to be not specularly reflected and are believed to cause the evaporation of an atom from the film surface. This value is in remarkably good

agreement with that of $\sim\frac{1}{3}$ given by Wyatt (1983) for the average probability of the quantum evaporation of a ^{4}He atom by thermal excitations and this implies that a transversely oscillating surface may be useful in detecting rotons in superfluid helium.

Above the liquid-gas critical point the density of the helium close to the crystal is enhanced above its bulk value, increasing rapidly but continuously up to the first layer of atoms which are localised on the crystal electrodes. The enhanced density layers cause a marked increase in the measured impedance, the major contribution being from the high density liquid comprising the second layer of atoms. At low pressures the ^{4}He gas becomes non-hydrodynamic and in the ballistic limit the impedance is found from kinetic theory, having no imaginary component and with a real part dependent on the fraction of atoms diffusely scattered from the crystal electrodes. This was found to be ~ 0.2 , a value comparable with that found for ^{3}He atoms in superfluid ^{4}He, implying that the scattering properties of the surface depends upon its roughness.

Finally, an unexpected feature of the superfluid film impedance measurements was the resonance observed at low temperatures. This is thought to be associated with the superfluid film itself rather than with the crystal and has been shown to be not inconsistant with the resonance at $\lambda/4$ of Kelvin waves on pinned vortices. In this case, it is possible to estimate the primordial vortex line density present on the crystal, though the value obtained is somewhat higher than might be expected. To confirm the presence of vortices, the possibility of the resonance being due to coupling between crystal vibrational modes must be eliminated by using a different cut of crystal for the resonantor. It may then prove possible to control the vortex line density by

changing the depth of the helium over the crystal as it passes through the λ-transition.

References

Andereck C.D. and Glaberson W.I., J. Low Temp. Phys., 48, 257 (1982).

Andronikashvili E.L. and Tsakadze D.S., Zh. Eksp. Teor. Fiz., 37, 322 (1959) [Sov. Phys. - JETP, 10, 227 (1960)].

Ashton R.A. and Glaberson W.I., Phys. Rev. Lett., 46, 1062 (1979).

Atkins K.R., 'Liquid Helium' (Cambridge University Press, 1959) p. 199.

Atkins K.R. and Rudnick I., in 'Progress in Low Temperature Physics' ed. Gorter C.J., (North Holland, Amsterdam, 1970) Vol. VI, Chap. 2, p. 37.

Awschalom D.D. and Schwarz K.W., Phys. Rev. Lett., 52, 49 (1984).

Bahadur H. and Parshad R. in Physical Acoustics, Vol. XVI, eds. Mason W.P. and Thurston R.N., (Academic Press, New York, 1982) p. 37.

Barenghi C.F., Donnelly R.J. and Vinen W.F., J. Low Temp. Phys., 52, 189 (1983).

Barenghi C.F., Donnelly R.J. and Vinen W.F., Phys. Fluids, 28, 498 (1985).

Batchelor G.K., 'An Introduction to Fluid Dynamics' (Cambridge, 1967).

Berlincourt D.A., Curran D.R. and Jaffe H., in Physical Acoustics, Vol. IA, eds. Mason W.P. and Thurston R.N. (Academic Press, New York, 1964) p. 169.

Bertinat M.P., Betts D.S., Brewer D.F. and Butterworth G.J., Phys. Rev. Lett., 28, 472 (1972).

Betts D.S., 'Refrigeration and Thermometry Below One Kelvin' (Sussex University Press, 1976).

Betts D.S., Cryogenics, 16 , 3 (1976).

Betts D.S., Keen B.E. and Wilks J., Proc. Roy. Soc., A289, 34 (1965).

Birch J., Proc. IEE, 112, 159 (1965).

Birch J. and Weston D.A., Proc. 30th Ann. Freq. Control Symposium (1976) p. 32.

Bishop D.J., Berthold J.E., Parpia J.M. and Reppy J.D., Phys. Rev., B24, 5047 (1981).

Bondarev V.N., Zh. Eksp. Teor. Fiz., 83, 2088 (1982) [Sov. Phys. - JETP, 56, 1211 (1982)].

Borovikov A.P. and Peshkov V.P., Zh. Eksp. Teor. Fiz., 70, 300 (1976) [Sov. Phys. - JETP, 43, 156 (1976)].

Brewer D.F., in 'The Physics of Liquid and Solid Helium', eds. Bennemann K.H. and Ketterson J.B. (Wiley, New York, 1978) Vol II, Chap. 6, p. 573.

Brewer D.F., Symonds A.J. and Thompson A.L., Phys. Rev. Lett., 15, 182 (1965).

Casimir H.B.G. and Polder D., Phys. Rev., 73, 360 (1948).

Chester M., Webster G.D., Webster E. and Oestereich T., Phys. Rev. Lett., 45, 464 (1980).

Chester M. and Yang L.C., Phys. Rev. Lett., 31, 1377 (1973).

Chester M., Yang L.C. and Stephens J.B., Phys. Rev. Lett., 29, 211 (1972).

Dzyaloshinskii I.E., Lifshitz E.M. and Pitaevskii, Advances in Physics, 10, 165 (1961).

Ezell E.F., Pollock F. and Daunt J.G., J. Low Temp. Phys., 42, 47 (1981).

Fetter A.L., in 'The Physics of Liquid and Solid Helium', eds. Bennemann K.M., and Ketterson J.B. (Wiley, New York, 1978) Vol. I, Chap. 3, p. 207.

Fetter A.L. and Harvey K., Phys. Rev., A4, 2305 (1971).

Feynman R.P., in 'Progress in Low Temperature Physics', ed. Gorter C.J. (North Holland, Amsterdam, 1955) Vol. I, p. 17.

Firth D., Quartz Crystal Oscillator Circuit Design Handbook, Dept. of the U.S. Army, Project No. 3A99-15-004 (1965).

Forder R.W., Halse M.R. and Brown J.B., Proc. 14th Int. Conf. on Low Temp. Phys., ed. Krusius and Vuorio, Vol. I, p. 396 (1975).

Glaberson W.I., Physica, 109-110B, 1567 (1982).

Glaberson W.I. and Donnelly R.J., Phys. Rev., 141, 208 (1966).

Goodwin J.M., Physica, 76, 177 (1974).

Goodwin J.M., Hirai A., Mizusaki T., Tsuboi K. and Waldschmidt T.K., Physica, 107B, 351 (1981).

Hall H.E., Proc. Roy. Soc., A245, 546 (1958).

Hall H.E., Advances in Physics, 9, 89 (1960).

Hedge S.G. and Glaberson W.I., Phys. Rev. Lett., 45, 190 (1980).

Hemming D., Can. J. of Physics, 49, 2621 (1971).

Herb J.A. and Dash J.G., Phys. Rev. Lett., 35, 171 (1975).

Jensen H.H., Smith H., Wölfe P. and Nagal K., J. of Low Temp. Phys., 41, 473 (1980).

Kawasaki K. and Lo S-M., Phys. Rev. Lett., 29, 48 (1972).

Kennard E.M., 'Kinetic Theory of Gases', (McGraw-Hill, New York, 1938).

Khalatnikov I.M., in 'The Physics of Liquid and Solid Helium', eds. Bennemann K.H. and Ketterson J.B. (Wiley, New York, 1976), Vol. I, Chap. 1, p. 1.

Kierstead H.A., Phys. Rev., A3, 329 (1971).

Komiyama B., Proc. 35th Ann. Freq. Control Symposium (1981) p. 335.

Landau L.D. and Lifshitz E.M., 'Fluid Mechanics', (Pergamon Press, London, 1959).

Landolt-Börnstein Zahlenwerte und Funktioner aus Physik, Chemie, Astronomie, Geophysik und Technik, 6th edition (Springer Verlag, Berlin, 1969) Vol. 11, p. 13.

Lea M.J. and Fozooni P., J. Low Temp. Phys., 56, 25 (1984).

Lea M.J. and Fozooni P., Ultrasonics, 23, 133 (1985).

Lea M.J. and Fozooni P., J. of Low Temp. Phys., 62, 55 (1986).

Lea M.J., Fozooni P. and Retz P.W., J. of Low Temp. Phys., 54, 303 (1984).

Lea M.J. and Retz P.W., Physica, 107B, 225 (1981).

Lifshitz E.M., Zh. Eksp. Teor. Fiz., 29, 94 (1955) [Sov. Phys. – JETP, 2, 73 (1956)].

Lo S-M. and Kawasaki K., Phys. Rev., A8, 2176 (1973).

Lu C., in 'Applications of Piezoelectric Quartz Crystal Microbalances', eds. Lu C. and Czanderna A.W., (Elsevier, Amsterdam, 1984), Chap. 2, p. 19.

Mason W.P., Bell System Technical Journal, 19, 43 (1940).

McCarty R.D., J. Phys. Chem. Ref. Data, 2, 923 (1973).

Migone A.D., Krim J. and Dash J.G., Phys. Rev., B31, 7643 (1985).

Monchick L., Mason E.A., Munn R.J. and Smith R.J., Phys. Rev., 139, A1076 (1965).

Mossuz G. and Gagnepain J.J., Cryogenics, 16, 652 (1976).

Nadirashvili Z.S. and Tsakadze D.S., Sov. Phys. - JETP, 27, 24 (1968).

Oestereich T. and Stenschke H., Phys. Rev., B16, 1996 (1977).

Ohbayashi K. and Ikushima A., J. of Low Temp. Phys., 15, 33 (1974).

Ohta T., J. Phys. C., 10, 791 (1977).

Osborne D.V., Proc. Phys. Soc., A63, 909 (1950).

Perl R. and Ferrell R.A., Phys. Rev., A6, 2358 (1972).

Putterman S.J., 'Superfluid Hydrodynamics' (North Holland, Amsterdam 1974).

Retz P.W., 'Quartz Crystal Resonator Studies in He II', Ph.D. Thesis, University of London (1983).

Roach P.R. and Ketterson J.B., J. of Low Temp. Phys., 25, 637 (1976).

Roach P.R. and Ketterson J.B., Phys. Rev. Lett., 36, 736 (1976).

Rose-Innes A.C., 'Low Temperature Laboratory Techniques', (English Universities Press, London, 1973).

Sabisky E.S. and Anderson C.H., Phys. Rev., A7, 790 (1973).

Schwarz K.W., Phys. Rev., B31, 5782 (1985).

Spencer D.S., Lea M.J. and Fozooni P., Phys. Lett., 109A, 295 (1985).

Stockbridge C.D., in 'Vacuum Microbalance Techniques', ed. Behrndt K.H., (Plenum, New York, 1966) Vol. 5, pp. 147-205.

Swinney H.L. and Henry D.L., Phys. Rev., A8, 2586 (1973).

Thomson Sir William, Philosophical Magazine, 10, 155 (1880).

Thomlinson W., Tarvin J.A. and Passell L., Phys. Rev. Lett., 44, 266 (1980).

Tominaga A., J. of Low Temp. Phys., 16, 571 (1974).

Vinen W.F., in 'Progress in Low Temperature Physics' ed. Gorter C.J., (North Holland, Amsterdam, 1961) Chap. 1, p. 1.

Webster E., Chester M., Webster G.D.L. and Chestereich T., Phys. Rev., B22, 5186 (1980).

Webster E., Webster G. and Chester M., Phys. Rev. Lett., 42, 243 (1979).

Welber B., Phys. Rev., 119, 1816 (1960).

Werner J.F. and Dyer A.J., Proc. 30th Ann. Freq. Control Symposium, (1976) p. 40.

Wilks J., 'The Properties of Liquid and Solid Helium' (Clarendon Press, Oxford, 1967).

Wyatt A.F.G., Physica, 126B, 392 (1984).

Yang L.C., 'Quartz Microbalance Studies on Unsaturated Helium Films', Ph.D. Thesis, Univ. of California, Los Angeles (1973).

Yang L.C. and Mason P.V., Cryogenics, 20, 91 (1980).

Yarmchuk E.J. and Glaberson W.I., Phys. Rev. Lett., 41, 564 (1978).

Appendix 1

Addresses of the devices interfaced to the HP9816 microcomputer

700 - disc drive

701 - printer

702 - Marconi 2018 signal generator

704 - AKB-1

707 - AKB-2

716 - Keithley 195A multimeter

Command codes for the AKB-1

ASCII	Function
@	Pip Tone
A	Start Motor
B	Stop Motor
C	Motor UP
D	Motor DOWN
E	Half Steps
F	Full Steps
G	Auxilliary ON - ON if frequency is to be read
H	Auxilliary OFF
I	Disable Druck (on manual)
J	Enable Druck (on auto)
K	Single Shot Pulse
L	Druck Range 0
M	Druck Range 1
N	Druck Range 2
O	Druck Range 3

ASCII	Function
P	PRF Single Steps
Q	PRF 0.1 steps/second
R	PRF 0.2 steps/second
S	PRF 0.5 steps/second
T	PRF 1 steps/second
U	PRF 2 steps/second
V	PRF 5 steps/second
W	PRF 10 steps/second
X	PRF 20 steps/second
Y	PRF 50 steps/second
Z	PRF 100 steps/second
0	Aux. Relay 1 (motor) ON
1	Aux. Relay 1 (motor) OFF
2	Aux. Relay 2 ON
3	Aux. Relay 2 OFF (reset)
4	Aux. Relay 3 ON
5	Aux. Relay 3 OFF (reset)
6	Aux. Relay 4 ON
7	Aux. Relay 4 OFF (reset)

Command Codes for the AKB-2

These codes must be prefaced by the letter 'A' to access the interface board appropriate to the AVS-45 resistance bridge.

ASCII	Function
H	Excitation Range UP
I	Excitation Range DOWN
J	Resistance Range UP
K	Resistance Range DOWN

ASCII	Function
P	Multiplexer: position 0
Q	Multiplexer: position 1
R	Multiplexer: position 2
S	Multiplexer: position 3
T	Multiplexer: position 4
U	Multiplexer: position 5
V	Multiplexer: position 6
W	Multiplexer: position 7

e.g. The command

```
OUTPUT 707; "ARKI"
```

will select the resistance on the second multiplexer position and decrease both the resistance and excitation ranges.

Appendix II

LT-17 (Contributed Papers)
U. Eckern, A. Schmid, W. Weber, H. Wühl (eds)

THE TRANSVERSE ACOUSTIC IMPEDANCE OF ^{4}He ABOVE THE CRITICAL TEMPERATURE

M.J. LEA, D.S. SPENCER and P. FOZOONI

Department of Physics, Bedford College, University of London, Regent's Park, London NW1 4NS, U.K.

Measurements of the transverse acoustic impedance of ^{4}He at 20.5 MHz were used to obtain the viscosity from 0 to 2.7 bar at 5.239 K ($\varepsilon = (T-T_c)/T_c = 10^{-2}$). The results show the transition to non-hydrodynamic behaviour at low pressures and the effects of van der Waals forces in producing density gradients in the critical region.

We present here measurements of the transverse acoustic impedance $Z = R - iX$ of fluid ^{4}He just above the critical temperature T_c at pressures P up to 2.7 bar. The impedance was measured using a quartz crystal resonator as in previous work (1,2). The helium reduces the resonant frequency $f(=\omega/2\pi)$ and the quality factor Q of the loaded resonator from their values at $P=0$. R and X can then be found from

$$R = \tfrac{1}{2}\pi n R_q [Q^{-1}(P) - Q^{-1}(0)]$$
$$X = \tfrac{1}{2}\pi n R_q [f(0) - f(P)]/f(0) \qquad (1)$$

where n is the harmonic number of the resonance and R_q is the acoustic impedance of the quartz. The resonant frequencies were corrected for the small linear pressure dependence of the parameters of the quartz crystal itself. Measurements were made at the third harmonic at a frequency of 20.5 MHz. The temperature was stabilised to ±0.001 K at 5.239 K, 49 mK above the critical temperature at 5.190 K (on the T_{58} scale). The results for $R(P)$ and $X(P)$ are shown in Fig. 1. Note the rapid increase in R and X near the critical region and that $X > R$ at all pressures.

The transverse acoustic impedance of a hydrodynamic viscous fluid is

$$Z = R - iX = (1-i)(\pi f \eta/\rho)^{\frac{1}{2}} \qquad (2)$$

where η is the viscosity and ρ is the density. We have used the equation of state for $\rho(T,P)$ given by McCarty (3) to derive an effective viscosity

$$\eta' = R^2/\pi\rho f \qquad (3)$$

from the data in Fig. 1, and η' is plotted as a function of density in Fig. 2. For $\rho > 20$ kg m^{-3} $\eta'(\rho)$ increases almost linearly with density and an extrapolation back to $\rho=0$ gives a value $\eta'(0) = 13.5 \pm 1.0$ μP. This is in good agreement with the low density limit from Betts (4) of 13.55 μP at 5.239 K.. As $\rho \to 0$ the effective viscosity at 20.5 MHz decreases rapidly to zero, rather than a finite value, because of the transition to the non-hydrodynamic regime ($\omega\tau > 1$) as the collision time τ increases. From the kinetic theory of an ideal gas $\tau = K\eta/P$ where K is a factor close to unity. Thus $\omega\tau = 0.02$ at 20.5 MHz at a pressure of 0.1 bar. We have found previously (1) that the equation

$$Z = \frac{(1-i)(\eta\rho\pi f)^{\frac{1}{2}}}{1 + (1-i)\beta\ell/\delta} \qquad (4)$$

gives a good account of the transition from hydrodynamic to non-hydrodynamic behaviour, where $\ell = v\tau$ is the mean free path of the atoms with mean speed v, $\delta = (\eta/\rho\pi f)^{\frac{1}{2}}$ is the viscous penetration depth and η is the hydrodynamic viscosity. For an ideal gas $\ell/\delta = (3\omega\tau/2)^{\frac{1}{2}}$. If $\beta = 4/3\alpha$ then eq.(4) gives the correct limits for Z in both the hydrodynamic ($\omega\tau \ll 1$) and ballistic ($\omega\tau \gg 1$) regimes. The fraction of atoms which are diffusely scattered at the surface of the resonator, α, is the only free parameter. We have calculated the effective

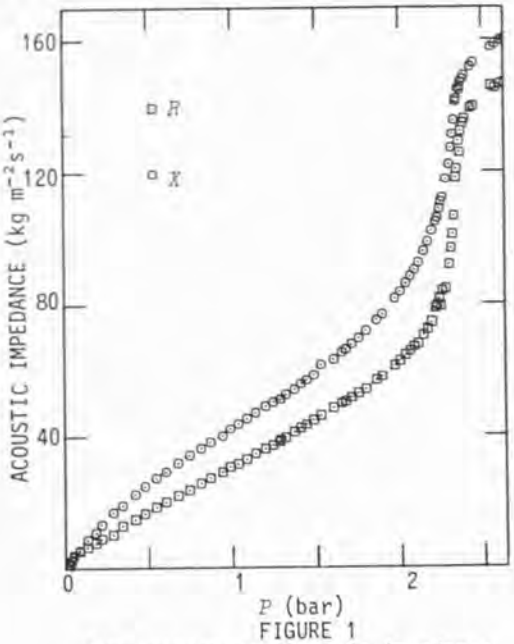

FIGURE 1
The transverse acoustic impedance $Z=R-iX$ of ^{4}He at 5.239 K

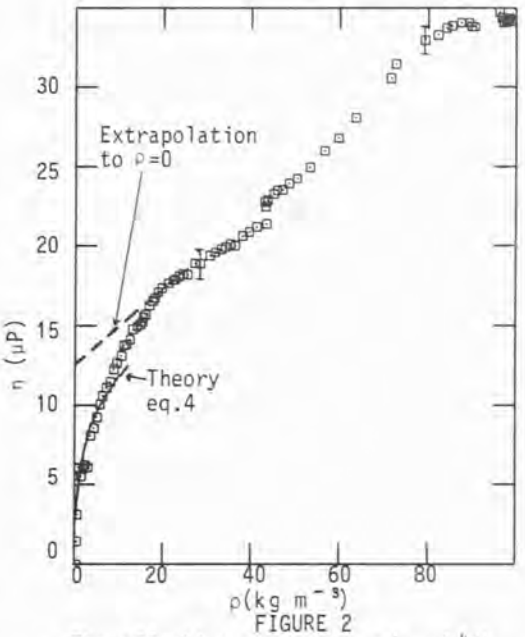

FIGURE 2
The effective viscosity, η', of ^4He

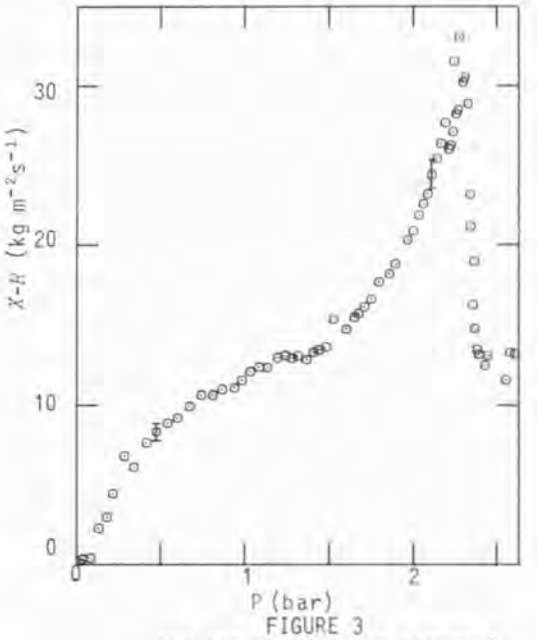

FIGURE 3
X-R for the data in Figure 1

viscosity η' at 20.5 MHz as shown in Fig. 2 for α = 0.2 which gives the best fit. This value is similar to that found for ^3He quasiparticles in superfluid ^4He below 0.1 K (2) and this suggests that the diffuse scattering is due to surface roughness.

Another region of interest is near the critical point (P_c = 2.274 bar). Goodwin et al. (5) measured η with a vibrating wire viscometer at 4.5 kHz and obtained a value of 24.8 μP for ρ=67 kg m^{-3} at $\varepsilon = (T-T_c)/T_c = 10^{-2}$. For $\varepsilon<10^{-2}$ they found a small critical anomaly in η along a near-critical isochore. Our value for η' at this density is 29±2 μP at $\varepsilon=0.94\times10^{-2}$ where the increase due to the critical point should be small. We are now investigating the critical anomaly in η at 20.5 MHz for $\varepsilon<10^{-2}$. Non-local effects may be important since Lo and Kawasaki (6) have shown that for a wavenumber q the effective viscosity is

$$\eta_q = \eta(T)(1-F(q\xi)) \qquad (5)$$

where ξ is the correlation length. For our experiment $q \cong 2\pi/\delta$ where $\delta \cong 24$ nm near the critical point. At $\varepsilon = 10^{-2}$, $q\xi \cong 1$ but $F(q\xi)$ is only 0.02 and the correction is negligible.

Also van der Waals forces will increase the density and viscosity of the fluid close to the crystal resonator. If the fluid at a distance x from the crystal is locally hydrodynamic then the change in acoustic impedance ΔZ is given by (1)

$$\Delta Z = -i\omega \int_0^\infty [\rho(x) - \rho(\infty)\eta(\infty)/\eta(x)]dx \qquad (6)$$

if $\Delta Z \ll Z$ and if the range of the forces $\ll\delta$. Thus van der Waals forces increase X, but not R, and X-R, as plotted in Fig.3, is a measure of the excess density and viscosity close to the crystal. As the pressure is increased, X-R exhibits a large critical anomaly where $(\partial\rho/\partial P)$ is large. This effect shows again that weak forces, such as gravity or van der Waals forces, can produce significant inhomogeneities near the critical point of a fluid.

ACKNOWLEDGEMENTS

We would like to thank Professor E.R. Dobbs for his encouragement and support; A.K. Betts, F. Greenough, F.W. Grimes and A. King for technical assistance and the SERC (UK) for a Research Grant and a Studentship (for D.S.S.).

REFERENCES

(1) M.J. Lea, P. Fozooni and P.W. Retz, J.Low Temp.Phys. 54 (1984) 303.
(2) M.J. Lea and P.W. Retz, Physica 107B (1981) 225.
(3) R.D. McCarty, J.Phys.Chem. Ref. Data 2 (1973) 923.
(4) D.S. Betts, Cryogenics 16 (1976) 3.
(5) J.M. Goodwin, A. Harai, T. Mizusaki, K. Tsuboi and T.K. Waldschmidt, Physica 107B (1981) 351.
(6) S-M. Lo and K. Kawasaki, Phys.Rev.Lett. 29 (1972) 48.

THE OBSERVATION OF VISCOUS WAVES IN A He I FILM

D.S. SPENCER, M.J. LEA and P. FOZOONI

Department of Physics, Bedford College, University of London, Regent's Park, London NW1 4NS, UK

Received 14 January 1985; revised manuscript received 18 March 1985; accepted for publication 29 March 1985

The transverse acoustic impedance of a ^{4}He film has been measured at 3.11 K and 20.5 MHz and shows the occurrence of standing shear waves in the film. This is in good agreement with calculations using transmission line theory and gives a new method of measuring the thickness of liquid films.

In fluids, the transverse mode of sound propagation is a heavily damped viscous wave. Measurements of the transverse acoustic impedance, $Z = R - iX$ therefore provide a useful probe of the fluid's properties on a length scale comparable with the penetration depth of the wave ($\delta \approx 20$ nm in liquid ^{4}He). Recently, measurements of Z have been made for bulk liquid ^{4}He [1,2], liquid ^{3}He [3] and for liquid ^{3}He–^{4}He mixtures [4].

We present here measurements of the transverse acoustic impedance at 20.5 MHz for films of ^{4}He above the λ-point. The impedance was found from changes in the quality factor Q and resonant frequency f of a quartz crystal resonator vibrating in shear and covered with the helium film. The effect of the helium is to decrease the Q and resonant frequency of the crystal by [1]

$$\Delta(Q^{-1}) = 4R/n\pi R_q\,, \tag{1}$$

$$\Delta f = -4f^2\sigma/nR_q - 2fX/n\pi R_q\,, \tag{2}$$

where n is the harmonic number of the resonance, R_q ($\gg R, X$) is the acoustic impedance of the quartz, σ is the adsorbed solid mass per unit area, and R and X are the real and imaginary parts of the impedance of the liquid film.

The profile of the helium film on the crystal is shown in fig. 1. Van der Waals forces cause a localised atomic layer to be adsorbed on to the crystal, giving, by the first term of eq. (2), a temperature independent frequency shift relative to the vacuum resonant frequency. The van der Waals forces also enhance the density of the liquid close to the crystal; since the density enhanced region is small, this too produces a shift in the crystal's resonant frequency with negligible effect on Q [1]. As the thickness of the film, a, is increased from $a = 0$, this mass loading effect is essen-

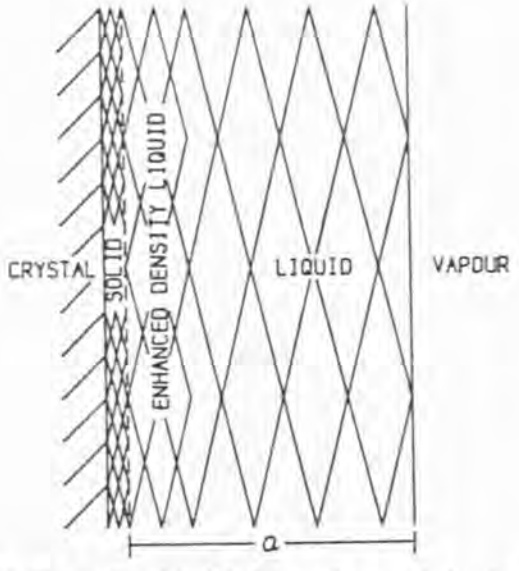

Fig. 1. The profile of the ^{4}He film on the crystal, showing the localised atomic layer and the region of enhanced density liquid caused by van der Waals forces. a is the thickness of the liquid film.

0.375-9601/85/$ 03.30 © Elsevier Science Publishers B.V. (North-Holland Physics Publishing Division)

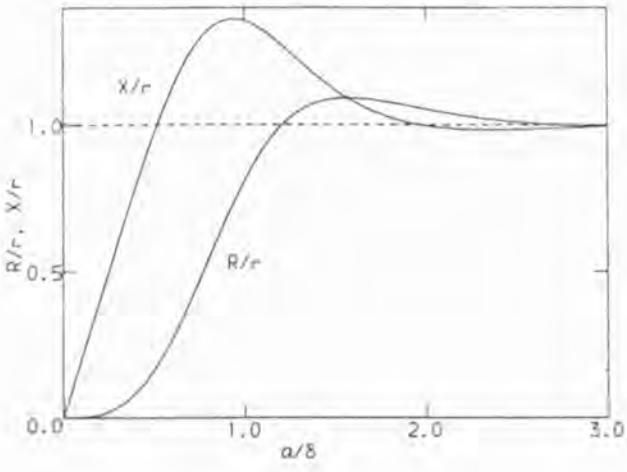

tially complete before the viscous losses of the film, given by eq. (1) and the second term of eq. (2), decrease both f and Q. The film has the properties of the bulk liquid and has its free surface in contact with ^{4}He vapour with an impedance Z_v.

For a homogeneous bulk fluid,

$$Z = (1 - \mathrm{i})(\eta\rho\omega/2)^{1/2} = (1 - \mathrm{i})r\,, \qquad (3)$$

with penetration depth $\delta = (2\eta/\rho\omega)^{1/2}$, where η is the viscosity, ρ is the density and $\omega = 2\pi f$. For a film

◀ Fig. 2. The real and imaginary parts of the acoustic impedance of a helium film, thickness a, in a vacuum. The bulk liquid has an impedance $(1 - \mathrm{i})r$ and δ is the penetration depth.

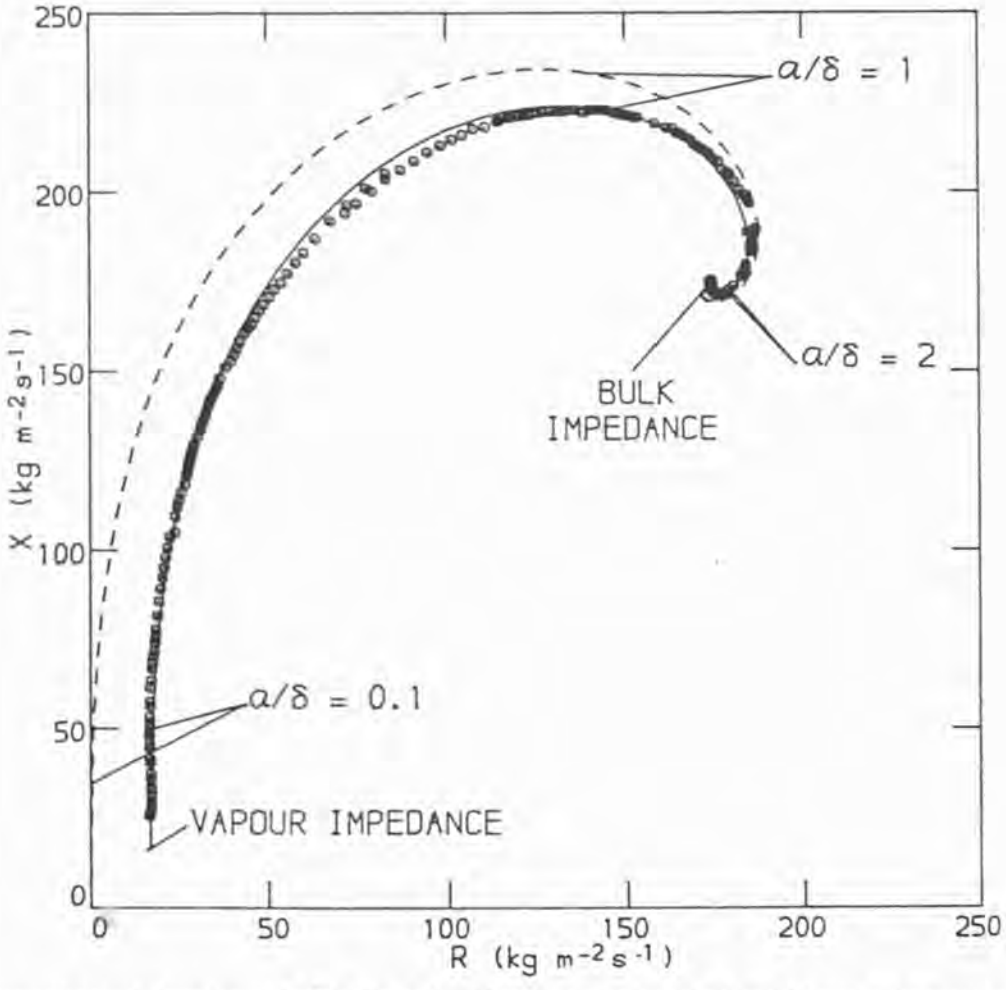

Fig. 3. The measured acoustic impedance of a ^{4}He film at 3.11 K as a/δ, the ratio of the film thickness to the penetration depth, is changed. The curve calculated from transmission line theory, eq. (4), is shown for films of bulk impedance 172 kg m^{-2} s^{-1} with a vapour impedance of zero (dashed line) and of 16 kg m^{-2} s^{-1} (solid line).

of thickness a, from analogy with transmission line theory, the impedance measured by the crystal is [5]

$$Z = (1 - \mathrm{i})r \tanh(\psi + \gamma a) , \quad (4)$$

where $\gamma = (1 - \mathrm{i})/\delta$ is the propagation constant of the viscous wave, and $\tanh \psi = Z_v/(1 - \mathrm{i})r$ is the ratio of the vapour impedance to the liquid impedance. For $a/\delta \ll 1$, the impedance measured is that of the vapour, Z_v; as a increases, $\tanh(\psi + \gamma a) \to 1$ and Z tends to the bulk value.

For a film in a vacuum, eq. (4) becomes

$$Z = (1 - \mathrm{i})r \tanh[(1 - \mathrm{i})a/\delta] . \quad (5)$$

As a increases, X and R increase and pass through a series of heavily damped maxima and minima corresponding to standing wave resonances in the film, as shown in fig. 2. Fig. 3 shows X versus R as a/δ varies for films of bulk impedance $r = 172$ kg m^{-2}s^{-1}, both in a vacuum ($Z_v = 0$) and for a vapour in contact with the film ($Z_v > 0$). The locus of Z is a spiral starting at Z_v for $a/\delta \ll 1$ and rapidly converging to $Z = (1 - \mathrm{i})r$.

The quartz crystal was mounted horizontally in a copper cell, a tube attached to the cell being partially filled with liquid helium. The thickness of the film on the crystal at a temperature T is determined by [6]

$$Ak/a^3 = -kT \ln(P/P_0) , \quad (6)$$

where the van der Waals constant A is 1.986×10^{-27} K m^{-3} for our crystals [1], k is the Boltzmann constant, P_0 is the saturated vapour pressure of the film and P is the actual pressure on the crystal. For an isothermal cell, the pressure P, and hence the film thickness will be determined by the crystal's height h above the liquid level and

$$Ak/a^3 = mgh \quad (7)$$

giving, for $h = 5.8$ cm, $a = 19$ nm. The film thickness was swept by creating a small temperature difference (~0.5 mK) between the crystal and the liquid in the tube. This changed the SVP of the film on the crystal and hence the film thickness could be swept from 1.5 nm to around 60 nm.

Fig. 3 shows data for X versus R at 3.11 K. The start of the spiral is the impedance of the vapour in contact with the film, measured when $a/\delta \ll 1$, with $\delta = 19$ nm. Assuming the vapour is in the hydrodynamic region, $Z_v = (1 - \mathrm{i})(\eta_v \rho_v \omega/2)^{1/2}$, and taking the vapour viscosity to be $\eta_v = 7.9$ μP [7], the real part of the vapour's impedance was calculated to be 17 kg m^{-2}s^{-1}. For thick films, $a/\delta \gg 1$, the measured film impedance tends towards that of the bulk liquid. Previous data [8], taken in the bulk liquid under SVP gives the real part of the impedance to be 172 kg m^{-2}s^{-1}. The fit of eq. (2) to the data is shown in fig. 3, where the real part of the vapour impedance is taken to be 16 kg m^{-2}s^{-1}, the bulk impedance is 172 kg m^{-2}s^{-1} and the $X = 0$ line is chosen so that $X = R$ for $a/\delta \gg 1$, thus allowing for the effects of mass loading. The $R = 0$ line here corresponds to the temperature independent value ($T < 0.6$ K) of Q^{-1} where the superfluid helium exerts no viscous forces on the crystal.

As shown in fig. 3, the transverse acoustic impedance of a helium film is described well by transmission line theory, giving a method for determining a which should be applicable to fluids other than helium. This experiment is the transverse analogue at 20 MHz of that of Sabisky and Anderson [9] who used longitudinal waves at around 30 GHz to detect standing wave resonances in a ^{4}He film; for a transverse wave however, the standing waves are much more heavily damped.

We would like to thank Professor E.R. Dobbs for his encouragement and support, A.K. Betts, F. Greenough and A. King for technical assistance and the SERC (UK) for a Research Grant and a Studentship (for D.S.S).

References

[1] M.J. Lea, P. Fozooni and P.W. Retz, J. Low Temp. Phys. 54 (1984) 303.
[2] M.J. Lea and P. Fozooni, J. Low Temp. Phys. 56 (1984) 25.
[3] F.P. Millikan, R.W. Richardson and S.J. Williamson, J. Low Temp. Phys. 45 (1981) 409.
[4] M.J. Lea and P.W. Retz, Physica 107B (1981) 225.
[5] M.J. Lea and P. Fozooni, Ultrasonics, to be published.
[6] D.F. Brewer, in: The physics of liquid and solid helium, Vol. II, eds. K.H. Bennemann and J.B. Ketterson (Wiley, New York, 1978) p. 573.
[7] D.S. Betts, Cryogenics 16 (1976) 3.
[8] M.J. Lea and P. Fozooni, unpublished.
[9] E.S. Sabisky and C.H. Anderson, Phys. Rev. A7 (1973) 790.

Acknowledgements

It is a pleasure to convey my thanks to the many people who have helped me in this project, particularly to my supervisor, Dr. M.J. Lea for his help and guidance and to Professor E.R. Dobbs for the provision of laboratory facilities at Bedford College, Regent's Park.

I should also like to thank Dr. P. Fozooni and Mr. F. Greenough for their patient advice and encouragement and for their friendship. My thanks also to Mr. A.K. Betts of the electronics workshop, and to Mr. F. Grimes and Mr. A. King for their help in the design and construction of the sonic cell.

Finally, I acknowledge the support of the SERC in the form of a research studentship.